A FINITE ELEMENT AND EXPERIMENTAL STUDY OF PLASTIC COMPRESSION FOR METAL FORMING

by

ROBIN HOULSTON

B.Sc., Physics, University of British Columbia, 1968
M.Sc., Applied Mechanics, University of Manchester, 1975

A THESIS SUBMITTED IN PARTIAL FULFILMENT OF

THE REQUIREMENTS FOR THE DEGREE OF

DOCTOR OF PHILOSOPY

in

THE FACULTY OF GRADUATE STUDIES

(Department of Mechanical Engineering)

We accept this thesis as conforming

to the required standard

THE UNIVERSITY OF BRITISH COLUMBIA

1984

In presenting this thesis in partial fulfilment of the requirements for an advanced degree at the University of British Columbia, I agree that the Library shall make it freely available for reference and study. I further agree that permission for extensive copying of this thesis for scholarly purposes may be granted by the head of my department or by his or her representatives. It is understood that copying or publication of this thesis for financial gain shall not be allowed without my written permission.

Department of Mechanical Engineering

The University of British Columbia
1956 Main Mall
Vancouver, Canada
V6T 1Y3

Date April 9, 1984.

ABSTRACT

Metal-forming involves the deformation of metals for the purposes of manufacturing a product. An understanding of the effect of process variables on metal forming operations is of fundamental importance to the engineer. However, little information is available regarding the effect of strain hardening and strain rate sensitive material properties, dynamic loading, surface friction and specimen dimensions on the way components deform during the forging process.

In this work the plane strain compression of an initially rectangular specimen between flat, parallel and rigid platens is selected for investigation as being representative of a basic die forging operation. This configuration allows the complete deformation history of quasi-statically or dynamically deformed specimens to be recorded photographically and the effect of process variables identified. A finite element model is developed for this case. The code accounts for large strains, nonlinear material properties, inertia effects and surface friction on all boundaries.

The results of dynamic compression tests on plasticine and quasi-static compression tests on aluminum are compared to the finite element code predictions. They give good correspondence over a large range of strain history. Further studies conducted with the finite element model identify many of the fundamental characteristics of the forging operation.

It is shown that rigid-perfectly plastic material tends to deform along lines of intense shear and can be approximated by certain upper bound solutions. The normal interface stress distribution for this case is very different from the classical friction hills that may sometimes be assumed. A more normal type of friction hill stress distribution is obtained with strain hardening and strain rate sensitive materials. The lines of intense shear become wider and give more homogeneous deformation for this case. With dynamic loading inhomogeneous deformation occurs as the energy of impact is rapidly diffused throughout the specimen. It is possible that an inverse friction hill develops on the lower platen and a friction hill on the top platen.

ACKNOWLEDGEMENTS

The author wishes to thank Professors G. W. Vickers and D. L. Anderson for jointly supervising the work.

The author is also thankful for the interest and cooperation shown by Professors J. P. Duncan, M. D. Olson and H. Ramsey.

The author also extends his gratitude to all the faculty and staff of the civil and mechanical engineering departments, without whose cooperation the work would not have been possible. In particular, he would like to thank John Richards, Electronics Technician. Mr. Richards designed and built the electronic circuits required for high speed photography in the experimental work.

A certain amount of work in this thesis was done at the Defence Research Establishment Suffield (DRES). The author acknowledges the cooperation of Mr. N. Bannister, Miss J. Smith, and Mr. H. Lightfoot of the DRES computing centre. The author was also encouraged by the interest shown in the work by the members of the Military Engineering Section at DRES.

The author gratefully acknowledges an H. R. MacMillan Family Fellowship (award 0326) awarded to him by the University of British Columbia.

TABLE OF CONTENTS

LIST OF FIGURES

NOMENCLATURE OF SELECTED SYMBOLS USED

Symbol	Description
D_{ij}	Effective deformation rate
S_{ij}	Deviatoric Stresses
Y	Yield stress
∇	Gradient operator
P	Mean normal stress
V_o	Platen velocity
$\bar{D}$	Effective deformation rate
$\bar{\sigma}$	Effective stress
σ_{ij}	Cauchy stresses
ρ	Mass density
v_i	Velocity
$\dot{v}_i$	Acceleration
T_i	Surface traction

DEDICATED TO MY PARENTS

CHAPTER 1

INTRODUCTION AND LITERATURE SEARCH.

1.1. METAL FORMING.

Metal-forming involves the deformation of metals for the purpose of manufacturing a product. Avitzur(1,1968) and Johnson and Mellor (2,1973) outline some of the metal forming processes currently used in industry.

An understanding of the effect of process variables on metal-forming operations must be considered of fundamental importance to the engineer in the design and development of manufacturing processes. For example, one may ask the following questions. What loads are required to deform the metal in a particular forming process? How do metal properties such as strain rate sensitivity and strain hardening affect the stress and deformation patterns? How do lubrication conditions on the boundaries of the metal in contact with the forming surfaces affect the stress distributions in the metal? What guidelines can one establish for effective design in metal-forming processes?

Very little information is available in the literature regarding the detailed effect of inertia, strain rate sensitivity, and strain hardening on the way components deform during the forging process and the resulting stresses and loads involved. This is due partially to the difficulties involved in measuring strain or stress within material that is undergoing very large, possibly rapid, distortions. Additionally, determination of the frictional boundary conditions that exist is extremely difficult.

1.2. SOLUTION TECHNIQUES.

1.2.1. Introduction.

A first step in the analytical treatment of a metal-forming problem is to propose a mathematical model. The model will usually involve large deformations, nonlinear materials, and unknown friction boundary conditions. In general there are no closed form solutions. Therefore, to solve practical problems, special procedures are employed to find approximate numerical solutions. Five practical methods for finding approximate solutions are limit analysis, the slip line field technique, the visioplasticity technique, the finite difference technique, and the finite element technique. The first four are discussed in sections 1.2.2 to 1.2.5 inclusive. In section 1.3 the finite element method is discussed.

1.2.2. Limit Analysis

The Upper Bound and the Lower Bound Theorems of plasticity allow one to place bounds on forming loads in metal forming processes. These theorems are discussed and proved by Hill(3,1950).

1.2.3. Slip Line Field Technique.

The slip line field method is applicable to plane strain problems and was introduced in 1923 by Hencky(4). Basically the method involves constructing a mesh of orthogonal lines along which the shear stress is a maximum. It is assumed that slip can occur only along these lines. From the limit theorems an upper bound on applied loads will be obtained. Johnson, Sowerby, and Venter(5,1982)

present numerous applications of the slip line field technique.

1.2.4. Visioplasticity.

Thomsen (6,1963) appears to have first introduced the visioplasticity technique. More recently Shabaik (7,1972) used the technique to study various types of metal forming processes. C.M.Lee, G.W Vickers, and S.N Dwivedi (8,1983) also futher extended the method to include dynamic problems.

The visioplasticity method uses the equations of motion to determine the stress field from an experimentally measured and numerically smoothed velocity field.

1.2.5. The Finite Difference Technique.

The finite difference technique is a well known computer-oriented method of numerically solving partial differential equations. Shabaik(9,1975) gives an example of the application of the method to plane strain extrusion. One of the disadvantages of the finite difference technique is that an equally divided mesh is required to achieve optimum accuracy.

1.3. APPLICATION OF THE FINITE ELEMENT METHOD TO THE SOLUTION OF METAL FORMING PROBLEMS.

1.3.1. Introduction.

The finite element technique is an appropriate numerical method for solving metal-forming problems. Irregular meshes can be used and very complex boundary conditions can be specified. The method is based on the construction of a velocity field over a small region (element) of material in terms of a number of generalised

coordinates. All the generalised coordinates from the elements are then determined to produce a solution. The resulting problem reduces to a set of simultaneous equations with the generalised coordinates as unknowns. Zienkiewicz(10,1977) shows that, subject to quite general requirements, as the number of elements spanning a region is increased to make more generalised coordinates available, the finite element solution will approach the exact solution to the mathematical model.

In the following sections the current literature on the application of the finite element technique to metal forming problems is reviewed. Section 1.3.2 cites some of the literature concerned with problems involving large strain finite element analyses. Section 1.3.3 cites some of the literature concerned with flow problems. Section 1.3.4 cites some of the literature concerned with plane strain and axisymmetric compression. Section 1.3.5 considers dynamic compression.

1.3.2. General Finite Element Formulation For Problems Of Large Strain.

In a large strain incremental approach it is usual to consider a coordinate system embedded in the material. Hibbitt(11,1970) gave one of the first treatments in the context of finite elements. Kitagawa, Seguchi, and Tomita (12,1972) gave a similar treatment using the techniques of differential geometry. Ref. 10 also considers geometrically nonlinear problems. These references all indicate that additional terms arise relating deformed geometry to initial geometry. Gotoh and Ishise (13, 1978) formulated

and applied the large strain case to a deep drawing problem. It was found that the large strain terms made a significant difference in their application.

1.3.3. Finite Element Applications To Flow Problems.

Zienkiewicz, Jain, and Onate(14,1978) gave a review of finite element numerical solution methods for studying the flow of solids. They first reviewed the general formulation for flow problems and identified two methods of merit: the V/P formulation with Lagrangian constraint and the penalty function approach. Several examples were given of extrusion, rolling, and cup forming.

Zienkiewicz and Godbole(15,1974) used a stream function representation to solve problems involving large distortions. Applications such as extrusion and indentation were treated as those of non-Newtonian flow. The method was applied to both steady state and transient problems.

Zienkiewicz and Godbole(16,1975) also introduced a penalty function approach for solving large deformation problems. They outlined how a standard elasticity program with a value of Poisson's ratio approaching 1/2 could be used to solve quasi-static flow problems. Examples of calculation with an isoparametric element with 2x2 Gauss integration were given for punch indentation, plane strain compression of a block, and extrusion.

1.3.4. Application Of The Finite Element Method To Plastic Compression.

Lee and Kobayashi(17,1973) applied the finite element method to the problem of the rigid-plastic axisymmetric compression of a cylinder. Friction on the top contact boundary was treated by applying a specified shear stress γ both as $\gamma=0.2Y_0$ and as $\gamma=0.3Y_0r/R$, where Y_0 is the constant yield stress, r is the radial coordinate and R is radius of the top boundary. They studied cylinders of height to diameter ratio (H_0/D_0) of 0.25, 0.5, and 1.0. They concluded that for $H_0/D_0=0.25$ and 0.5 there was a friction hill on the top boundary as predicted by elementary theory. For the case of $H_0/D_0=1$ they found an inverse friction hill. This reference also assessed the effect of work hardening.

Price and Alexander(18,1979) presented a paper on isothermal forging. Deformed geometries were presented for axisymmetric cylinders with height to diameter ratios of 1/4, 2/3, 1, 3/2, and 4. The calculations were carried out with the penalty function method. The predicted geometries were found to conform well with experiments for a variety of specimen configurations.

Hartley, Sturgess, and Rowe(19,1979) gave a technique of handling surface friction. They introduced a thin layer of friction elements on the top surface of an axisymmetric specimen to be deformed by a rigid platen. The top nodes were kept fixed to the rigid platen while the lower nodes were free to move horizontally. The stiffness of the friction elements were then modified by a viscous factor.

They identified the problems that they encountered with the application of the approach and described their solution. Good agreement was obtained with the ring test given by Hawkyard and Johnson(20,1967). A full elastic-plastic formulation was presented.

Hartley, Sturgess, and Rowe(21,1980) also presented a following paper in which they gave results for the elastic-plastic compression (up to 40%) of a cylinder with $H_o/D_o=1$. They confirmed, as did Lee and Kobayashi(17,1973) that an inverse friction hill occured on the top boundary for this case for certain values of the friction coefficient. The low values of friction tended to give an inverse friction hill. High values of friction tended to make the boundary surface traction more uniform. In the case of high friction a single large rigid zone occurred below the platen with high pressure areas near the centre and at the outside edge.

Rooyen and Backofen(22,1960) gave many experimental results for friction on thin discs. In agreement with the calculations of Lee and Kobayashi(17,1973) friction hills were observed in all cases. However, their tests were only for small H_o/D_o. Refs. 17 and 21 agree, however, that for $H_o/D_o=1$ inverse friction hills can result on the top boundary.

1.3.5. Dynamic Compression

Johnson(23,1972) has given an extensive treatment of dynamic impact for engineering applications. Of particular interest to the present work is Hawkyard's energy method and similar approaches (see Chapter 5 of ref. 23). Hutchings and O'Brien(24,1981) presented experimental results for impact of metal projectiles against rigid targets at low velocities (less than $100ms^{-1}$). A comparison was made to the theories of Taylor, Hawkyard, and Hutchings.

G.R.Johnson(25, 1976,26, 1977) considered elastic-plastic impact at high velocity. A code was developed for three dimensional tetrahedral elements. The type of problems considered were: impact of a nickel cylinder onto an aluminum plate at $1500ms^{-1}$, impact of a nickel sphere onto an aluminum plate at $1500ms^{-1}$, normal impact of a nickel truncated cone onto an aluminum variable thickness plate at $1500ms^{-1}$, and oblique impact of an aluminum rod onto a rigid surface at $1000ms^{-1}$.

A general review of impact dynamics was presented by Zukas(27,1980) for materials subjected to intense impulsive loading.

1.4. PURPOSE AND SCOPE OF THE THESIS.

The objective of this work is to gain some fundamental insight into the general effect that material properties, boundary friction, and inertia have on the way forging specimens deform. Of interest also is the stress distributions, strain distributions, and loads involved. With this in mind a simple type of die forging operation

was selected; namely, the plane strain compression of an initially rectangular specimen between flat, parallel, and rigid platens. The process is depicted in Fig. 4.2.4.

The reason for the selection of this case is that the complete deformation history can be recorded photographically by observing the distortion of the mesh on the specimen through the glass plates. The effect of the process variables can thus be readily recorded.

Plasticine was selected as the test material. This has been used extensively for metal forming studies and is known to give a reasonable assessment of the deformations that occur in metal forming. Its main advantage in the present study is that the loads involved for specimens of a size suitable for observation are not excessively large. It is, however, a strain rate sensitive material which has to be accounted for in any numerical modelling.

With the experimental results as a basis for comparison, a finite element model was developed. To do the calculations a finite element code was prepared to model plane strain plastic compression. The code which will be referred to as FELEM-RH has surface friction routines for both static and dynamic conditions and plotting routines for graph plots and pictorial displays. The code was intended to be compact in nature although generally applicable to a range of bulk metal - forming problems. In the work the results of dynamic compression tests on plasticine and the quasi-static compression of aluminum are compared with code predictions. These initial comparisons are then followed by a systematic study of the effect of

strain rate sensitivity, strain hardening, and inertia on specimens of various dimensions.

The results of the study indicate that all the variables mentioned have significant effect on the resulting deformation and stress patterns. The applicability of approximate upper bound models to many of the cases are discussed.

The chapter contents are summarized below. Chapter 2 presents some simplified solutions for plane strain compression. Chapter 3 presents a review of the formulation of the finite element equations. Chapter 4 presents some experimental work for the plane strain deformation of plasticine for comparison with numerical solutions. Chapter 5 presents the results of calculations done with the code. Both static and dynamic cases were considered and comparison with experimental results made. In addition, comparison of quasi-static solutions found for a rigid-plastic material were compared with slip line field solutions and velocity discontinuity patterns. Chapter 6 presents an overall summary and conclusion of the study.

CHAPTER 2

APPROXIMATE MODELS.

Approximate closed form solutions are used widely in metal forming problems. A summary of these approximate solutions is given by Bishop(28,1958). In this reference solutions for plane strain compression are summarised. In this work the main interest in these approximate solutions is for comparison purposes with the finite element code predictions and for determining their applicability over a variety of conditions.

The following sections of this chapter present approximate solutions for the plane strain compression of a rigid-perfectly plastic material between flat and parallel platens. In section 2.1 the solution for homogeneous plane strain deformation is given. While this solution is simple and exact, it is only of limited use in practice. It will only occur in the absence of platen friction. In section 2.2 it is assumed, however, that an homogeneous velocity field still exists even with friction. The solution can then be easily found but it is approximatate since an assumed displacement field is used. In section 2.3 velocity discontinuity patterns are presented and used to find upper bound solutions.

2.1. HOMOGENEOUS PLANE DEFORMATION.

2.1.1 Introduction.

For the case where platen friction and glass-plate friction is zero homogeneous deformation results and the free boundaries of the specimen remain straight and parallel. Fig. 2.1.1.1 depicts the process.

The solution for this case is well known -- the velocity field is linear and the stresses are constant.

2.1.2 The Velocity and Stress Fields.

The equation of continuity is

$$v_{i,i} = 0 \qquad (2.1.2.1)$$

where v_i $(i = 1,2)$ are the velocity components in plane strain referred to the fixed rectangular cartesian axes x_1, x_2 as shown in Fig. 2.1.1.1. The repeated index implies summation and the comma denotes partial differentiation with respect to x_i.

For the homogeneous deformation of a rectangular block the velocity components satisfying equation 2.1.2.1 are

$$v_1 = \frac{v_0}{L} \cdot x_1 \qquad (2.1.2.2)$$

$$v_2 = \frac{v_0}{L} \cdot x_2 \qquad (2.1.2.3)$$

where v_o is velocity of the platens relative to the centre of the specimen and 2L is the current specimen height.

The Cauchy stresses σ_{ij} referred to the fixed rectangular coordinate axis x_i is

$$\sigma_{ij} = \begin{bmatrix} 0 & 0 \\ 0 & -\sigma_p \end{bmatrix} \qquad (2.1.2.4)$$

where σ_p is the uniform platen pressure. For a perfectly plastic material σ_p will be equal to the yield stress, Y, of the material. In general the yield stress Y will be a function of the effective strain $\bar{e}$ and the effective deformation rate $\bar{D}$. The definition of the effective strain

is given as

$$\bar{\varepsilon} = \int_0^t \bar{D}\, dt \qquad (2.1.2.5)$$

$$\text{where } \bar{D} = \sqrt{(2/3)\, D_{ij} D_{ij}} \qquad (2.1.2.6)$$

$$D_{ij} = (1/2)(v_{i,j} + v_{j,i}) \qquad (2.1.2.7)$$

In the present case the effective strain is given by

$$\bar{\varepsilon} = (2/\sqrt{3}) \left| \ln (L/L_o) \right| \qquad (2.1.2.8)$$

where $2L_o$ is the initial specimen height.

A general form (3) for Y which can be adapted to the specific cases is

$$Y = \begin{cases} \alpha \bar{D} \text{ if } \bar{D} \le \bar{D}_o \\ (1+c_1\bar{\varepsilon})^{\gamma} [Y_o + c_2(\bar{D}-\bar{D}_o)^{c_3}] \text{ if } \bar{D} > \bar{D}_o \end{cases} \qquad (2.1.2.9)$$

$$\text{where } \bar{D}_o = (1+c_1\bar{\varepsilon})^{\gamma} Y_o/\alpha \qquad (2.1.2.9)$$

α is a large number chosen to approximate rigid-plastic behavior. Y_o is the static annealed yield stress. c_1, c_2, c_3, and are constants.

2.2 HOMOGENEOUS PLANE DEFORMATION WITH FRICTION

Homogeneous deformation as discussed in Section 2.1 cannot occur if there is friction on the boundaries. An approximate result given by Hill (3) can be obtained, however, by assuming homogeneous deformation as far as the velocity field is concerned but including a shear stress on the boundaries for the stress calculation. This model is illustrated in Fig. 2.2.1.

A force balance on the differential element with $x_i = (x, y)$ gives

$$(d\sigma_{xx}/dx) = \tau/L \qquad (2.2.1)$$

where τ is the boundary shear stress, and σ_{xx} the horizontal stress which is independent of specimen height y. If Coulomb friction is assumed then

$$\tau = -\eta \sigma_{yy} \qquad (2.2.2)$$

where σ_{yy} is the y component of stress and η is the coefficient of friction. The negative sign is introduced since σ_{yy} is considered positive when tensile. The yield condition for a rate-insensitive non-strain hardening isotropic material is

$$\bar{\sigma} = Y_0 \qquad (2.2.3)$$

where

$$\bar{\sigma} = \sqrt{(3/2)(S_{xx}^2 + S_{yy}^2)} \qquad (2.2.4)$$

The Levy-Von Mises flow rule can be used to show that

$$\sigma_{zz} = P \qquad (2.2.5)$$

where σ_{zz} is the stress in the direction normal to the plane of deformation. This requires that

$$P = (1/2)(\sigma_{xx} + \sigma_{yy}) \qquad (2.2.6)$$

The result 2.2.6 can be used with equations 2.2.4, 2.2.3 and the fact that $\sigma_{xx} = S_{xx} + P$ and $\sigma_{yy} = S_{yy} + P$ to write the yield

condition in the form

$$|\sigma_{xx}-\sigma_{yy}|=2K \qquad (2.2.7)$$

where $K=Y_0/\sqrt{3}$. K is the yield shear stress. Equation 2.2.7 implies that $(d\sigma_{xx}/dx)=(d\sigma_{yy}/dx)$ since K is constant. Equation 2.2.1 can thus be written, with γ replaced from equation 2.2.2

$$d\sigma_{yy}/dx=-\eta\sigma_{yy}/L \qquad (2.2.8)$$

This can now be integrated as

$$\int_{x=W}^{x}(d\sigma_{yy}/\sigma_{yy})=-(\eta/L)\int_{W}^{x}dx \qquad (2.2.9)$$

The integration can be carried out using the fact that σ_{yy} at x=W (on the boundary) is -2K. Since K is required to be positive the negative sign indicates a compressive stress. The integration is carried out as

$$\ln(\sigma_{yy})\Big|_{w}^{x}=(\eta/L)(W-x)$$

$$\text{Thus } \ln[\sigma_{yy}/(-2K)]=(\eta/L)[W-x]$$

$$\text{or } \sigma_{yy}=-2K[\exp\{(\eta/L)(W-x)\}] \qquad (2.2.10)$$

Equation 2.2.10 indicates a friction hill type of distribution; that is, the magnitude of σ_{yy} increases towards the centre of the specimen.

The result can be written in non-dimensional form as

$$[-\sigma_{yy}/(2K)]=\exp[\eta\ell/L] \qquad (2.2.11)$$

where ℓ is the distance inwards from the right boundary of the specimen. A simple non dimensional diagramatic representation of a friction hill distribution is given in Fig. 2.2.2. There is an exponential increase in σ_{yy} towards

the centre of the specimen.

From the derivation a qualititative observation can be made. During compression σ_{xx} must always increase towards the centre. If the average σ_{xx} over a vertical plane in the material such as AD in Fig. 2.2.1 is used, then even for inhomogeneous deformation the average σ_{xx} must increase according to equation 2.2.11.

2.3. VELOCITY DISCONTINUITY PATTERNS.

Ref. 2 describes the method by which velocity discontinuity patterns and associated hodographs can be constructed. For convenience a brief description of the method is presented here.

In the model considered in section 2.2 σ_{xx} and σ_{yy} were principal stresses. Under these conditions, the lines of maximum shear stress occur at 45° to the x axis in Fig. 2.2.1. A velocity discontinuity pattern is constructed by assuming that the block of material being compressed is formed of rigid blocks of material defined by boundaries which are the 45° lines of maximum shear stress. The blocks are considered to slide over each other with a shear stress K acting between the blocks. The power dissipation at these sliding interfaces thus represents the internal power which can be equated to the power of the external loads to obtain an estimate of the forming load required.

Thus for a block with H/D=1, a velocity discontinuity pattern and hodograph can be constructed as shown in Fig. 2.3.1. The rigid blocks ABC and EBF in Fig. 2.3.1 move vertically with unit velocity. The blocks FBC and AEB move horizontally. Slip thus occurs, for example, between blocks

ABC and CBF along BC. The hodograph is constructed by first drawing an arrow V_{12} to represent the vertical velocity of block ABC. An arrow V_{13} is then drawn to represent the horizontal velocity of block CBF. $V_{23}=\sqrt{2}$ on the hodograph is the relative velocity between the two blocks ABC and CBF.

It is next assumed that the traction due to the friction between the blocks is K, the yield stress of the material in shear. For a block of unit thickness the total power dissipation in BC is thus $\sqrt{2}K$ times the length BC which is $\sqrt{2}$. 2K is thus the total power dissipation in BC, and 8K is the total power dissipation in all the velocity discontinuities. Let σ_{yy} be the normal tractions on AC and EF. The external power associated with compressing the block is $4\sigma_{yy}$. Since this must equal the internal power dissipation 8K, then $\sigma_{yy}=2K$ is the estimated traction on AC and EF

2.3.1. A Velocity Discontinuity Pattern For $H/D\geq 2$

For integral values of $H/D\geq 2$, the block in Fig. 2.3.1 can be used to build up a velocity discontinuity pattern. For H/D=2, for example, the pattern shown in Fig. 2.3.1.1 could be used. It is clear that EF has zero velocity here and hence the power dissipation in AEFC is only one half of that in Fig. 2.3.1. Since block EHIF has equal power dissipation to block AEFC however, the total power dissipation in the block AHIC in Fig. 2.3.1.1 is the same as it was in block AEFC in Fig. 2.3.1. $\sigma_{yy}=2K$ is thus still the compressive surface traction on the platen faces.

For non integral values of $H/D\geq 2$, the situation

becomes slightly more complex. Fig. 2.3.1.2 shows one possible velocity discontinuity pattern for H/D=3.35. Basically this is constructed by first drawing the pattern for H/D=4 and then reducing the height by allowing the lines to overlap in a way that is obvious from Fig. 2.3.1.2. The hodograph shows that the relative velocities between all the blocks is $\sqrt{2}/4$. The total power dissipation along BE and BG, for example, is $2\sqrt{2}(\sqrt{2}/4)K$ or K. The total power dissipation in AOIE is thus 2K, and for the whole block JKLE is 8K. Since the same internal power as found previously holds, the same forming load is obtained.

2.3.2. A Velocity Discontinuity Pattern For $1 \leq H/D \leq 2$

Fig. 2.3.2.1 shows a proposed velocity discontinuity pattern and hodograph for this case. Using the same procedure as previously, $\sigma_{yy}=2K$ is again obtained for the compressive stress.

2.3.3. A Velocity Discontinuity Pattern For $H/D \leq 1$

A velocity discontinuity pattern and hodograph for $H/D \leq 1$ is shown in Fig. 2.3.3.1. In this particular case H/D=0.516 was chosen for illustration. Again $\sigma_{yy}=2K$ is obtained for the compressive stress.

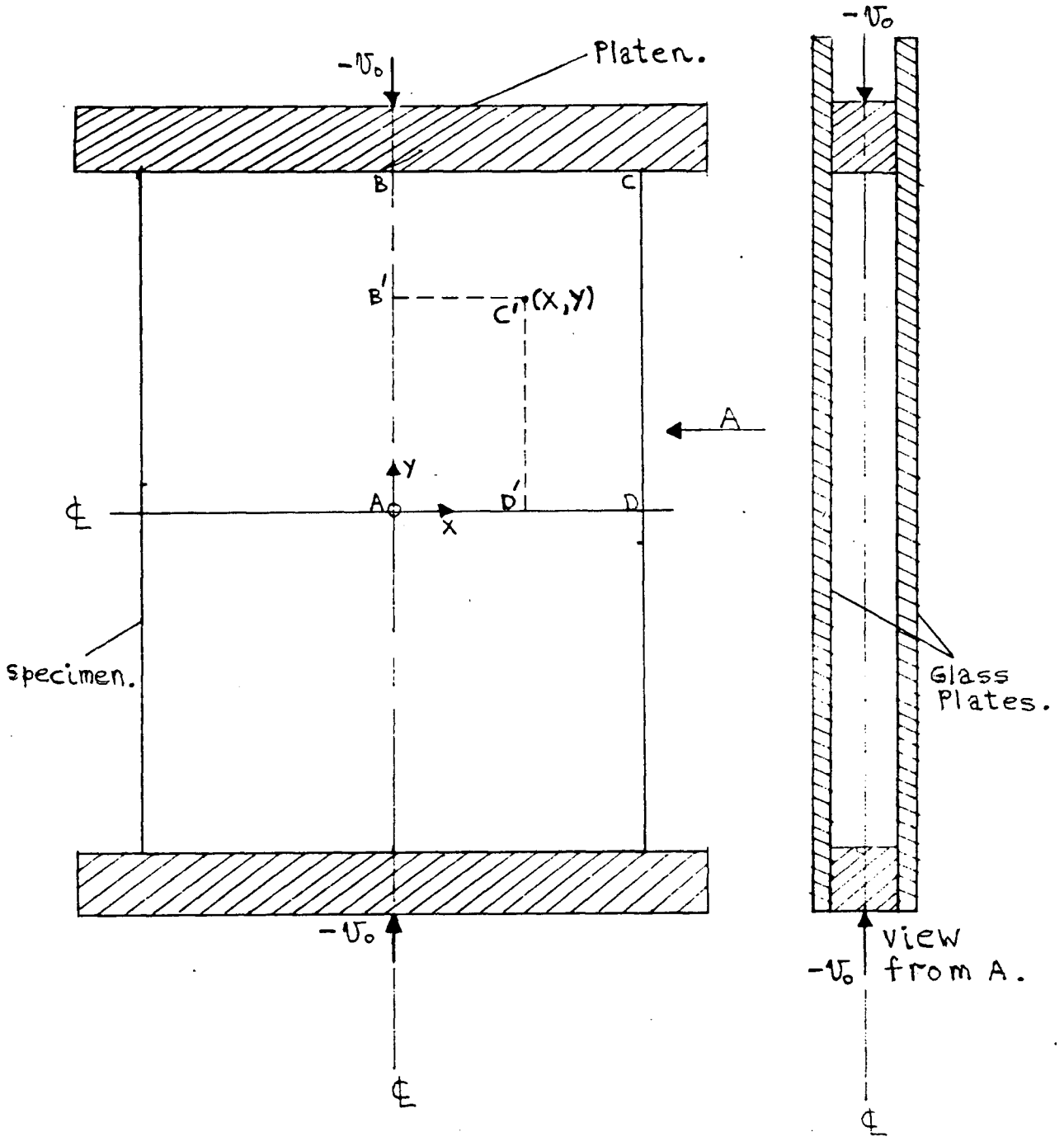

FIG. 2.1.1.1.

ILLUSTRATION OF THE HOMOGENEOUS PLANE DEFORMATION OF A BLOCK OF MATERIAL BETWEEN TWO FRICTIONLESS AND RIGID PLATENS.

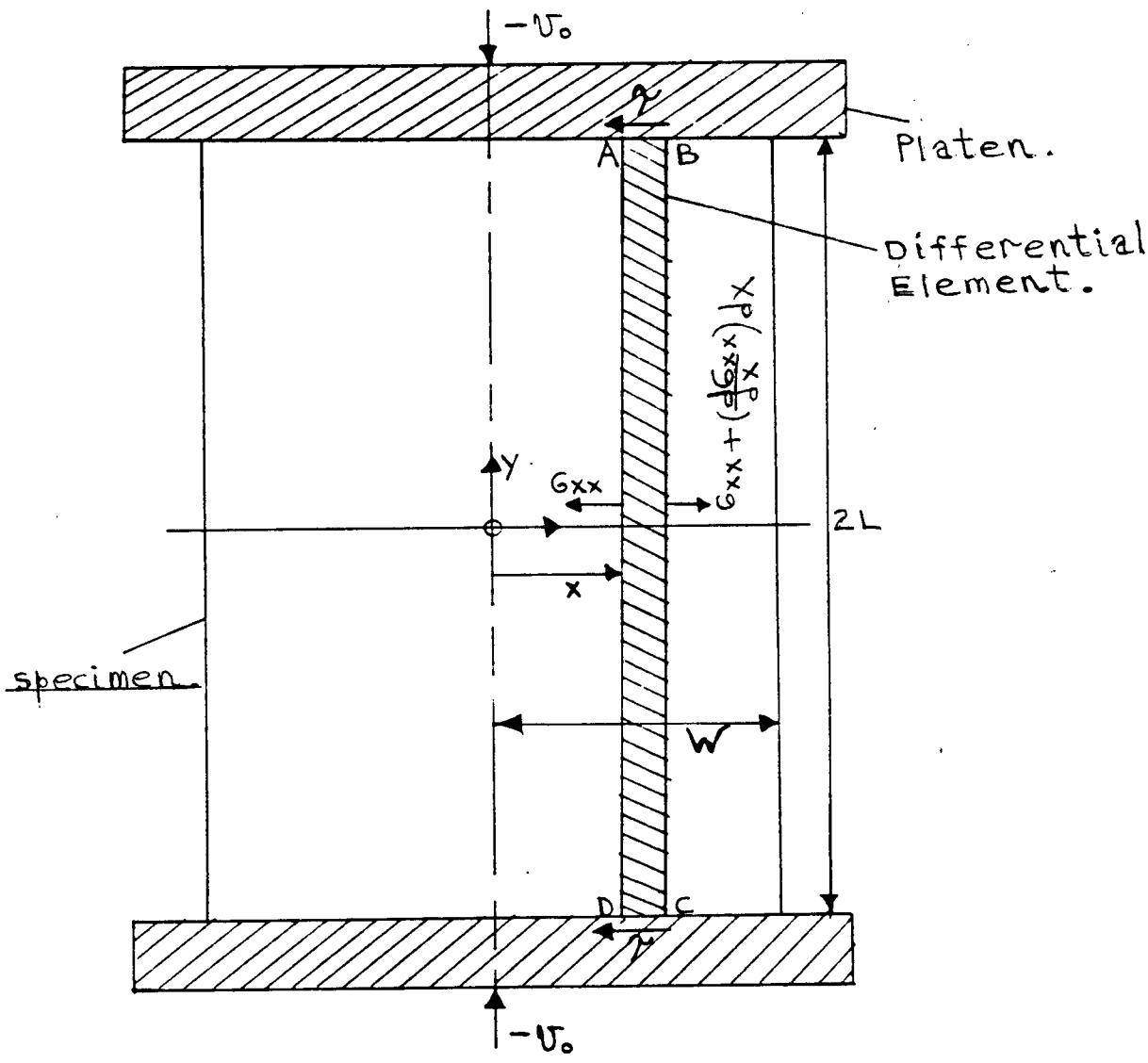

FIG. 2.2.1.

HOMOGENEOUS PLANE DEFORMATION WITH FRICTION ASSUMED TO ACT ON THE PLATENS.

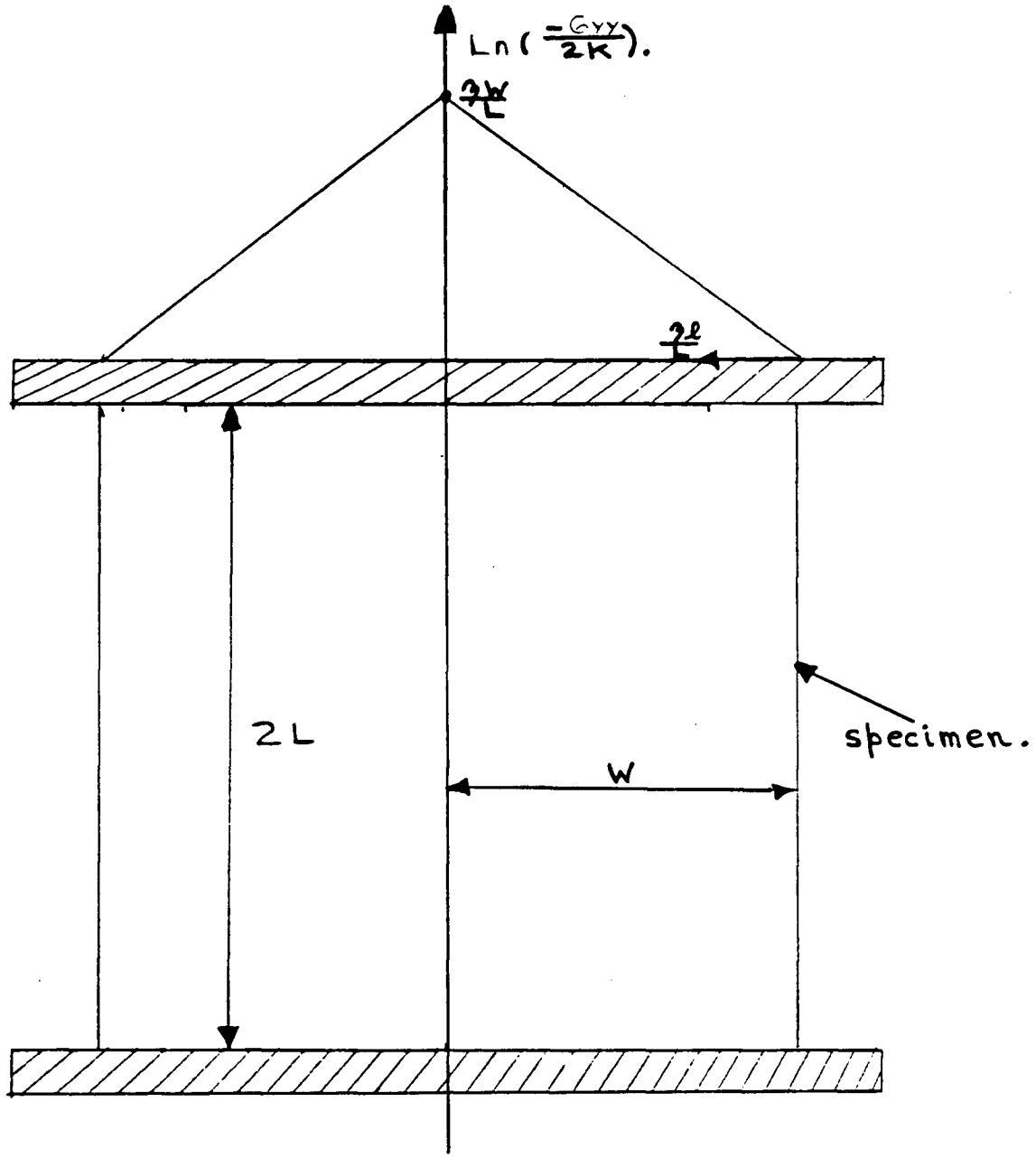

FIG. 2.2.2.

ILLUSTRATION OF A FRICTION HILL NORMAL STRESS DISTRIBUTION IN NON-DIMENSIONAL FORM.

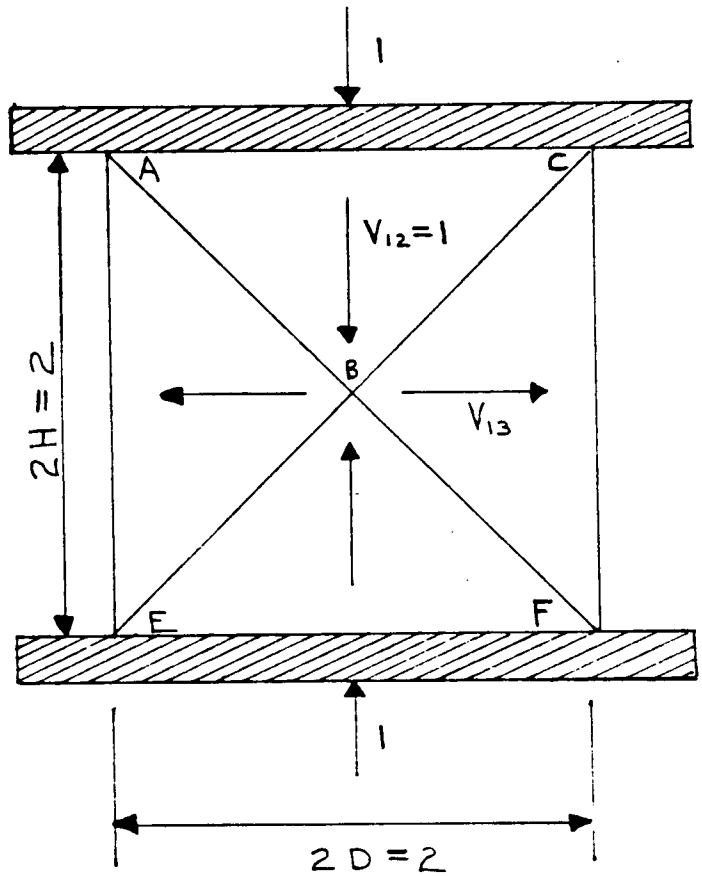

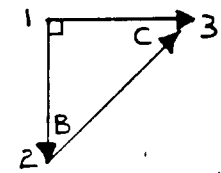

Hodograph.

FIG. 2.3.1.

A VELOCITY DISCONTINUITY PATTERN FOR THE CASE H/D = 1.

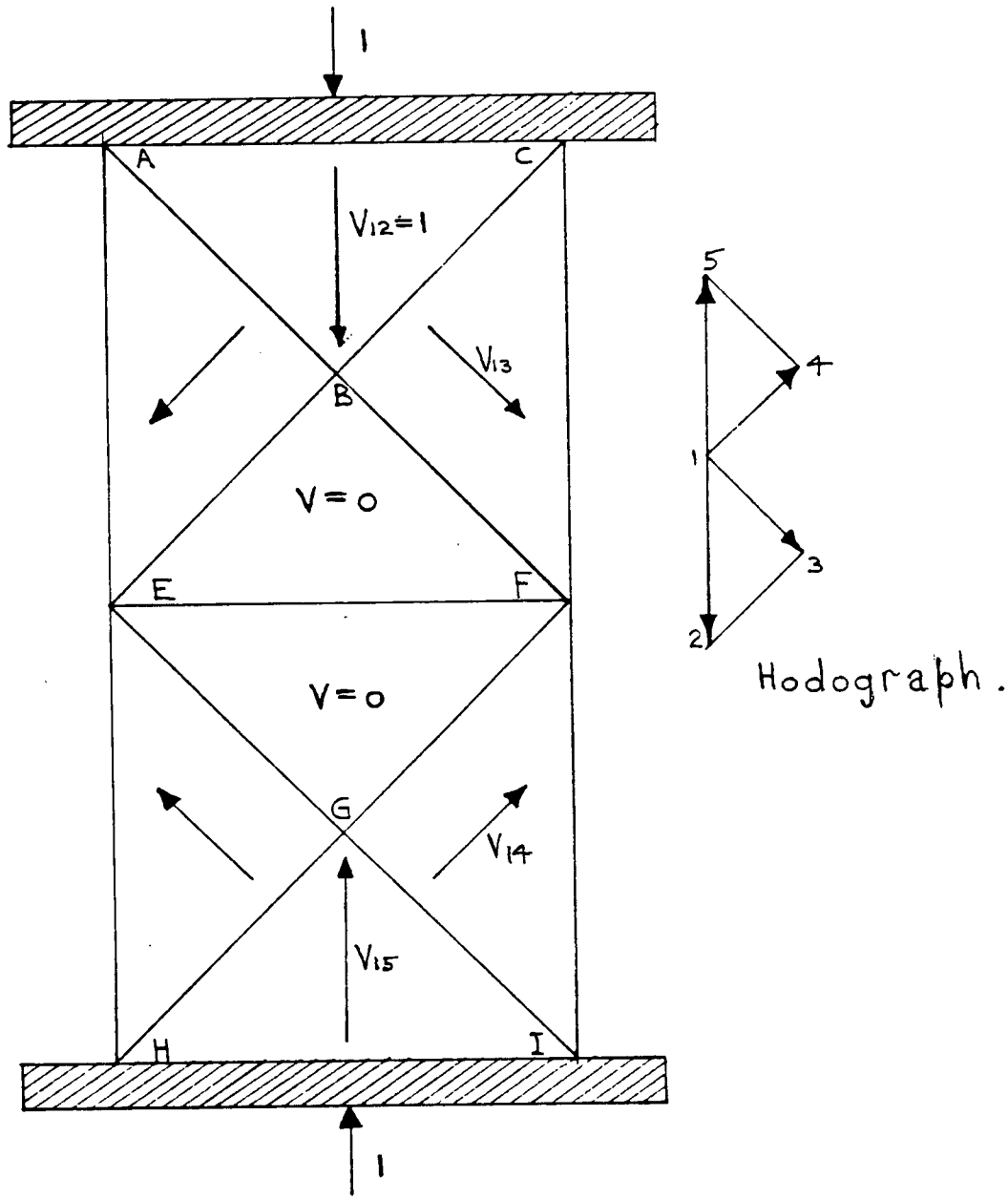

FIG. 2.3.1.1.

A VELOCITY DISCONTINUITY PATTERN FOR THE CASE H/D = 2.

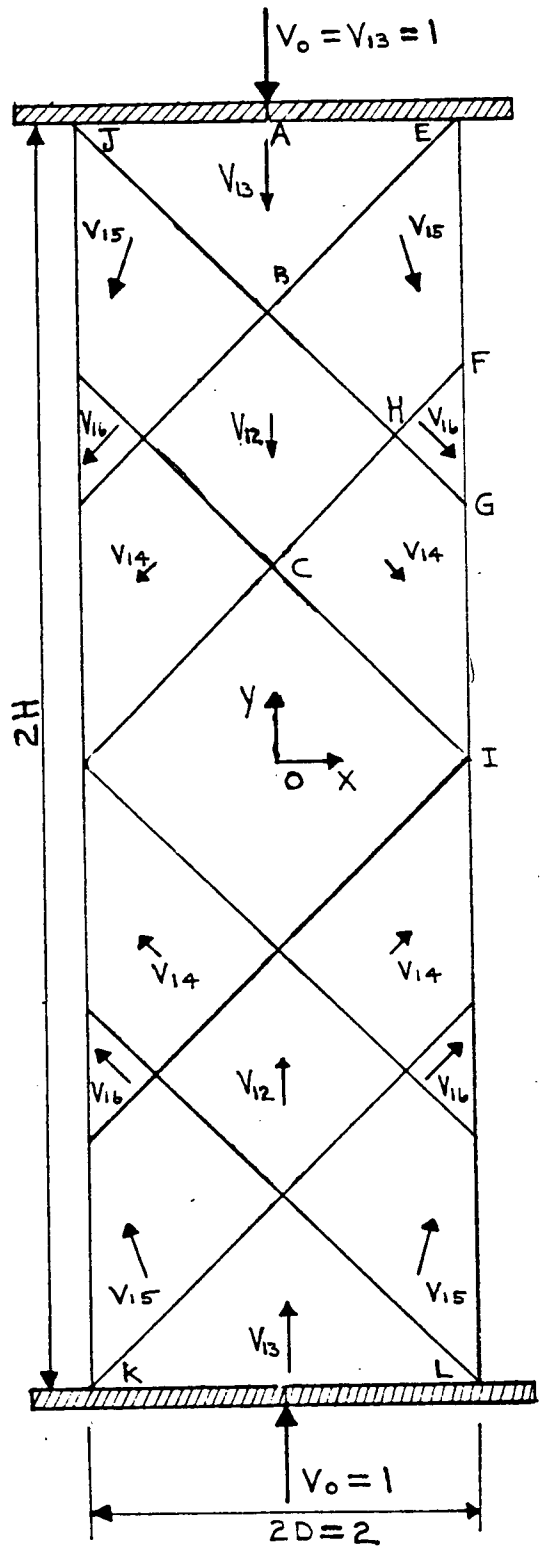

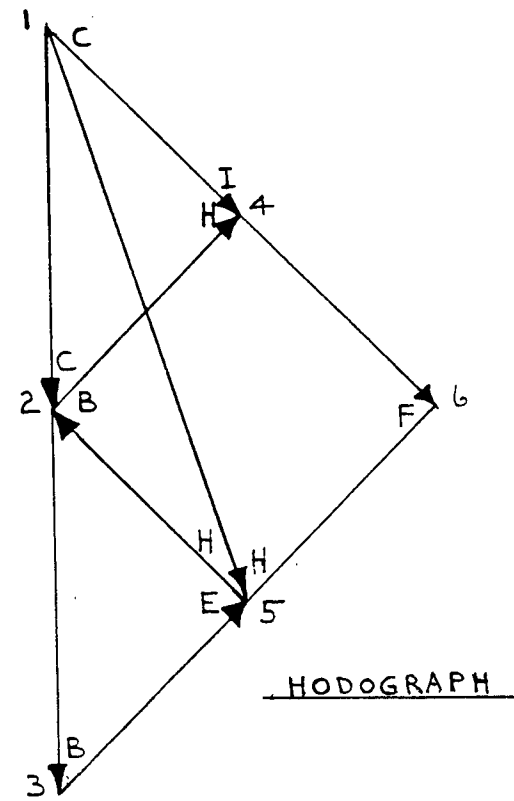

FIG. 2.3.1.2.

ONE POSSIBLE VELOCITY DISCONTINUITY PATTERN FOR PERFECTLY PLASTIC PLANE STRAIN COMPRESSION BETWEEN RIGID AND PARALLEL PLATENS. $H/D \geqslant 2$ IS ASSUMED IN THE DIAGRAM.

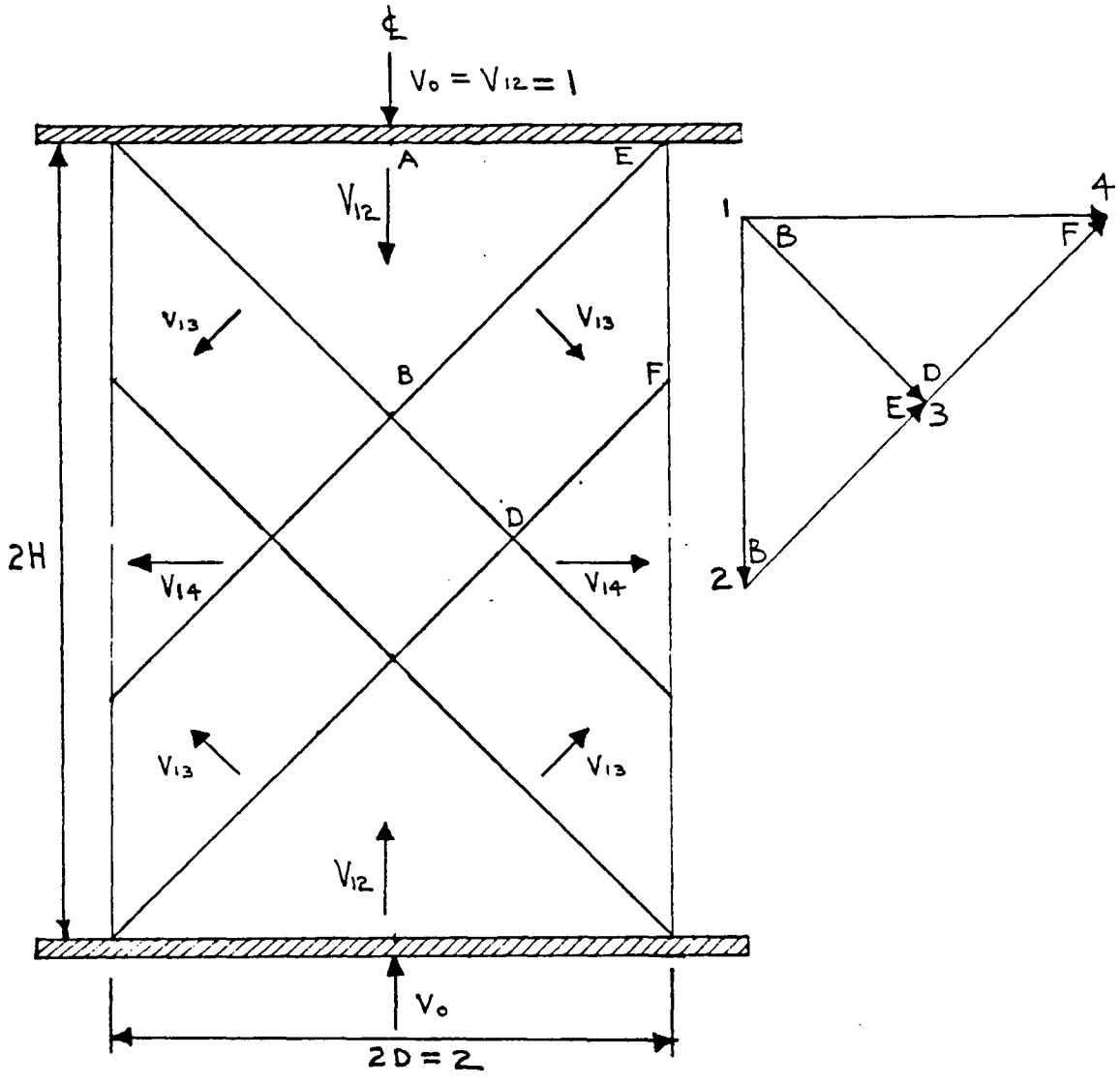

FIG. 2.3.2.1.
A POSSIBLE VELOCITY DISCONTINUITY PATTERN FOR PERFECTLY PLASTIC PLANE STRAIN COMPRESSION BETWEEN RIGID AND PARALLEL PLATENS. $1 \leq H/D \leq 2$ IS ASSUMED IN THE DIAGRAM.

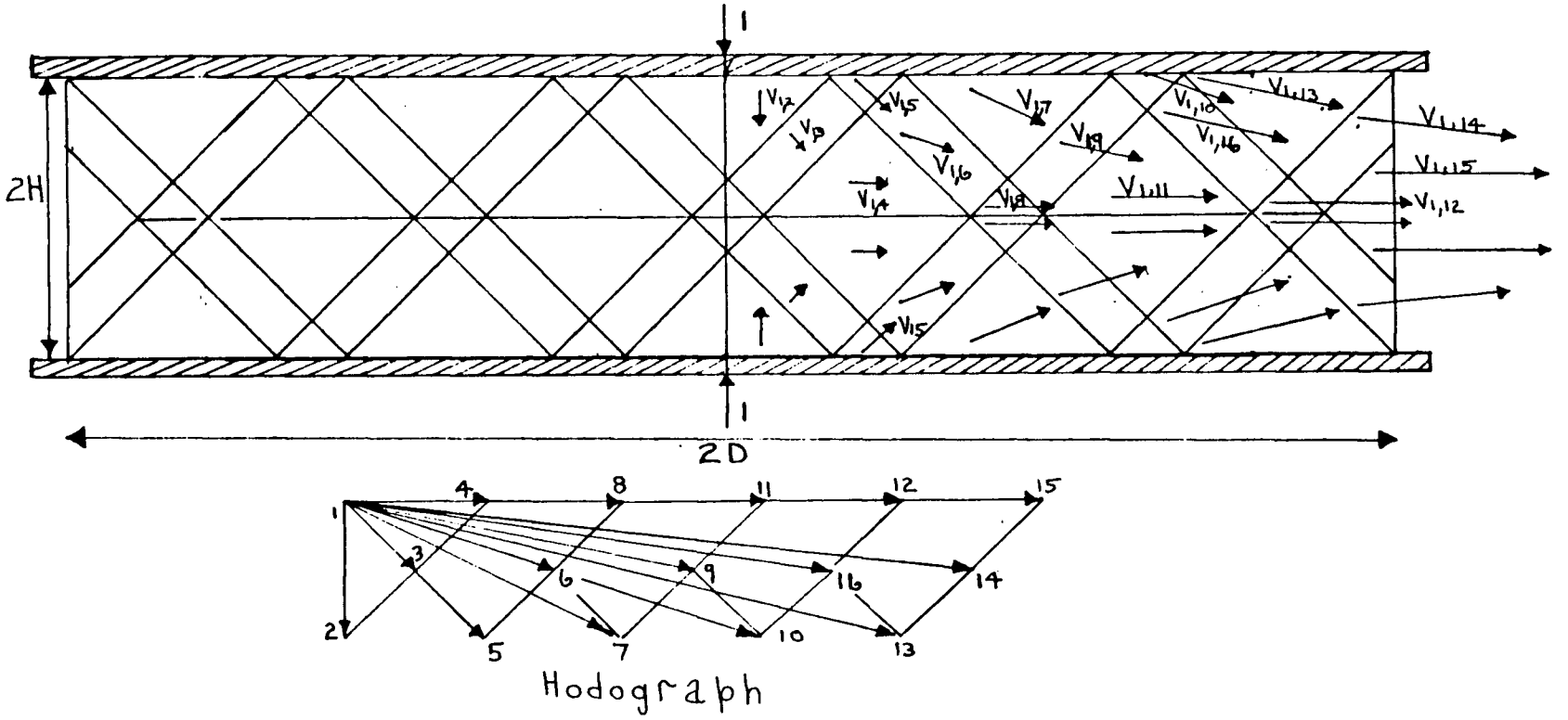

FIG. 2.3.3.1.

A POSSIBLE VELOCITY DISCONTINUITY PATTERN FOR PERFECTLY PLASTIC PLANE STRAIN COMPRESSION BETWEEN RIGID AND PARALLEL PLATENS. $H/D < 1$ IS ASSUMED IN THE DIAGRAM.

CHAPTER 3

THE FINITE ELEMENT FORMULATION.

3.1. INTRODUCTION

The Finite Element Method (FEM) is now well established as a powerful numerical technique for solving problems in solid mechanics with complex boundary conditions. One purpose of this work is to develop a specialised efficient code capable of being easily adapted to modelling the complex problems that occur in metal forming applications. These applications involve very large plastic deformations and very complex friction boundary conditions. These factors must be considered in conjuction with strain hardening and strain rate sensitivity of the material. In addition, dynamic effects must be taken into account for rapid metal forming applications. The formulation of the code is based on existing methods of analysis. Tomita and Sowerby(29) have applied the formulation to metal forming problems. A brief outline of the finite element theory is given in this chapter as the rationale for the selection of the approach. Specialised procedures formulated by the author will be discussed in full but standard ones will only be discussed briefly.

3.2. FORMULATION OF THE FINITE ELEMENT EQUATIONS.

A review of continuum mechanics is given by Mase(30). However, for completeness and future reference relevant equations of continuum mechanics that are to be solved are given here. It is recalled that the rectangular cartesian coordinates, x_i, and Cauchy stresses, σ_{ij}, are used.

The equation of motion governing mechanical behaviour is

$$\sigma_{ij,j} - \rho \dot{v}_i = 0 \qquad (3.2.1)$$

and the continuity equation for an incompressible material is

$$v_{i,i} = 0 \qquad (3.2.2)$$

It is recalled that the components of deformation rate are given by

$$D_{ij} = (1/2)(v_{i,j} + v_{j,i}) \qquad (3.2.3$$

and the effective deformation rate is given by

$$\bar{D} = \sqrt{(2/3) D_{ij} D_{ij}} \qquad (3.2.4)$$

The effective plastic strain is

$$\bar{e} = \int_0^t \bar{D} dt \qquad (3.2.5)$$

and the yield function to be specified for each material is given by

$$Y = Y(\bar{e}, \bar{D}) \qquad (3.2.6)$$

The definition of a generalized viscosity is given by

$$\gamma = (2Y)/(3\bar{D}) \qquad (3.2.7)$$

and the Levy-Von Mises flow rule by

$$S_{ij} = \gamma D_{ij} \qquad (3.2.8)$$

In the above equations σ_{ij} is the Cauchy Stress Tensor, ρ the mass density, v_i the velocity, and S_{ij} the deviatoric Cauchy stress tensor.

The finite element method transforms the equations 3.2.1 and 3.2.2 to a system of algebraic equations. The equivalent principles of virtual power given below are used for this purpose. The equation thus derived is

$$\int_A t_i \delta U_i \, dA - \int_V \rho \dot{U}_i \delta U_i \, dV - \int_V \sigma_{ij} \delta D_{ij} \, dV = 0 \qquad (3.2.9)$$

$$\int_V v_{i,i} \delta P \, dV = 0 \qquad (3.2.10)$$

where t_i is surface traction per unit area A, $\dot{v}_i$ denotes the derivative of v with respect to time, V is volume . δv_i denotes arbitrary variations of the velocity components U_i which are subject to the constraint given in 3.2.10. The arbitrary variation in pressure, δP, and deformation rate components δD_{ij} can be expressed in terms of δv_i using equation 3.2.3. The components of surface traction t_i are obtained from the Cauchy stress components σ_{ij} by $t_i = \sigma_{ij} n_j$ where n_j are the components of the outward unit normal to the surface.

v_i is now expanded with respect to a set of discrete nodal values $v_{\varphi r}$ referred to a set of basis functions $\psi_\varphi(x_I)$

$$v_r = \psi_\varphi(x_i) v_{\varphi r} \qquad (3.2.11)$$

where summation over the nodes Q is implied.[1] $\psi_\varphi(x_i)$ is the basis function of the global coordinates x_i for global node

---

1 The summation rule on repeated indices will be assumed throughout this chapter and future chapters unless otherwise stated.

Q and satisfies the condition $\varphi_Q(x_i)=1$ when x_i are the coordinates for node Q. At all other nodes the value of this function is zero. The function varies continuously between nodes and is chosen to give only local support to the velocity field.

Similarly, the hydrostatic pressure is an independent variable in a rigid-plastic formulation. Let a different set of nodes L be defined for pressure, and let P_L be the pressure at the L'th pressure node. These pressures can be expanded with respect to a set of basis functions, ψ_L as follows

$$P=\psi_L P_L \qquad (3.2.12)$$

If the expansions 3.2.11 and 3.2.12 are substituted into equations 3.2.9 and 3.2.10 respectively, and consideration is given of the fact that the variations δv_i and δP are arbitrary, the required finite element equations result. These equations are listed below. In these equations $\underline{QR}$ and $\underline{ST}$ represent single indices denoting, respectively, the global variable number of the R'th degree of freedom at global node Q and the T'th degree of freedom at global node S. L denotes global variable number of the single degree of freedom pressure, at pressure nodes. The summation rule on repeated indices in a product term also holds.

$$(M_{\underline{QRST}})(\dot{V}_{\underline{ST}})+(C_{\underline{QRST}})(V_{\underline{ST}})+(G_{\underline{QR}L})(P_L)=(F_{\underline{QR}}) \qquad (3.2.13)$$

$$(G_{\underline{ST}L})(V_{\underline{ST}})=0 \qquad (3.2.14)$$

$$(M_{\underline{\varphi R S T}}) = \delta_{RT} \int_V [(\rho)(\gamma_S)(\gamma_\varphi)]dV \qquad (3.2.15)$$

$$(C_{\underline{\varphi R S T}}) = \int_V [(\gamma)(B_{IJ\varphi R})(B_{IJST})]dV \qquad (3.2.16)$$

$$(G_{\underline{\varphi R L}}) = \int_V [(\gamma_{\varphi,R})(\psi_L)]dV \qquad (3.2.17)$$

$$(B_{IJST}) = (1/2)[(\gamma_{S,J})\delta_{IT} + (\gamma_{S,I})\delta_{JT}] \qquad (3.2.18)$$

$$(v_R) = (\gamma_\varphi)(V_{\underline{\varphi R}}) \qquad (3.2.19)$$

$$(D_{IJ}) = (B_{IJST})(V_{\underline{ST}}) \qquad (3.2.20)$$

Here $\dot{V}_{\underline{ST}}$, $V_{\underline{ST}}$, and $F_{\underline{ST}}$ represent the acceleration, velocity, and external force components in the T'th degree of freedom at node S. P_L is the hydrostatic pressure at the L'th pressure node. $(M_{\underline{\varphi R S T}})$, $(C_{\underline{\varphi R S T}})$, and $(G_{\underline{\varphi R L}})$ are the mass, stiffness, and constraint matrices, respectively, which will subsequently be denoted [M], [C], and [G]. Similarly, $(\dot{V}_{\underline{ST}})$, $(V_{\underline{ST}})$, and (P_L) are the acceleration, velocity, and pressure matrices, respectively, which will subsequently be denoted by $\{\dot{V}\}$, $\{V\}$, and $\{P\}$. δ_{RT} is the Kronecker Delta ($\delta_{RT}=1$ if R=T and $\delta_{RT}=0$ if R≠T). A comma denotes differentiation with respect to the global coordinates x_I. In order to solve equations 3.2.13 and 3.2.14 the acceleration must be related to the velocity. In

order for this to be done a finite difference integration formulae must be adopted. Let

$$\{V\} = [(1-\phi)\{\dot{V}\}+\phi\{\dot{V}\}_1]\Delta t+\{V\} \qquad (3.2.21)$$

where $\{V\}_1$ and $\{\dot{V}\}_1$ are the global velocity and acceleration vectors at time $t+\Delta t$ and the vectors without a subscript "1" are those at time t. ϕ is a constant that can be chosen for optimum accuracy.

If equation 3.2.21 is substituted into equation 3.2.13 and then the equations 3.2.13 and 3.2.14 are written in matrix form the result can be expressed as

$$\begin{bmatrix} [\tilde{C}] & [G] \\ [G]^T & [0] \end{bmatrix} \begin{Bmatrix} \{V\}_1 \\ \{P\}_1 \end{Bmatrix} = \begin{bmatrix} \{F\} \\ \{0\} \end{bmatrix} \qquad (3.2.22)$$

where $\{\tilde{F}\}=\{F\}+b_0[M]\{V\}+b_1[M]\{\dot{V}\}$ (3.2.23)

and $[\tilde{C}]=[C]+b_0[M]$ (3.3.24)

$b_0=1/[(\phi)(\Delta t)]$ (3.2.25)

$b_1=(1-\phi)/\phi$ (3.2.26)

For this case

$$[\tilde{A}] = \begin{vmatrix} [\tilde{C}] & [G] \\ [G]^T & [0] \end{vmatrix} \qquad (3.2.27)$$

is symmetric.

The system 3.2.22 can now be written

$$[\tilde{A}]\{Y\}=\{\tilde{B}\} \qquad (3.2.28)$$

where $\{Y\}^T=[\{V\}^T,\{0\}^T]$.

3.3. DISCUSSION OF ELEMENT SELECTION.

The global matrix $[\tilde{A}]$ in equation 3.2.28 is built conveniently by joining the nodal points by lines so as to form elements of the material. The required matrices can then be formed for each element in turn and assembled into the global matrix.

The standard four node isoparametric quadrilateral element was chosen for the application in this work (ref. 10). This element was selected since it is the simplest finite element that can deform under plane strain conditions with constant volume. The basis functions to be listed below are bi-linear for the velocity field and unity for the pressures (or the mean normal stresses). The pressures will thus be constant for each element and hence discontinuous between elements.

The element matrices for the four node quadrilateral are formed conveniently by mapping a distorted quadrilateral to a unit square as depicted on the following page.

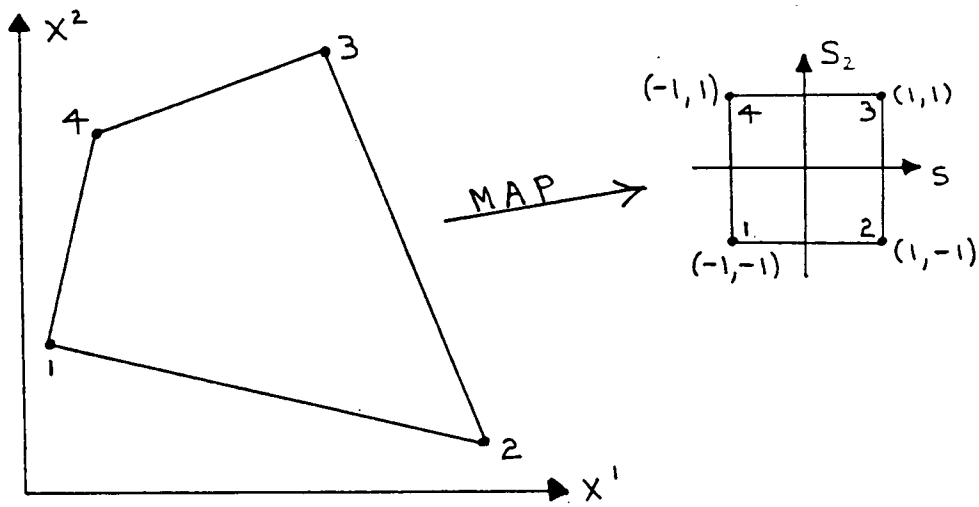

FIG. 3.3.1
Illustration of the mapping to s^1, s^2 coordinates of a 4 node quadrilateral element

The basis functions are written in the s_1 and s_2 coordinate system as

$$\phi_1=(1-s_1-s_2+s_1 s_2)/4 \qquad (3.3.1)$$

$$\phi_2=(1+s_1-s_2-s_1 s_2)/4 \qquad (3.3.2)$$

$$\phi_3=(1+s_1+s_2+s_1 s_2)/4 \qquad (3.3.3)$$

$$\phi_4=(1-s_1+s_2-s_1 s_2)/4 \qquad (3.3.4)$$

The mapping function from the local s_I coordinates to the global x_I coordinates is defined as

$$x_I = (s_1, s_2)X_{QI} \qquad (3.3.5)$$

where X_{QI} is the I'th coordinate of node Q and x_I is the I'th coordinate of any other point in the material. All element integrations can then be carried out over s_I coordinates instead of x_I on using the Jacobian of the transformation 3.3.5. The integrations are carried out using Gaussian integration which involves a sum of values over selected points in the element.

3.4. SPECIFICATION OF GEOMETRY.

The figure below illustrates how the nodal point numbering and coordinate data is used to specify the material geometry.

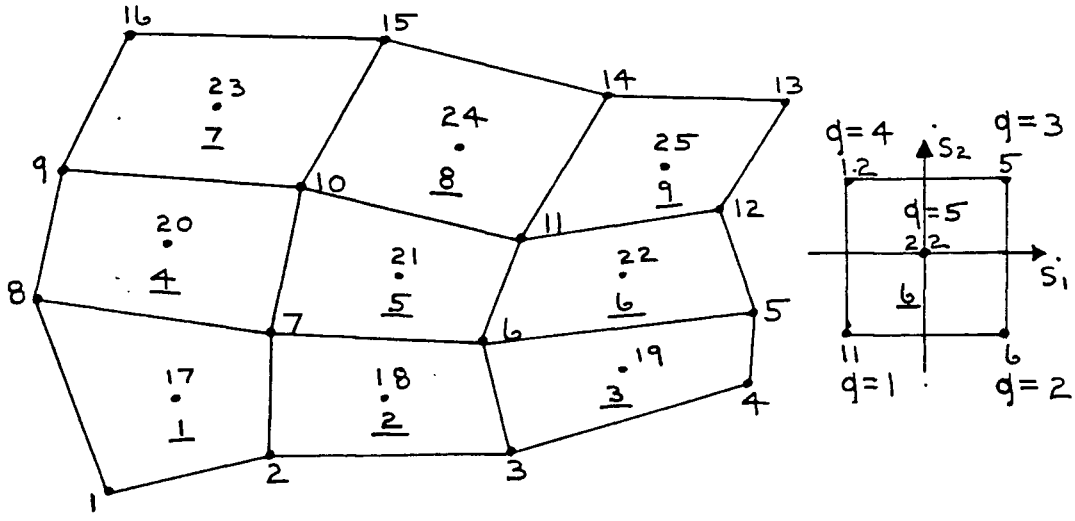

FIG. 3.4.1
Illustration of nodal point numbering for elements.

The connectivity data consists of an array C_{eq} which gives the global node number of the q'th local node in element e. For element 6 for example, C(6,1)=11, c(6,2)=6, C(6,3)=5, C(6,4)=12, and C(6,5)=22. The pressure node, for the linear quadrilateral element (local element node number 5) is always assumed to be at the centre of the element.

The coordinate data can be specified in the array as X_{QI} which gives the I'th coordinate at the global node Q. Thus X_{QI} with $Q=C_{eq}$ would give the I'th coordinate of the q'th local node (Q'th global node) in element e.

The coordinate and connectivity data is thus sufficient to define the region over which the solution is required.

3.5. MATERIAL CONSTITUTIVE BEHAVIOR.

Equation 3.2.8 relates deviatoric stress to deformation rate with a coefficient of viscosity. All quantities are defined except the functional relation of the yield stress indicated in equation 3.2.6. The functional relation to be assumed is specified below. The flow rule and other definitions are re-stated for completeness.

$$s_{ij} = \gamma D_{ij} \qquad (3.5.1)$$

$$\gamma = (2Y)/(3\bar{D}) \qquad (3.5.2)$$

$$Y = (1+c_1\bar{e})^{\gamma}[Y_o + c_2(D-\bar{D}_o)^{c_3}] \text{ if } \bar{D} > \bar{D}_o \qquad (3.5.3)$$

$$Y = \alpha\bar{D} \text{ if } \bar{D} \le \bar{D}_o \qquad (3.5.4)$$

$$\text{where } \bar{D}_o = (1+c_1\bar{e})^{\gamma} Y_o/\alpha \qquad (3.5.5)$$

Here c_1, γ, c_2, c_3 are constants for the material. α is an initial constant slope on the Y against $\bar{D}$ curve to prevent $Y/\bar{D}$ from becoming infinite as $\bar{D} \to 0$.

Graphically the assumed constitutive behaviour is as illustated in Fig. 3.5.1 on the following page.

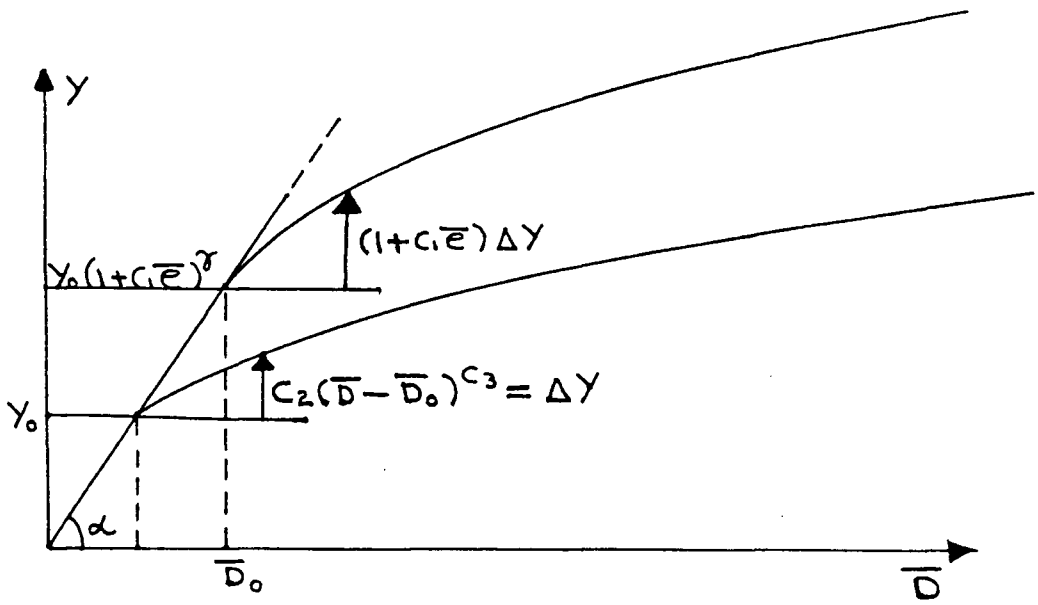

FIG. 3.5.1
Illustration of the constitutive behavior assumed.

The static yield stress for material that has an effective strain $\bar{e}$ is $Y_0(1+c_1\bar{e})^{\gamma}$. If $c_1 \neq 0$ strain hardening will thus occur. The yield stress may also be strain rate sensitive. In this case it is assumed that the annealed yield stress increases by $c_2(\bar{D}-\bar{D}_0)^{c_3}$. The suggested combined effects of strain rate sensitivity and strain hardening was not used in any of the calculations. Only the separate cases of strain hardening with no strain rate sensitivity ($c_2=0$) or strain rate sensitivity with no strain hardening ($c_1=0$) were assumed.

It was established that equation 3.5.3 was sufficient to account for the variation of the yield stress of aluminum with strain hardening and also the yield stress of plasticine with strain rate sensitivity. These materials were used in this work to compare the computer code predictions with experimental results.

3.6. ELEMENT ASSEMBLY

The process of element assembly can be indicated as follows. If $A^e_{qrst} Y^e_{st} = B^e_{qr}$ represents the algebraic equations for a single element only and $A_{QRST} Y_{ST} = B_{QR}$ that for the total structure, then

$$A_{\underline{QR}\,\underline{ST}} = \sum_e A^e_{\underline{qr}\,\underline{st}} \qquad (3.6.1)$$

$$\text{and } B_{\underline{QR}} = \sum_e B^e_{qr} \qquad (3.6.2)$$

where $Q = C_{eq}$ and $S = C_{es}$.[1]

On referring to equation 3.2.22 it can be seen that [A] contains elements of [C] and [G]. In the computer code it is important to be able to selectively assemble [C] or [G]. For example, on iterating with respect to material viscosity, only [C] changes from one iteration to the next. [G] and $[G]^T$ are independent of viscosity and only change when the material is incrementally strained. Thus only [C] needs to be updated on an iteration. If inertia is not being considered then the update for viscosity change is easily done since [M]=0 and $[\tilde{C}]=[C]$ from equation 3.2.24.

---

[1]Here $A_{\underline{QR}\,\underline{ST}}$, which is an element of [A], can be considered an influence coefficient between the Qr'th and St'th global solution variables. Qr refers to the r'th solution variable at global node Q and St to the t'th solution variable at global node S. Similarly, at the element level, $A^e_{\underline{qr}\,\underline{st}}$, which is an element of $[A]^e$, can be considered an influence coefficient between the qr'th and st'th element solution variables. qr refers to the r'th solution variable at element node q and st to the t'th solution variable at element node S. In the present formulation there are 2 velocity components at velocity nodes and one pressure at pressure nodes.

If inertia is being considered, however, it is useful to be able to take advantage of the fact that [M] is independent of viscosity and does not have to be recalculated on iterations.

The usual procedure followed in the code for assembly is as follows. On the first iteration of an increment (which occurs on the first run or just after the material has been incrementally strained) assemble, for each element, $[C]^e$, $[G]^e$, $[M]^e$, and $[F]^e$. Then form $[\tilde{C}]^e$ from equation 3.2.24 and $\{\tilde{F}\}^e$ from equation 3.2.23. Then form the total element matrices $[\tilde{A}]^e$ and $\{\tilde{B}\}^e$ and assemble into the global matrices to give $[\tilde{A}]$ and $[\tilde{B}]$. While assembling the element matrices also form [M] as a separate global matrix. On the remaining iterations after the first on an increment assemble only $[C]^e$ into [A]. After this assembly add $b_o[M]$ into the [C] submatrix of [A] to form $[\tilde{A}]$.

The procedure outlined above avoids a reformulation of [M] and $\{\tilde{B}\}$ which do not change when viscosity only is updated after an iteration on an increment. They only change when the material is incrementally strained.

3.7. BOUNDARY CONDITIONS.

Much of the material in this section has been specially formulated for this work. Reasonably full details will thus be given.

3.7.1. Specified Velocity and Mean Normal Stress

As a result of the discretisation process, the continuum problem governed by the equations of motion and continuity has been replaced by a discrete problem governed by a system of algebraic equations of the form.

$$[A]\{Y\}=\{B\} \qquad (3.7.1.1)$$

Before insertion of any boundary conditions the matrix [A] will be singular. Sufficient boundary conditions must be supplied to define the problem; in particular, all rigid body motions must be removed. Several different types of boundary conditions will be outlined in subsequent sections.

Let $\{Y\}^T$ be written $[\{Y\}_1^T, \{Y\}_2^T]$ such that $\{Y\}_1^T$ contains unknown velocities and pressures and $\{Y\}_2^T$ contains specified velocities and pressures. The sub-system

$$[A]_{11}\{Y\}_1=\{B\}_1-[A]_{12}\{Y\}_2 \qquad (3.7.1.2)$$

represents the system of equations that is to be solved for non specified variables. The solution $\{Y\}_1$ will automatically reflect the requirement of the specified nodal variables. The solution $\{Y\}_1$ found subject to the specified $\{Y\}_2$ will not in general satisfy the remaining part of the system 3.7.1.1 namely

$$[A]_{21}\{Y\}_1=\{B\}_2-[A]_{22}\{Y\}_2 \qquad (3.7.1.3)$$

The residuals for each equation in 3.7.1.3 can be interpreted as the reaction (a force for velocity or flow rate for pressure) that is required to give the specified variable to which the equation refers.

From a computational standpoint it may be convenient to solve for these reactions directly. This can be done by

writing the system 3.7.1.1 in the form

$$\begin{bmatrix} [A]_{11} & [0] \\ [A]_{21} & -[I] \end{bmatrix} \begin{bmatrix} \{Y\}_1 \\ \{R\} \end{bmatrix} = \begin{bmatrix} \{B\}_1 - [A]_{12}\{Y\}_2 \\ \{B\}_2 - \{A\}_{22}\{Y\}_2 \end{bmatrix} \qquad (3.7.1.4)$$

Thus only a transformation on the matrix [A] and load vector {B} is required in order that the solution of the transformed system yield reactions in place of specified variables. If required, the symmetry of [A] can be preserved by setting $[A]_{21}$ to zero and replacing {R} by {X} say. After solution when {Y} and {X} have been calculated, {R} can be found from

$$\{R\} = [A]_{21}\{Y\}_1 + \{X\} \qquad (3.7.1.5)$$

In practice it may be more convenient to adopt the approach discussed above for solving for the reactions directly rather than solving the sub-system 3.7.1.2 separately. This situation occurs since only a permuted form of [A] is stored inside the computer and also advantage must be taken of the banded structure of the matrix.

3.7.2. Surface tractions.

To account for surface traction, equivalent nodal forces must be formed by an integration over the sides of the elements. The results are then added into the load vector $\{\tilde{F}\}$ in equation 3.2.22. Should adjacent elements have surface traction or the same element have surface traction on more than one side, then this addition process will finally result in the complete load vectors for surface traction being formed.

3.7.3. Platen Friction

In the system of equations 3.7.1.2 1 a subscript 1 variables and 2 known variables.

$$[A]_{11}\{Y\}_1=\{B\}_1-[A]_{12}\{Y\}_2 \qquad (3.7.3.1)$$

could be solved as a separate system and is interpreted as the solution for {Y} subject to the applied force vectors {B} and additionally $-[A]_{12}\{Y\}_2$. The latter force vector can be interpreted as the external forces that must be applied to make the variable {Y} consistent with the applied constraints. The residuals

$$\{R\}=[A]_{21}\{Y\}_1+[A]_{22}\{Y\}_2-\{B\}_2 \qquad (3.7.3.2)$$

are the generalised forces that are required to achieve the constraints.

Coulomb friction essentially relates the normal stress between two surfaces, F_N, to the shear stress, γ, that results due to sliding contact by a coefficient of friction according to the following relationship

$$\gamma=\eta F_N \qquad (3.7.3.3)$$

If now motion of a boundary is specified in the normal direction then a normal reaction results. The coefficient of friction times the reaction will then be a load vector that should constrain the sliding motion of the surface.

Let node W be one of the nodes where friction is to be supplied. Let 2 be the degree of freedom in which velocity is to be specified and hence the direction of the normal reaction. The Figure below summarises the notation for the application being considered.

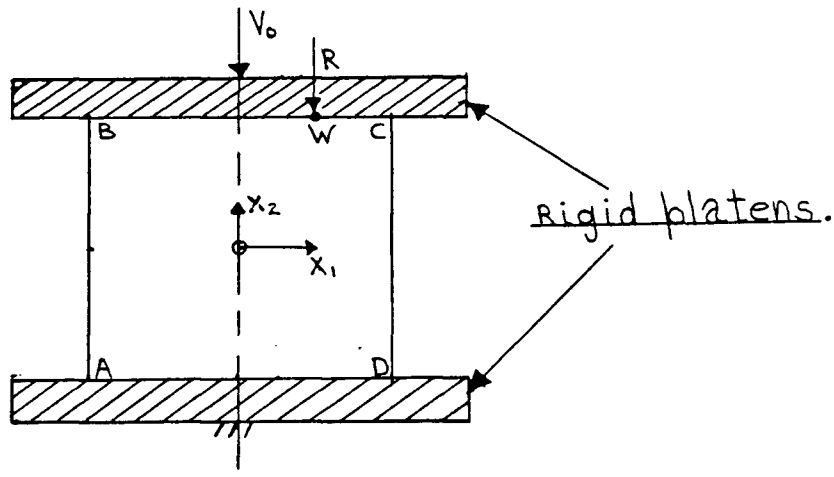

FIG. 3.7.3.1
Illustration of the compression in plane strain of a block of material between two platens.

Specification of v_o will give a normal force on the top face BC of the specimen. The equation of motion of node W in the second degree of freedom occurs in the system 3.7.3.2 while the equation that governs motion in the first degree of freedom at W will occur in the system 3.7.3.1. Now R is a vertical reaction force that results when the velocity v_o is specified. The coefficient of friction, denoted by γ_p, times this reaction must be added into the load vector of the equation that governs motion of node W in the horizontal direction. This constraint on sliding is conveniently applied by putting $-\gamma_p$ into the diagonal of [0] in equation 3.7.1.4 in the row for the horizontal degree of freedom at node W.

During the course of a solution, after every iteration on every increment, the status of all platen friction nodes is examined. On the first iteration of the first increment

in the code all surface nodes under the platens are made to stick to the surface by imposing velocity constraints. From the horizontal reactions that result the direction that nodes want to move in can be determined. Depending upon the magnitude of the vertical reaction a node is either left stuck to the surface or allowed to slide. Sliding is allowed if the estimate of the frictional force that would hold if the node were released is less in magnitude than the sticking reaction force. It is then assumed that the node could slide with the friction force acting in the direction opposite to that of motion along the surface. On iterations after the first, if a node is found to be sliding in the same direction as the friction force, it is constrained to a stick condition.

The code includes routines that allow a completely arbitrary boundary movement. Nodes can stick to the platens, slide along the platens, or move away from the platens. Nodes already free are automatically restrained if they again reach the platens.

Until now boundary friction has been discussed with the assumption that the coefficients of friction at the platen friction nodes are known. If this is not the case it is then of interest to be able to predict the coefficients of friction based upon information about boundary velocities in the sliding direction. What we have called the Master-Slave Node Method is one approach and is discussed. Before doing this it should perhaps be stated that the prescription of boundary velocities all along a surface where friction acts would not in general be

satisfactory. This procedure effectively totally constrains the boundary and forces it to move in a way that may not be consistent. For example, with the assumed constitutive behaviour it is much better to minimise the boundary constraints and predict the observed motion. A second approach might be to solve the problem several times with different coefficients of friction and then to predict the best one by interpolation. This technique would, however, require solving the problem several times. The Master-Slave Node Method overcomes both these difficulties.

The method first requires the choice of a boundary node where friction acts. The success of the method is dependent upon the sliding velocity of the node being sensitive to friction conditions along the whole platen boundary. In the present application this node occurs at the top right hand corner of the specimen and is illustrated in the following figure on the next page.

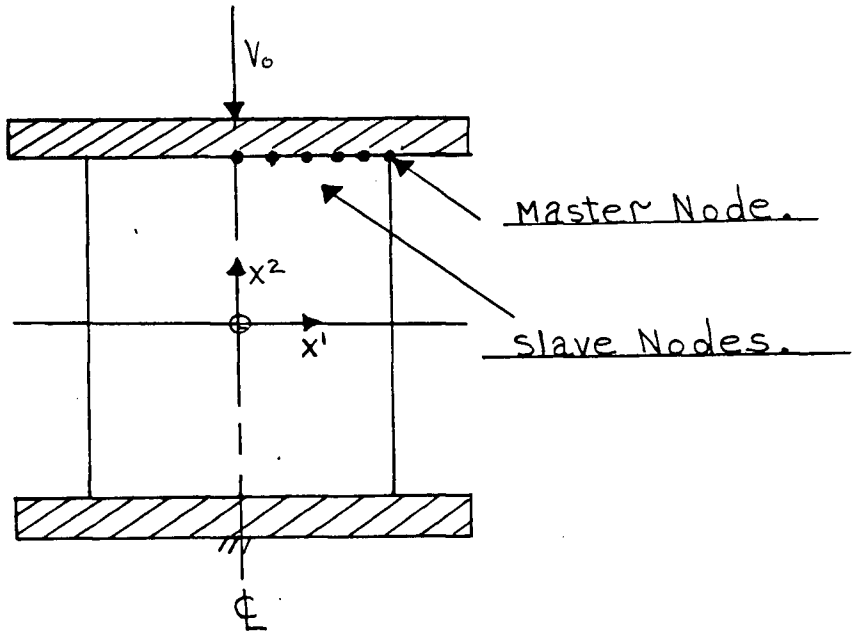

FIG. 3.7.3.2
Illustration of the top right hand quadrant of a specimen with the slave friction nodes and the master friction node shown.

The basic idea of the method is to impose the measured x^1 component of velocity at the master node and then to adjust the coefficients of friction at the friction nodes until the ratio of the tangential to the normal reactions at the master node becomes equal to the coefficient of friction at the slave nodes. The calculation will now be briefly outlined.

Let F be the sum of the tangential friction forces of the sliding slave nodes along a platen and let R be the tangential reaction of the master node. A coefficient of friction, η, is calculated from $\eta=(F+R)/(R_S+R_M)$ where R_S is the total vertical (or normal) reaction of the slave nodes and R_M is the vertical reaction of the master node.

Corrections to η are made on the basis of the ratio for sliding nodes of the total tangential force to the total normal force. It was found numerically that $|R/R_M|$ approached η on iterations.

3.7.4. Glass Friction.

During the solution of the system of equations 3.2.22 the nodal pressures are obtained as basic solution variables. This pressure is the mean normal stress and , for plane strain conditions, is the pressure distribution that the glass plates enforce on the material. The assumption of Coulomb friction allows a shear stress to be calculated from this normal pressure. An integration over the face of each element in contact with the glass plates then allows a set of consistent nodal forces to be calculated from the principle of virtual power. These nodal forces will be referred to the velocity nodes and will be related directly by matrices to be derived to pressures at pressure nodes. This latter fact will allow the load terms to be added to the equations on the left side rather than the right by a transformation on the global matrix that involves subtracting terms off the constraint matrix [G] in equation 3.2.22. As this approach is entirely unique to this work full details will now be presented.

Fig. 3.7.4.1 depicts material deforming in plane strain between glass plates.

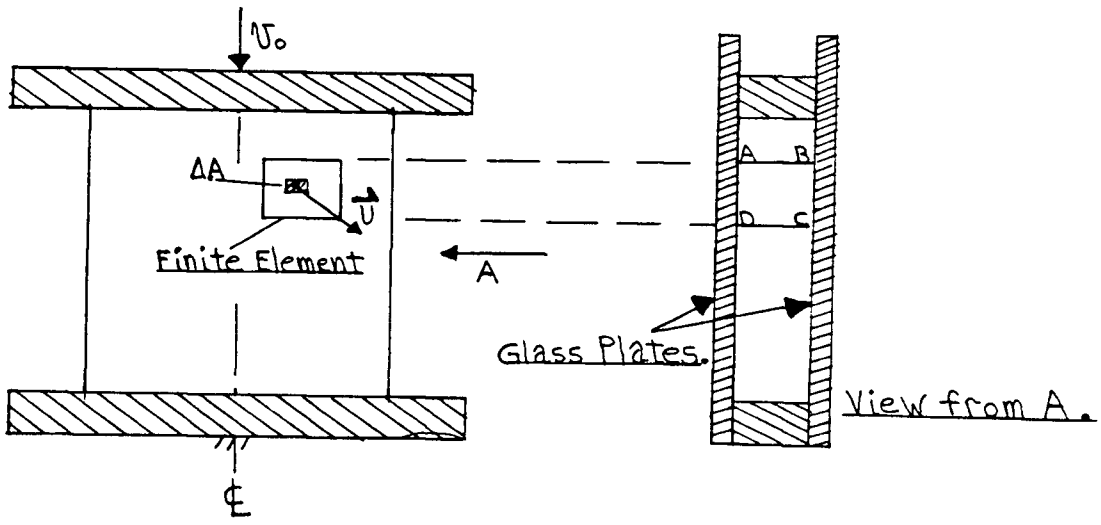

FIG. 3.7.4.1
Illustration of material deforming in plane strain between glass plates.

The small area ΔA is contained within a finite element e and is sliding between the glass plates in a direction given by the unit vector u_i. The glass friction, which acts on both sides of the element, must be in the direction $-u_i$. On taking into account that the pressure, P, exerted by the glass plates is negative when compressive one can deduce that the net glass friction force ΔF_i acting on the material ABCD with area ΔA in contact with the front and back plates is

$$\Delta F_i = -2\eta_g P u_i \Delta A \qquad (3.7.4.1)$$

where η_g is the coefficient of friction for the material being compressed for sliding along the glass plates.

If δv_i is an arbitrary virtual variation of velocity for the differential element the virtual power involved will be $2(\eta_g P u_i \Delta A)\delta v_i$. If this differential power is integrated over the finite element the virtual power, $\delta \dot{W}^e$,

associated with the element is obtained as

$$\delta \dot{W}^e = 2\int_{A^e} (\eta_g P u_i \delta v_i)\, dA^e \qquad (3.7.4.2)$$

where the integration is taken over one face of the finite element in contact with the glass. The series expansions $v_i = \Psi_\varphi (v_\varphi)_i$ and $\Psi_L P_L$ for velocity and pressure as given in equations 3.2.11 and 3.2.12 can be substituted into 3.7.4.2 to give

$$\delta \dot{W}^e = [2\int_{A^e} (\eta_g u_r \Psi_\varphi \Psi_L)\, dA^e] P_L \delta V_{\varphi R} \qquad (3.7.4.3)$$

where u_i is the unit vector in the direction of the particle velocity v_i.

The glass friction acting over the element e is thus equivalant to a generalised force vector $F^e_{\varphi r}$ such that $\delta \dot{W}^e = F_{\varphi r} \delta V_{\varphi r}$, where $\delta V_{\varphi r}$ is a virtual nodal force velocity vector. Thus

$$F^e_{\varphi r} = [2\int_{A^e} (\eta_g u_r \Psi_\varphi \Psi_L)\, dA^e] P_L \qquad (3.7.4.4)$$

where $F^e_{\varphi r}$ is the r'th component of generalised force at node Q. This can be written in matrix notation as

$$\{F\}^e = [X]^e \{P\}^e \qquad (3.7.4.5)$$

On assembling the force vector in 3.7.4.5 into the equation 3.2.22 one obtains the system

$$\begin{bmatrix} [\tilde{C}] & [G]-[X] \\ [G]^T & [0] \end{bmatrix} \begin{bmatrix} \{V\}_1 \\ \{P\}_1 \end{bmatrix} = \begin{bmatrix} \{\tilde{F}\} \\ \{0\} \end{bmatrix} \qquad (3.2.22)$$

Thus a transformation on the matrix [A] in equation 3.2.28 is required to account for glass friction once the

equivalent element load vectors have been calculated.

Additional constraints are required if both sticking and sliding friction are to be accounted for. Let v_i denote nodal velocity, F_i nodal force due to sliding friction, and R_i nodal reaction calculated for a stick condition. The following criteria were found to be satisfactory.

A). If the node is sliding calculate $v_i F_i$. If $v_i F_i > 0$, apply a velocity restraint of zero to simulate a stick condition. Otherwise continue to allow the node to slide. In the case of nodes in contact with the platens this criterion is not used. In this case the glass friction force is added onto the platen friction force and then the decision on recapture to a stick condition made by the platen friction routines as outlined in section 3.7.3.

If an external boundary condition exists at the nodes, such as the downward velocity of the top platen, then the boundary condition is maintained regardless of the glass friction since it is then implicitly assumed that the required external force to maintain the velocity constraint is always being applied.

B). In the case of a node that is stuck to the glass plates the angle θ between R_i and F_i is calculated from $\cos^{-1}[R_i F_i/(|R_i||F_i|)]$. If θ is between 90° and 270° it is assumed that the node would move in the direction of the velocity if released. In this case it is thus constrained to zero velocity. If the angle θ is less than 90°, it is allowed to slide provided also that $|F_i| < |R_i|\cos(\theta)$. This

latter check is to estimate whether the reaction force in the direction of F_i is less than the magnitude of F_i. Again platen friction nodes are dealt with by platen friction routines with the glass friction force taken into account.

An additional consideration that arises in the treatment of glass friction is the case where an element has all of its velocity nodes constrained to a stick condition. In this case the element pressure (which is constant for the four node quadrilateral) becomes indeterminate. This situation occurs beacause the continuity equation is satisfied automatically and the incompressibility constraint cannot be invoked by determining the element pressure. Computationally, application of the method described in section 3.7.1 for transforming the matrix [A] to constrain boundary condition velocities for the element would lead to a line of zeros in the matrix making it singular. In this case the element pressure previously calculated for the element is applied as a boundary condition. The procedure outlined in section 3.7.1 then leads to a flow rate being determined as a reaction. For a stick condition, the flow rate would be determined as zero thus satisfying continuity. The advantage of this procedure is that the singularity is easily removed in the calculation.

3.8. NONLINEAR GEOMETRY.

A piecewise constant incremental approach was adopted for taking into account the geometry change of the finite element meshes due to strain. The velocity field was calculated keeping the finite element mesh fixed and then the velocities were multiplied by a time increment to give a new distorted mesh. The velocities would then be re-calculated and the process repeated.

The time increment was automatically controlled by the program. The user specifies the maximum strain he will tolerate. The program will then automatically choose the time increment to keep the strain at the specified tolerance.

The piecewise constant geometry approach neglects certain terms that would occur in a piecewise linear approach. During mesh distortion, for example, the principal stress vectors rotate and change in magnitude. Incremental stresses thus result that, in the piecewise constant approach, were not taken into account in the virtual power equation. Since these incremental stresses do contribute to the power the size of the strain increment must be small enough to make these incremental stresses negligible.

CHAPTER 4

THE EXPERIMENTAL STUDY.

4.1. INTRODUCTION.

In the experimental work a study was undertaken of the rapid plane strain compression of a rectangular block of plasticine between flat, parallel, and rigid platens. Specimens of various height to diameter ratios (H/D) were used and different compression speeds selected. Specimen deformed profiles were examined from high speed photographs taken at wide range, and detailed boundary motion was examined from high speed photographs taken at close range.

The experimental results obtained are used as a basis of comparison with the results of calculations obtained with the finite element code discussed in chapter 3.

The details of the experimental work are outlined in the following sections. In Section 4.2 the equipment used is discussed. In Section 4.3 an outline of the test procedure is discussed. In Section 4.4 the procedure followed to calibrate effective stress to effective strain rate for plasticine is discussed. Finally, in Section 4.5, the experimental results are presented and general observations made regarding the deformation patterns.

4.2. EQUIPMENT.

A photograph of the Dynamic Impact Press (DIP) is given in Fig. 4.2.1.(a), and a schematic drawing of the DIP is shown in fig. 4.2.1(b). This press was designed and built by the author's advisor Professor G.W.Vickers. It consists of a large motor driven wheel attached to a Whitworth quick return mechanism. The main purpose of the

drive wheel was to drive a cam along the cam guides. At each end of the cam guides were placed optical sensors , OS1 and OS2, which enabled a sequence of electronically controlled events to occur during a test.

Prior to initiation of the test cycle the cam just freely moved up and down the cam guides as the drive wheel rotated. When the test sequence was initiated, OS1 was activated. When OS1 detected the cam the solenoid was energised. When the cam next reached the top of the cam guides, the solenoid mechanism engaged and the cycloidal cam was pulled down through the cam followers. This in turn caused the upper platen to move down with constant velocity onto the specimen. When the cam, which was now attached to the cycloidal cam, again reached the top of the cam guides the cycloidal cam was released.

In order to photograph specimens under dynamic conditions, high speed photography at about 2000 frames per second (FPS) was required. The high speed camera used was a Hycam rotating prism type which used 16mm film and was capable of operating at 10,000 FPS. The camera was designed to pull the film through a film gate at high speed with the image reflected onto the film by a rotating prism.

Of importance to this work was the capability of synchronizing the camera start pulse to the compression of plasticine by the platen. Fig. 4.2.2 shows a schematic diagram of the logic of the electronic circuit designed for

this purpose.[1] When the system was enabled by pressing a button (P/B) a preset camera start delay was initiated when the cam reached OS2 in Fig. 4.2.1(b). The time taken for the cam to move between OS1 and OS2 was the time base for this delay. When the cam reached OS1 the solenoid was activated to enable the cam to engage the cycloidal cam. The sequence then previously described proceeded. The camera started after the preset time delay and stopped when the end of film was detected. After the impact, the solenoid was released when a mechanical micro switch (MS) was reached by the cam. This action allowed the cam to disengage when it next reached the solenoid.

The preset time delay for the camera was set manually using the Synchronization Control shown in Fig. 4.2.2. The indicator flashed when the two pulses from OS1 and OS2 indicated that the camera advance setting was correct.

Fig. 4.2.3 shows a schematic drawing of the specimen holder. This arrangement was designed by the author with the objective of enabling a wide field of view for the camera lens with impact at maximum speed onto the specimen. Adjacent to the specimen holder is shown a graph of upper platen velocity against displacement. The curve shows that over most of the displacement path the velocity was constant.

Fig. 4.2.4. illustrates the experimental arrangement that was used for compressing specimens in plane strain.

---

[1] Courtesy of John Richards, Electronics Technician, University of B.C.

The front view shows a plasticine specimen in position. The specimens were typically 3 inches high, 1.5 inches wide, and 1.375 inches thick. Squares of 1/8 in. were also drawn on the surfaces to enable the movement of points to be followed. Scales were mounted on the glass plates in front of the specimens and also on the upper platen. These scales enabled velocities and distances to be determined on the photographs.

The side view in Fig. 4.2.4 shows the specimen between the glass plates. The platen shown deformed the specimen by passing between the glass plates.

Also shown in Fig. 4.2.4 are velocity and displacement transducers. The displacement transducer is essentially a linear variable differential transformer with a 6V DC power supply to a solid state oscillator. The velocity transducer operated by magnetic induction and this required no power supply. The outer casing is magnetised and the self-induced voltage was proportional to the velocity of the inside coil through the magnetic field.

A DMS 510 Digital Memoryscope with a single channel could be connected to the displacement transducer, velocity tranducer, or load cell for direct recording and subsequent plotting.

Fig. 4.2.4 also illustrates a typical lighting arrangement used with the camera in position. A high intensity light was required for the film speeds used. The camera had a tele-photo lens attached which enabled very close examination of the specimens during deformation.

Fig. 4.2.5 shows some characteristics of the high

speed camera obtained from an examination of timing marks on the film. 100 ft of film was able to travel through the camera in about 1.5s. Since only 26ms was typically required for the traversal of the upper platen from the highest to the lowest position, there was adequate time for the specimen deformation to be captured on only a few feet of film. During specimen compression the film speed would usually be about 2300 FPS.

In Fig. 4.2.6 is shown calibration curves obtained for displacement and velocity transducers. It was confirmed that the manufacturer's specifications on linearity were met over the region tested. Fig. 4.2.7 shows a calibration curve for the load cell. The loading in this case was carried out on a Tinius Olsen Mechanical Load Testing Machine capable of loading accurately to 60,000 pounds. From the series of detailed calibration curves constructed the load cell was found to be accurately linear to the maximum specified loading value of 25000 pounds.

4.3. TEST PROCEDURE.

4.3.1. Introduction.

The test procedure involved a). Preparation of specimens, b). Photographing the specimens being deformed and developing the film, and c). Viewing the film and digitising the results.

4.3.2. Preparation Of Specimens.

Plasticine specimens were prepared by first cutting them to shape with a thin strand of wire. The grid lines were marked on the plasticine with a Staedtler Lumocolor pen. As the ink flows from the tip of this pen by venturi action minimal pressure was required between the tip and the surface. The ink was absorbed into the plasticine. It was found that the grid patterns were quite resistant to shearing stresses from the glass plates provided no lubrication was applied to the plasticine specimen. Lubrication with light oil tended to absorb a thin layer of plasticine with the result that the grid patterns were destroyed with only a small amount of movement.

4.3.3. Photographing The Specimens And Developing The Film.

In carrying out the tests a systematic procedure was essential since a considerable amount of preparatory work could easily be lost. The following steps were systematically followed during testing. Fairly specific details are given for completeness.

1. The impact press drive motor and electronic control system were connected to the main power supply.
2. The Bridge Amplifier Meter (BAM) was balanced. The BAM was a Wheatstone Bridge attached to the strain gages in the load cell. A final balance was carried out when the BAM had reached a steady state thermal condition.
3. The plasticine specimen was next placed in the impact press specimen holder with the glass plates in

position. If required, the lower platen was lubricated before putting the specimen in position.

4. With the floodlights on for as short a time as possible, the camera was focused with a detachable focusing prism and the aperture set after measuring the light intensity with a lightmeter. The focusing prism was then inserted directly in the film gate position and the image that would reach the film observed. Any positioning adjustments were then made.
5. The camera was next loaded with the film. 100ft rolls of Eastman 4-X Negative Film 7224 were used. This is 16mm film prepared specially for high speed cameras.
6. The camera supply voltage was set (usually to 75V), and the film timing light generator was turned on usually at 1000 pulses per second (PPS). The timing marks placed on the film by the pulse generator allowed the film speed to be determined.
7. The BAM balance was next re-checked, and the digital storage scope made ready for accepting the pulse from the load cell during impact. The scope was adjusted to self trigger at an early point on the load pulse and a sweep time of 10ms per scope division was used.
8. The impact press drive motor was next started to give a specimen impact speed of usually 4m/s. The synchronization timer for the camera advance was then set.
9. The camera supply variac was next turned on. This was not done previously to avoid having the camera start early because of an extraneous pulse during the

starting procedure.

10. Finally the floodlights were turned on and the scope rechecked to ensure that no extraneous pulse had caused it to trigger early. The automatic photographing sequence previously described was then enabled.

11. On completion of the test, a hard copy of the load trace captured by the storage scope was obtained by attaching an X-Y recorder (model WX4400, Watanabe Instruments Corp). A photograph of the scope screen would also usually be taken as an additional record.

12. Finally, the film was removed from the camera and developed in a developing tank (Nikor Film Processing Machine) using Kodak D-76 developer (6 minutes at 70°F), a Glacial Acetic Acid stop bath (1 minute), and Kodak Rapid Fixer (10 minutes). This processing was followed by 30 minutes of washing in running water.

4.3.4. Viewing The Film And Digitising The Results.

After the film was developed it was examined using a 16mm Athena Model 224 projector. This projector could display single frames and be pulsed at an arbitrary rate in either direction. The images were projected directly onto drawing paper at a reasonable size and the grid patterns sketched directly over the images. From various vertical and horizontal scales attached to the specimen holder on the impact press, the scale factor for each drawing could be found . It was established that there was no significant optical distortion in the projected frames. It was also

established that the heat from the projector lamp when left on a stationary frame for longer than would be required in sketching produced no detectable movement of the image.

After sketching the specimen grid patterns for a series of frames (usually corresponding to equal time intervals) and establishing the scale for each frame, the coordinates of the points on the surface defined by the intersection of grid lines were found with the use of a digitising machine supported by the UBC Computing Centre. The coordinates of the points for a series of grid patterns could then be used to plot, for example, a series of path lines or a velocity field.

4.4. CALIBRATION OF PLASTICINE.

Aku, Slater, and Johnson(31) found that plasticine is very strain rate sensitive but essentially not strain hardening. While ref. 31 gave several calibration curves for plasticine, it was decided to do, as part of this work, a calibration of effective stress to effective deformation rate for the plasticine to be used in the experimental tests.

Axisymmetric cylinders of plasticine were used for calibration purposes. The main objective was to deform cylinders of various diameters but of the same height so as to obtain a range of loads for the same deformation rates.

Fig. 4.4.1 shows two examples of the plasticine cylinders used with the final results of the deformation shown for interest. Fins were moulded on the sides of one of the specimens to enable the boundary to be clearly defined on the high speed photographs. Radial lines drawn

on the tops of the cylinders was an indication that the deformation was reasonably axisymmetric over the whole compression.

The series of photographs shown in Fig. 4.4.2 are examples of the compression of the plasticine cylinders. The film timing marks and the scales attached to the load cell enabled platen velocities to be determined. The photographs in fig. 4.4.2 show that the boundary remained quite straight during the deformation. The heights shown on the photographs were determined from the scale factor as were also the diameters. A check on volume constancy was carried out by calculating the diameters of the specimens assuming uniform compression. The results are shown in brackets above the measured diameters in Fig. 4.4.2. Comparison of the predicted and measured diameters show reasonable agreement.

A typical displacement against time curve for the upper platen is shown in Fig. 4.4.3. A series of marks along the curve show the positions that were used for calibration. The zero point on the time axis was chosen as the position of maximum velocity which occured at approximately the centre position between the limits of displacement. The velocity at any point is the instantaneous slope of the curve which varies slightly over the region of deformation. The piecewise linear approximations A-B, B-C, C-D, and D-E were used to estimate the velocities for the various photographs.

Fig. 4.4.4 shows the load trace with the positions of the frames selected for calibration purposes. With the

velocity of the upper platen known at any point in the deformation together with the specimen height and load, it was possible to calculate both the effective stress and effective deformation rate. The calibration data obtained is plotted in Fig. 4.4.5.

4.5. EXPERIMENTAL RESULTS.

4.5.1. Introduction.

The experimental work was done on plasticine to observe the deformation profiles and measure the platen loads throughout the straining history. The results obtained are compared to finite element predictions in chapter 5.

4.5.2. Experimental Tests.

For all tests, the procedure outlined in Section 4.3 was followed. The tests to be discussed are listed below. Each test will then be considered in detail.

Test 1. Plane strain compression at a platen speed of 4.4m/s of an unlubricated specimen with the standard dimensions of 3in. high, 1.5in. wide, and 1.375in. thick between glass plates with the full specimen in the field of view of the camera.

Test 2. An identical test to 1 but with the camera at close range to the top platen. This test was carried out to observe the details of the motion along the platen boundary.

Test 3. This test was a repeat of test 2 but with household oil as a lubricant for the platens.

Test 4. This test was identical to test 1 but with a

platen speed of 2m/s.

Fig. 4.5.2.1 summarises the results of test 1. The top of the specimen deforms the most initially but movement at the base of the specimen increases as the deformation proceeds.

The results were digitised from enlarged sketches taken from the projector image as discussed in Section 4.3.4. From the digitised results, a computer plot of the path lines was obtained. This plot is given in Fig. 4.5.2.2. The lines join the instantaneous positions of selected nodes in the material and reveal that the top surface remained stuck to the upper platen for the first three photographs used (frames 3, 5, and 6 in Fig. 4.5.2.1). The remaining two photographs (frames 7 and 8) reveals that slip did occur at the top right hand corner of the specimen. This slip is shown also by the behaviour of point C in Fig. 4.5.2.2. Except for this slight edge slip, however, a non-slip condition exists.

On Fig. 4.5.2.1 is also shown a load trace obtained for comparison with finite element predictions in chapter 5.

Test 2 was intended to examine the motion of the plasticine along the unlubricated top platen boundary. Fig. 4.5.2.3 shows the results. At t=-0.4ms the platen is just above the surface. The remaining series of photographs shows that no motion takes place along the impact boundary except for the element at the top right corner as was observed in test 1. Fig. 4.5.2.4 is a superimposed drawing of two specimen grid positions. These were obtained by projecting the images onto tracing paper as described in

Section 4.3.4 and then superimposing each of the drawings. Fig 4.5.2.4 shows the result and confirms accurately the observations made earlier regarding a full stick condition except for slip at the top right hand corner of the specimen.

For test 3 the platen surface was lubricated with light oil to give a slip boundary condition. Fig. 4.5.2.5 shows the photographs obtained and Fig. 4.5.2.6 shows the superimposed tracing obtained in the same way as Fig. 4.5.2.4. A comparison of Fig. 4.5.2.4 and 4.5.2.6 confirms that the deformation is more homogeneous in the slip case.

In test 4 the specimen was unlubricated and the platen velocity was 2m/s instead of 4.4m/s. The deformed profiles are shown in Fig. 4.5.2.7. At the start of the compression the deformed profiles were similar to those obtained at 4.4m/s. After significant straining had taken place, however, some differences were apparent. These differences will be discussed in chapter 5.

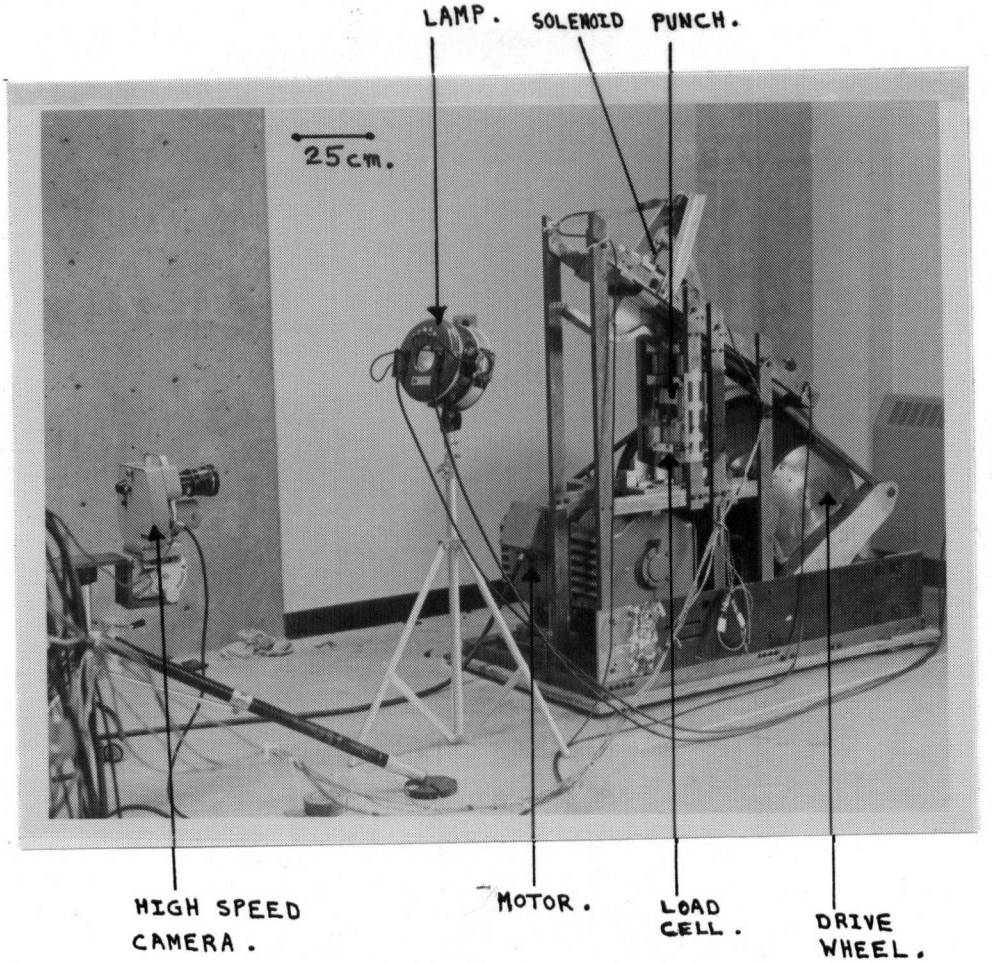

FIG. 4.2.1.(a).

PHOTOGRAPH OF THE IMPACT PRESS AND HIGH SPEED CAMERA.

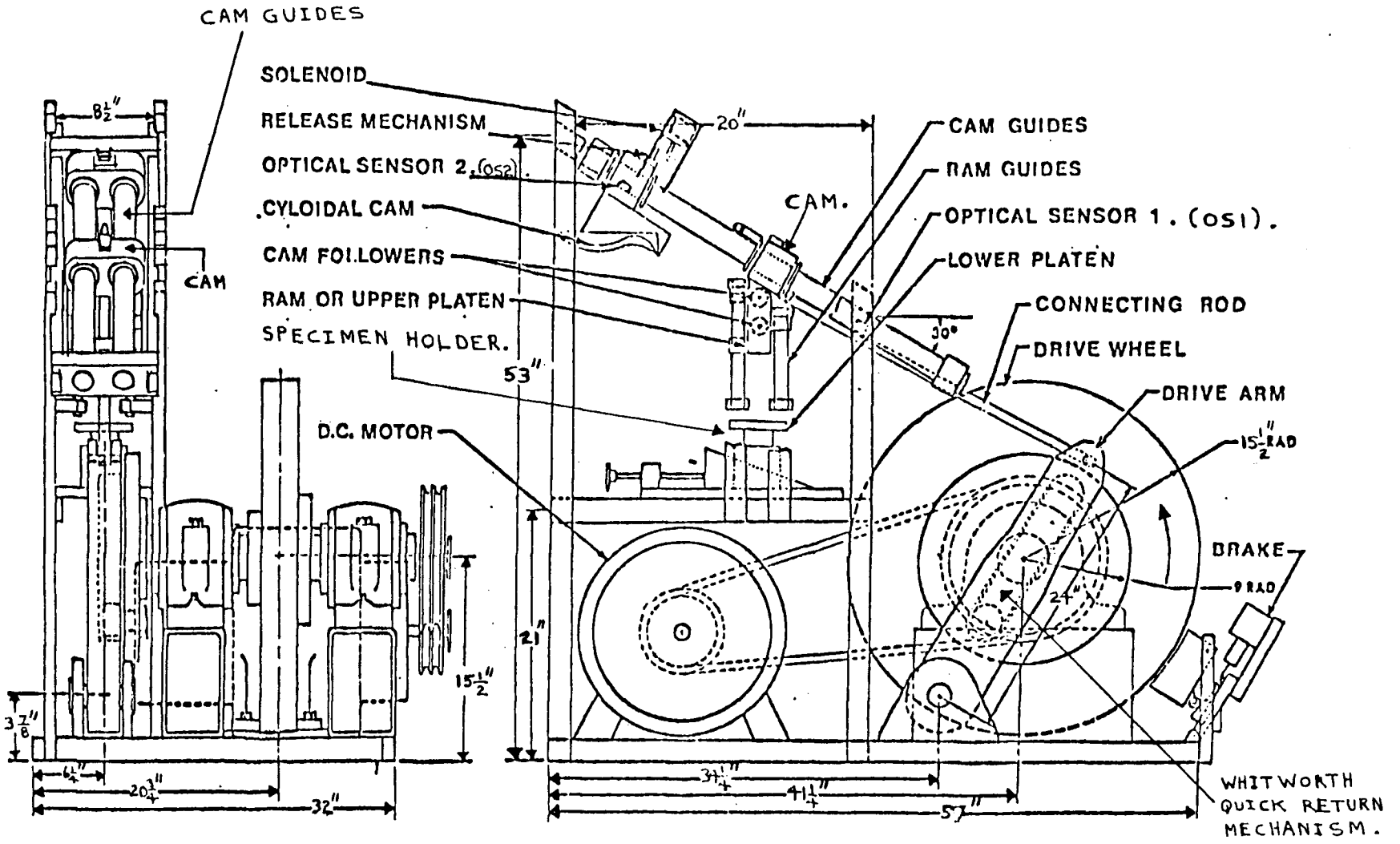

FIG. 4.2.1.(b).

THE IMPACT PRESS USED FOR THE DEFORMATION TESTS.

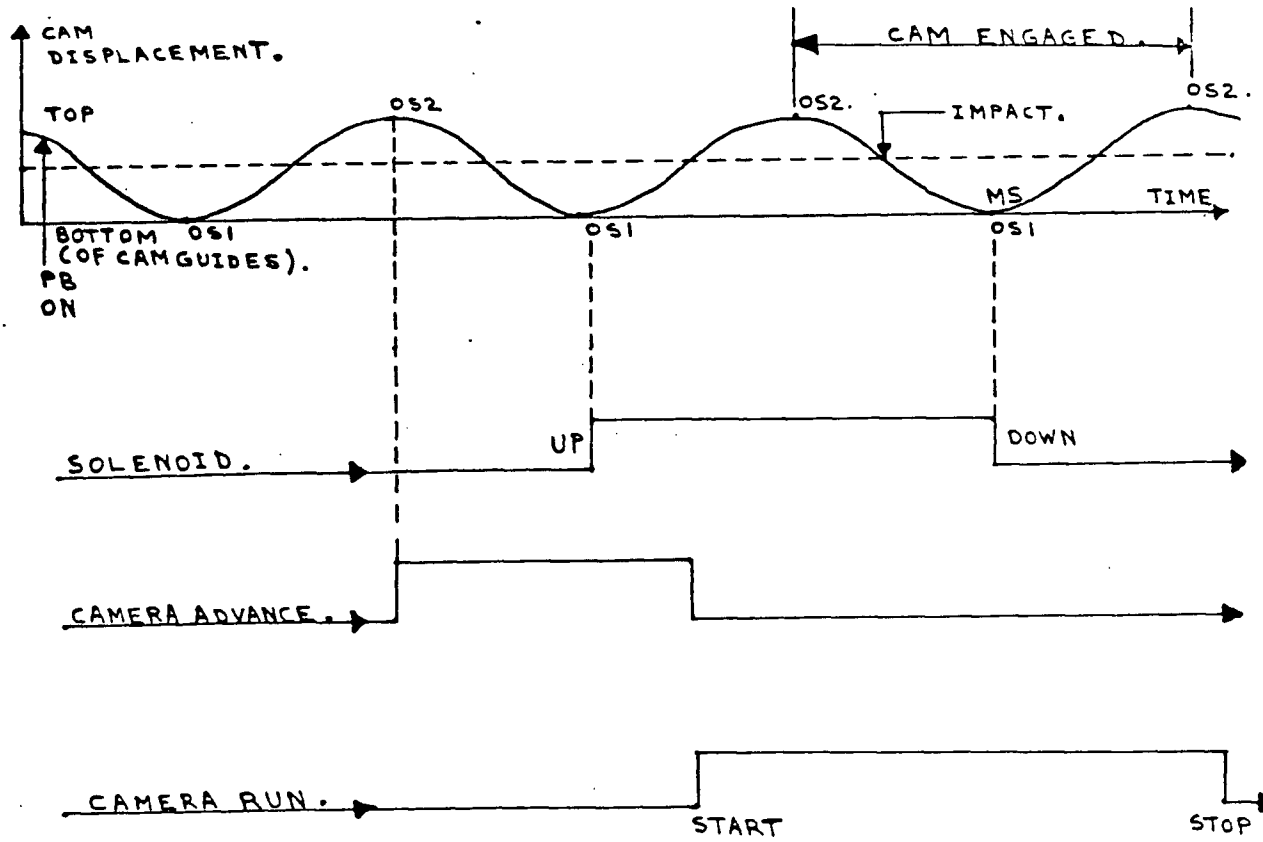

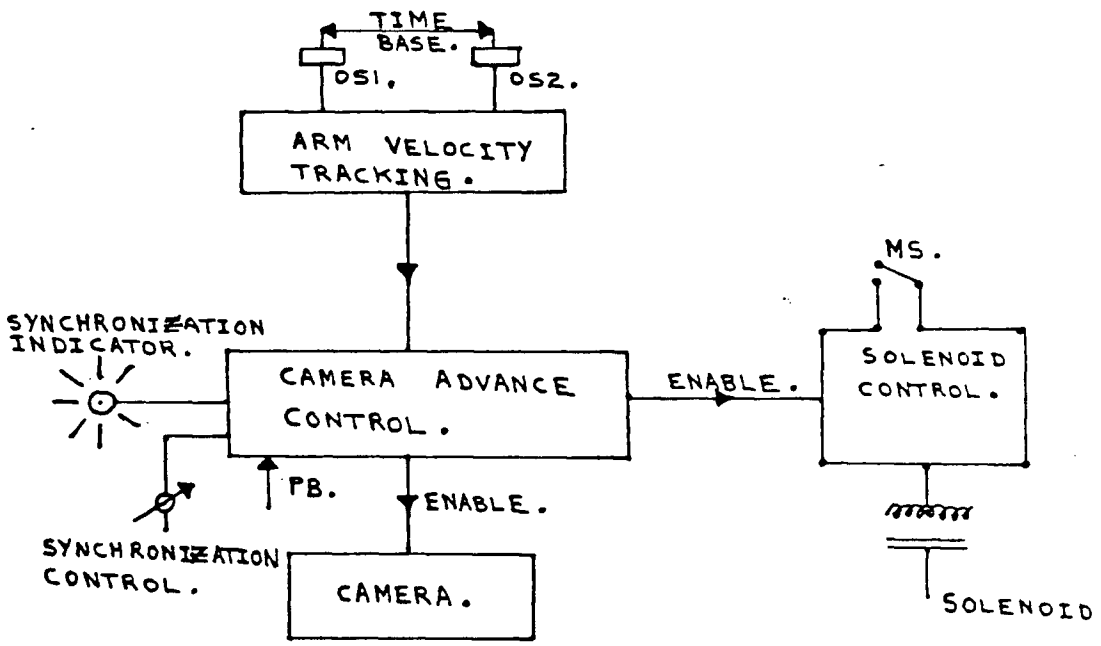

FIG. 4.2.2.

LOGIC OF THE ELECTRONIC CIRCUIT FOR CAMERA SYNCHRONIZATION.

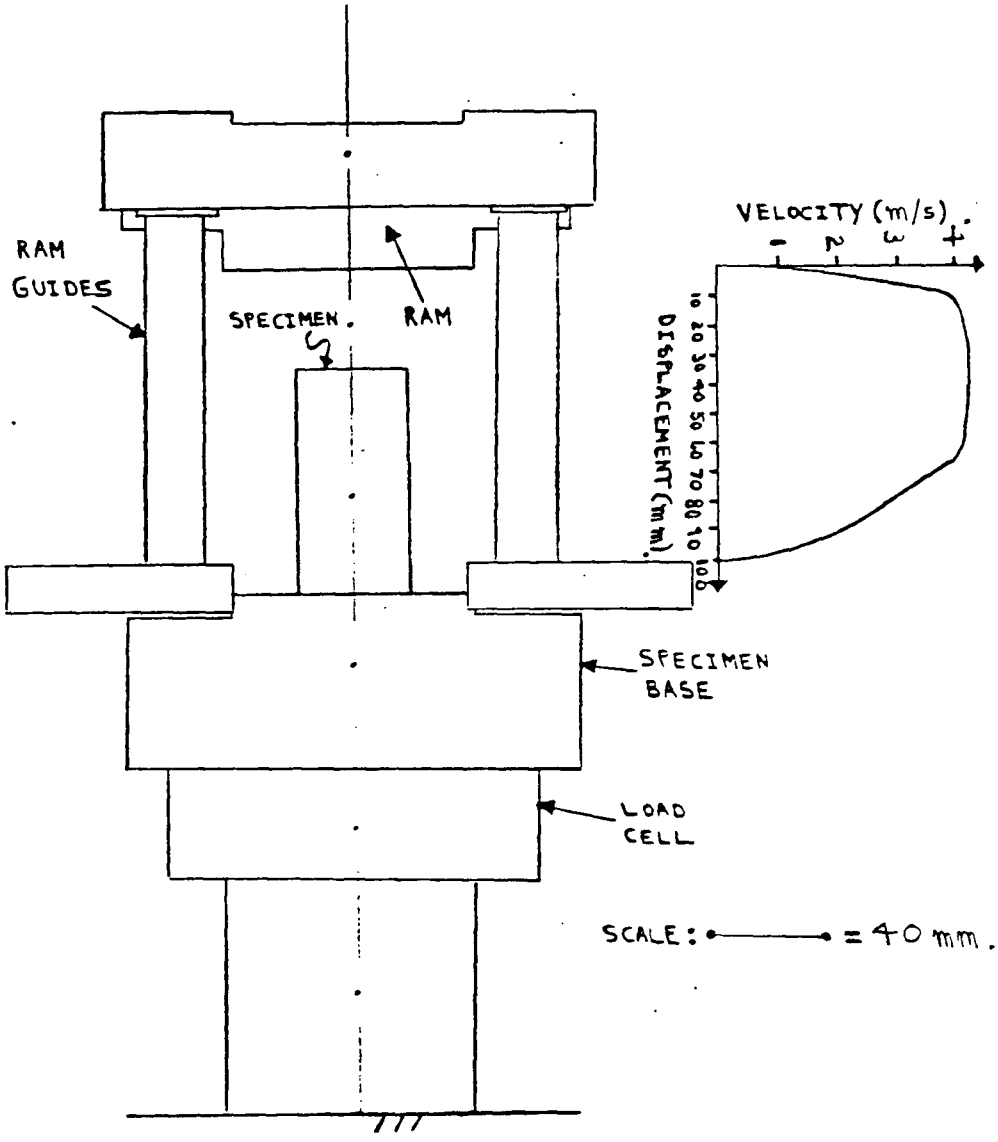

FIG. 4.2.3.

THE SPECIMEN HOLDER ON THE IMPACT PRESS. A PLATEN VELOCITY AGAINST DISPLACEMENT CURVE IS ALSO SHOWN.

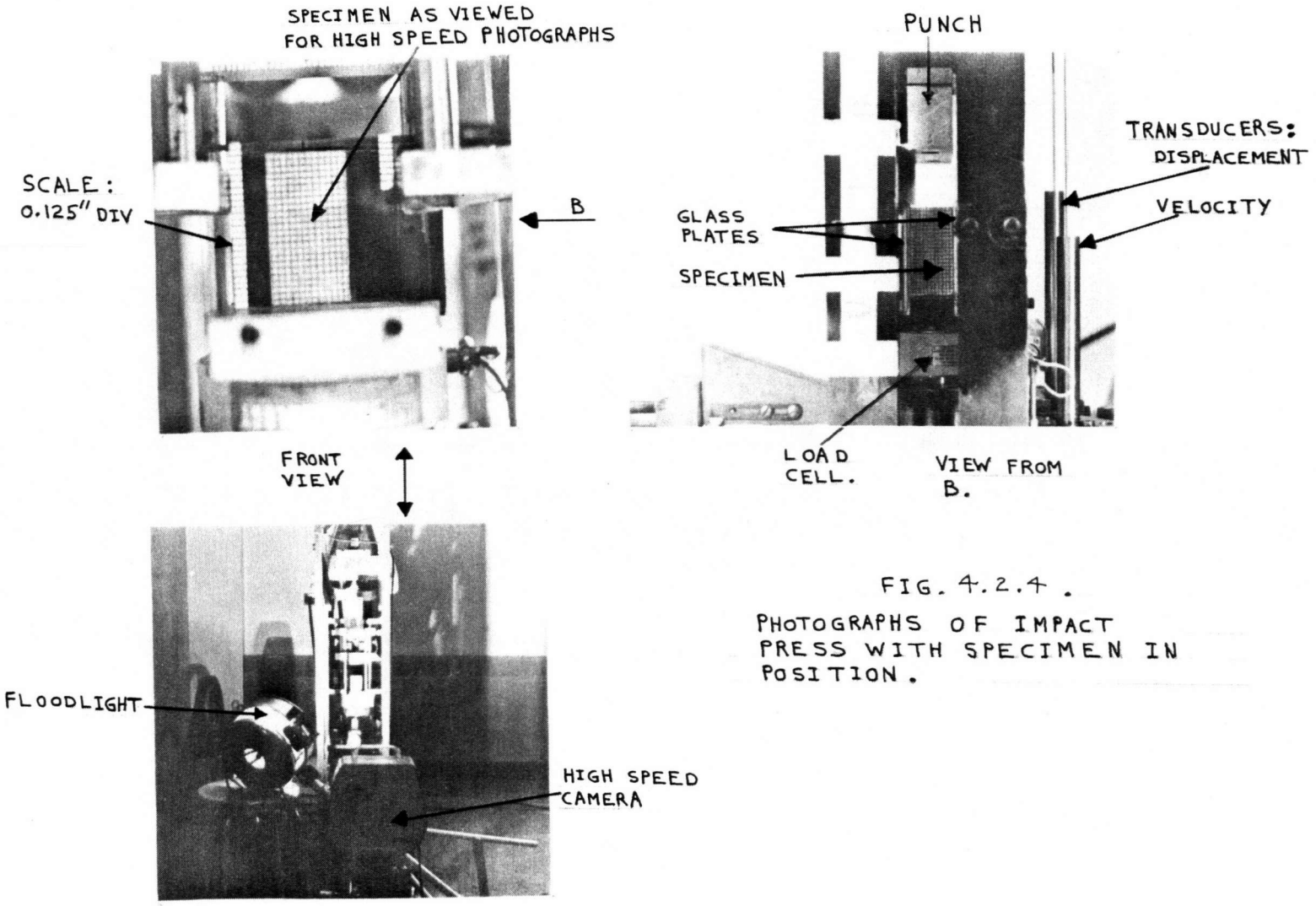

FIG. 4.2.4.

PHOTOGRAPHS OF IMPACT PRESS WITH SPECIMEN IN POSITION.

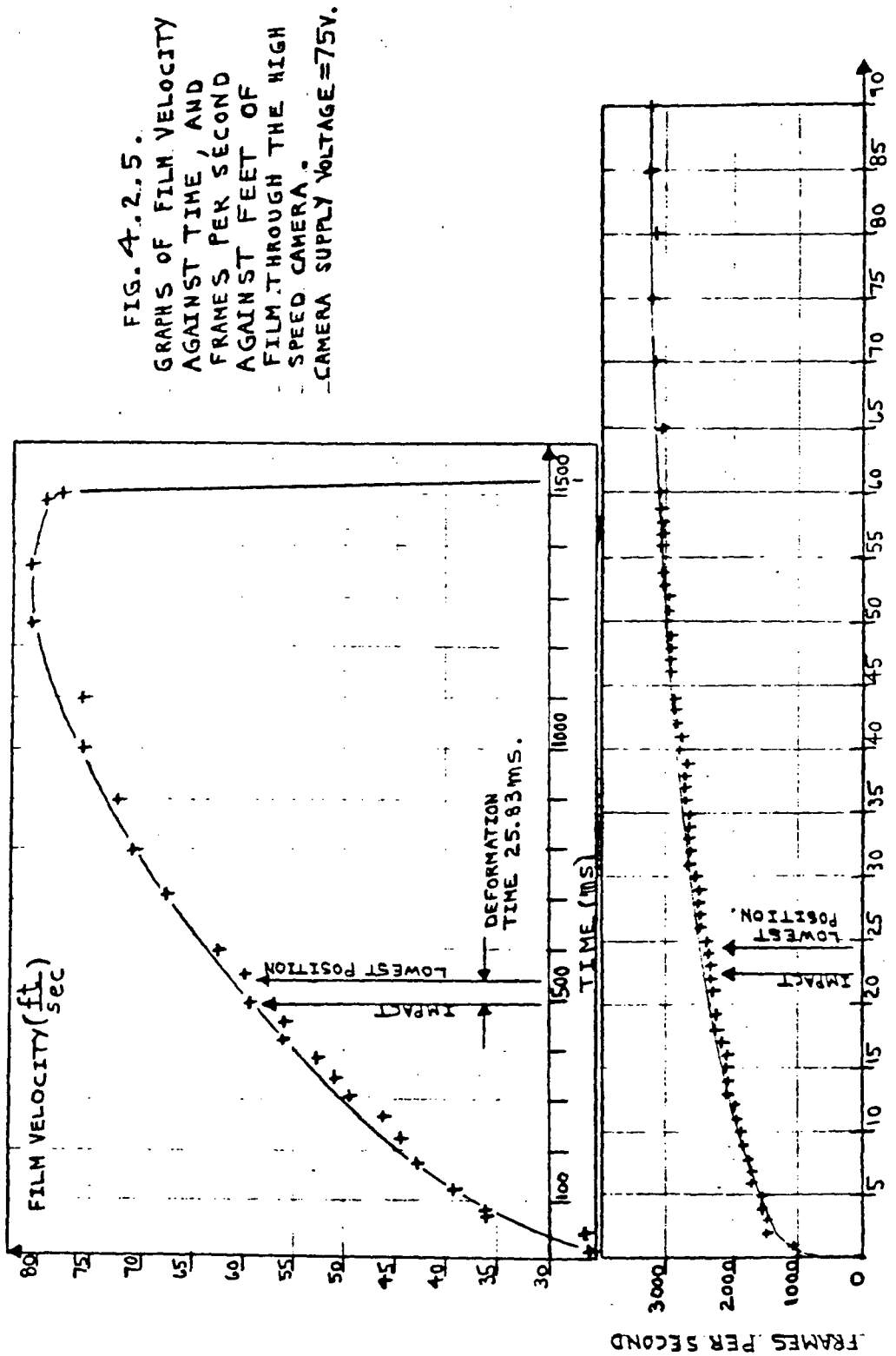

FIG. 4.2.5.
GRAPHS OF FILM VELOCITY AGAINST TIME, AND FRAMES PER SECOND AGAINST FEET OF FILM THROUGH THE HIGH SPEED CAMERA.
CAMERA SUPPLY VOLTAGE=75V.

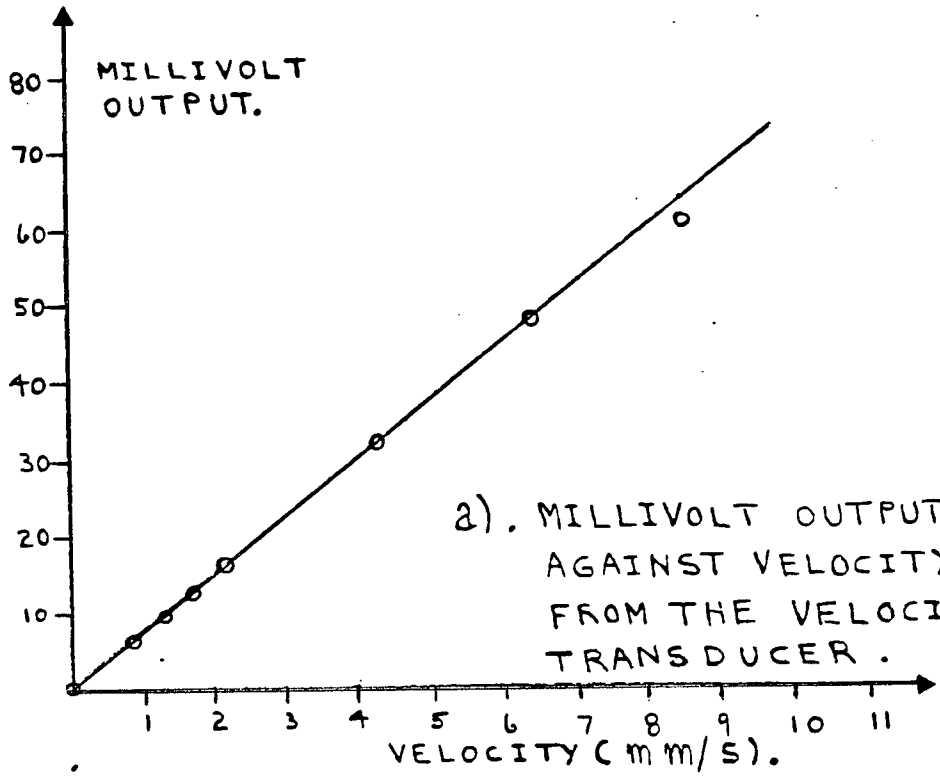

a). MILLIVOLT OUTPUT AGAINST VELOCITY FROM THE VELOCITY TRANSDUCER.

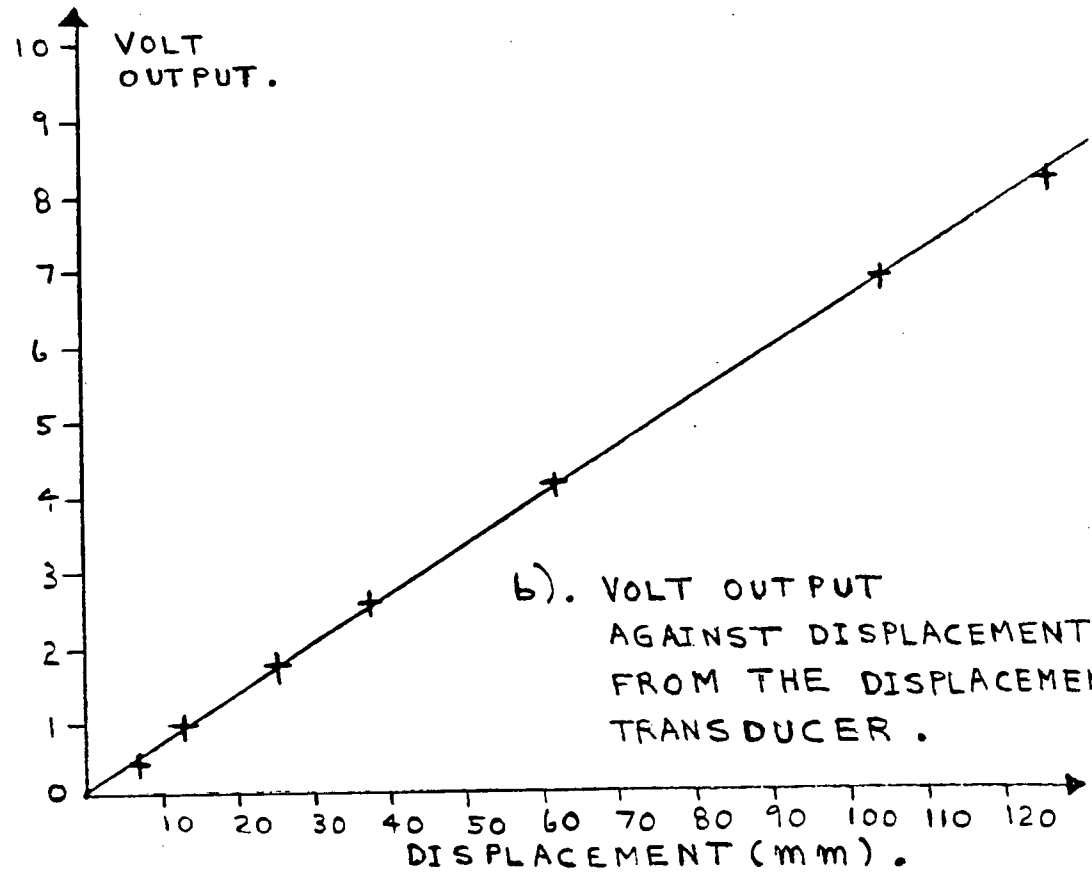

b). VOLT OUTPUT AGAINST DISPLACEMENT FROM THE DISPLACEMENT TRANSDUCER.

FIG. 4.2.6.

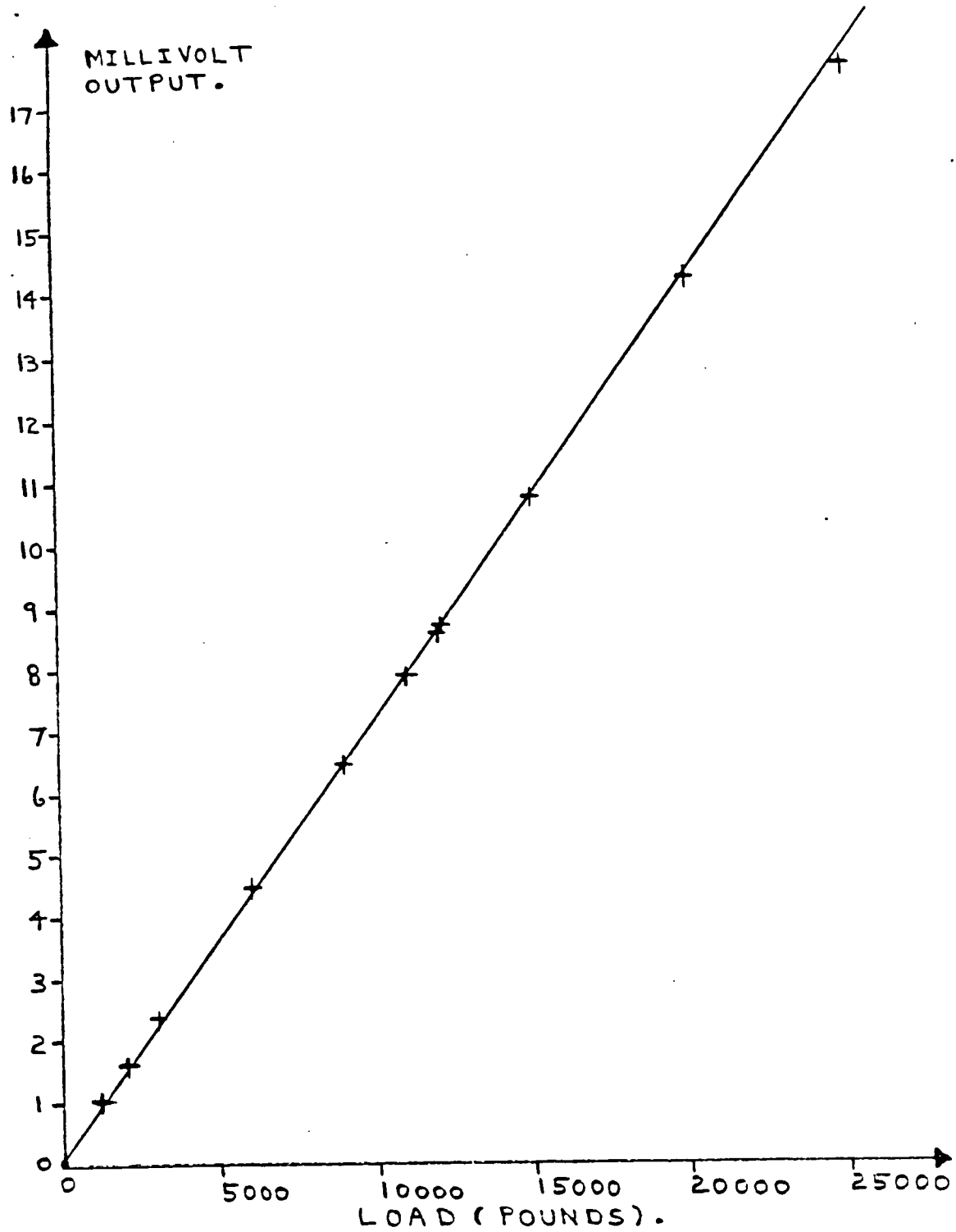

FIG. 4.2.7.
PLOT OF OUTPUT VOLTAGE FROM THE LOAD CELL AGAINST APPLIED LOAD.

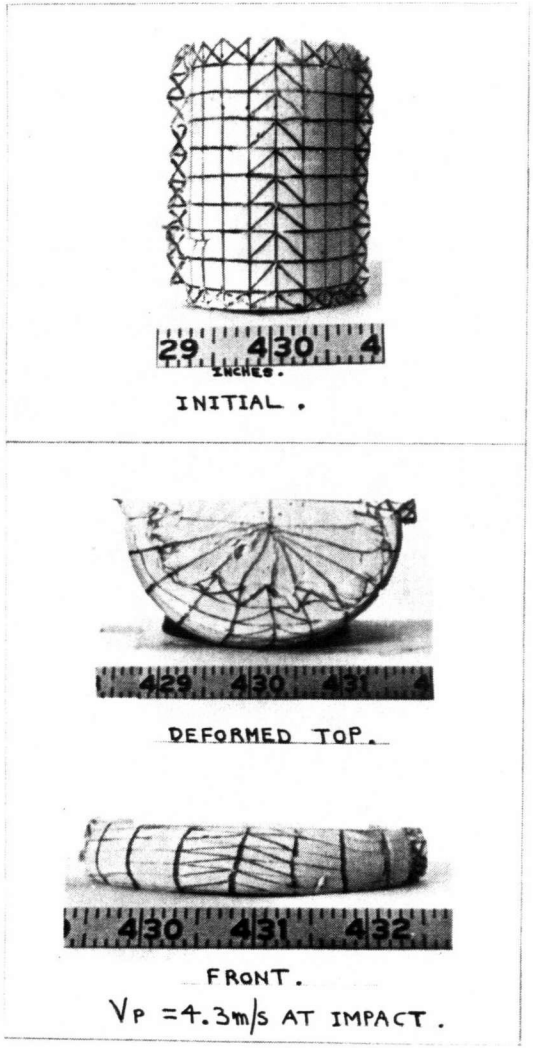

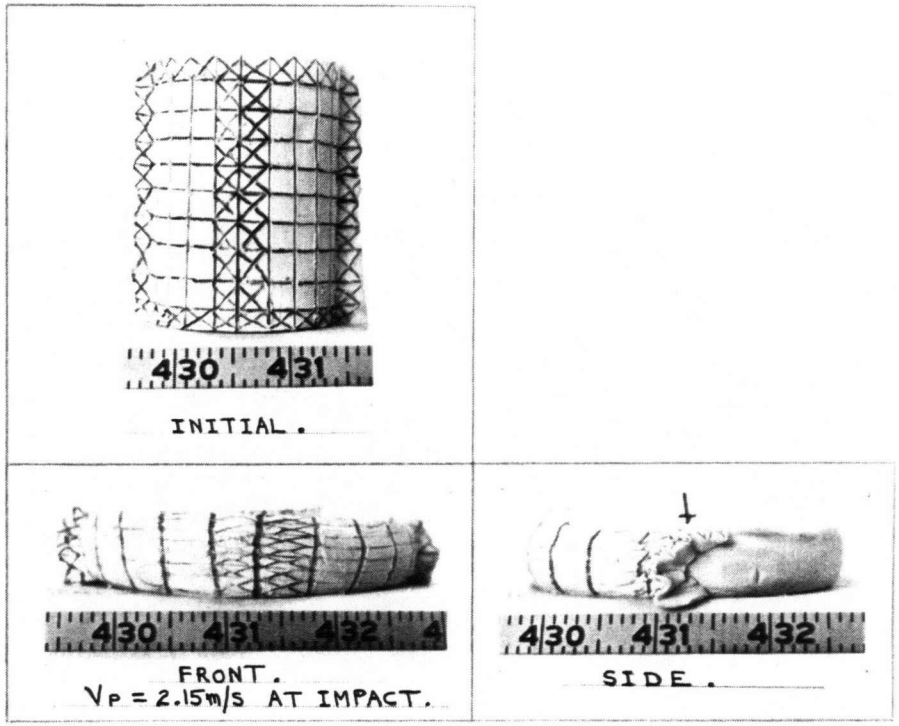

FIG. 4.4.1.

INITIAL AND FINAL DEFORMED SHAPES OF TWO AXISYMMETRIC PLASTICINE SPECIMENS FROM TESTS FOR DETERMINING MATERIAL PROPERTIES .

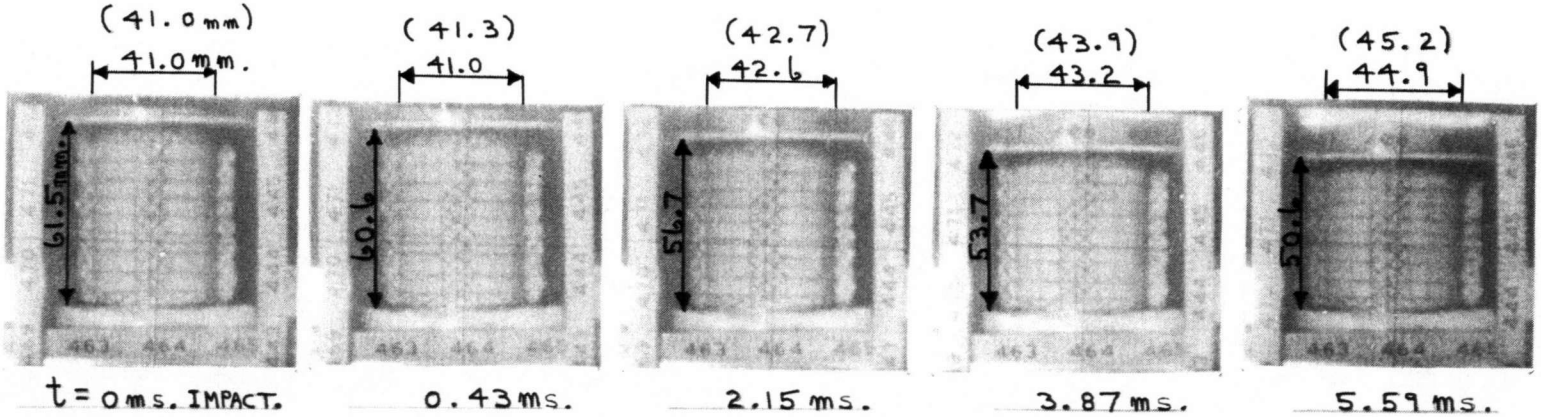

( ) = CALCULATED DIAMETERS.

FIG. 4.4.2.
DYNAMIC COMPRESSION OF A CYLINDRICAL PLASTICINE SPECIMEN.

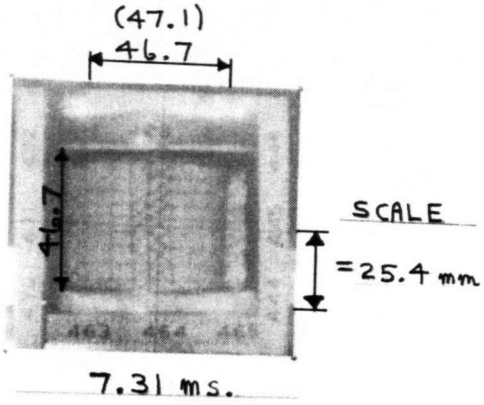

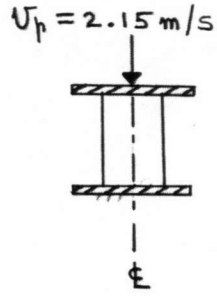

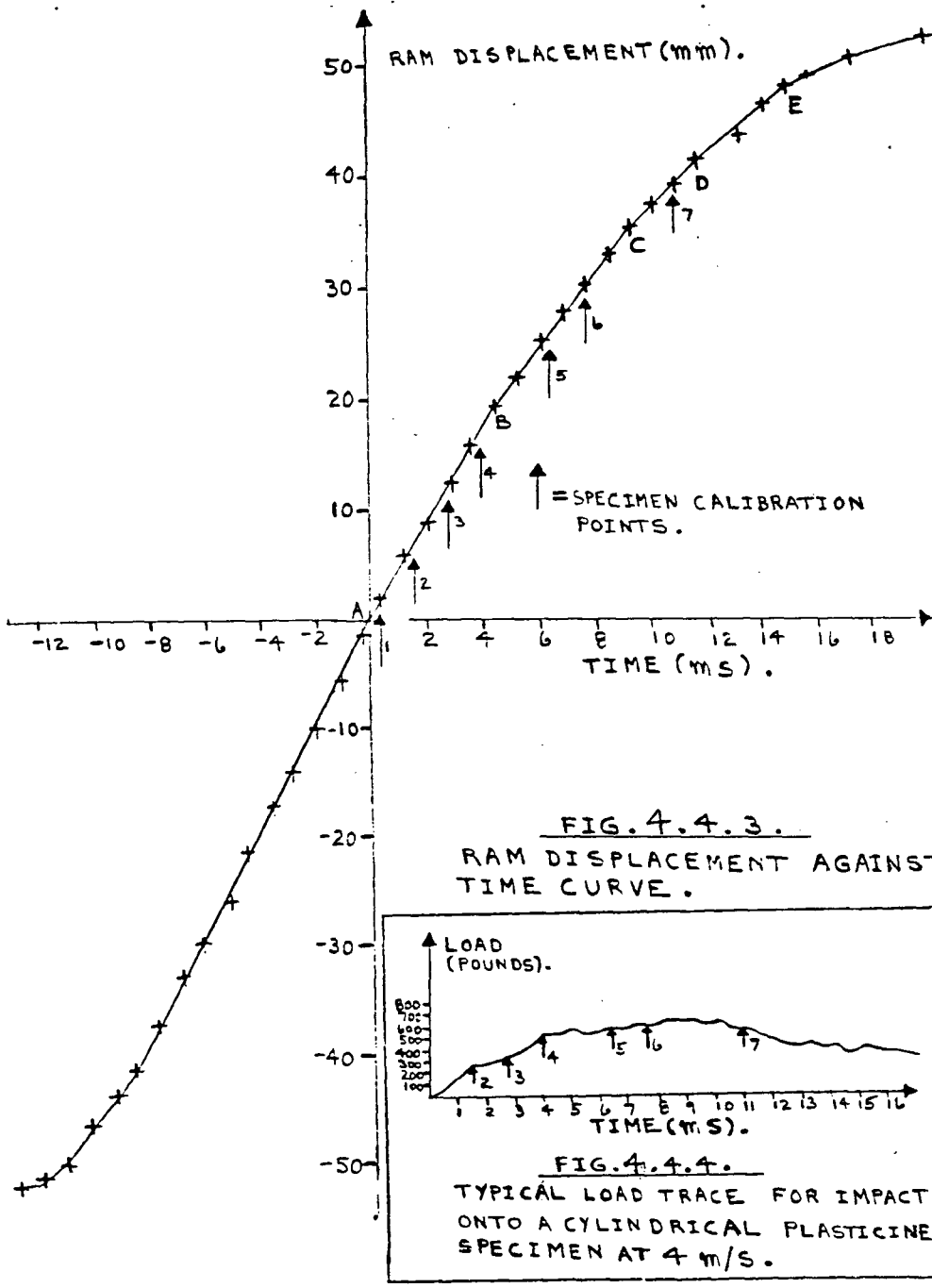

FIG. 4.4.3.

RAM DISPLACEMENT AGAINST TIME CURVE.

FIG. 4.4.4.

TYPICAL LOAD TRACE FOR IMPACT ONTO A CYLINDRICAL PLASTICINE SPECIMEN AT 4 m/s.

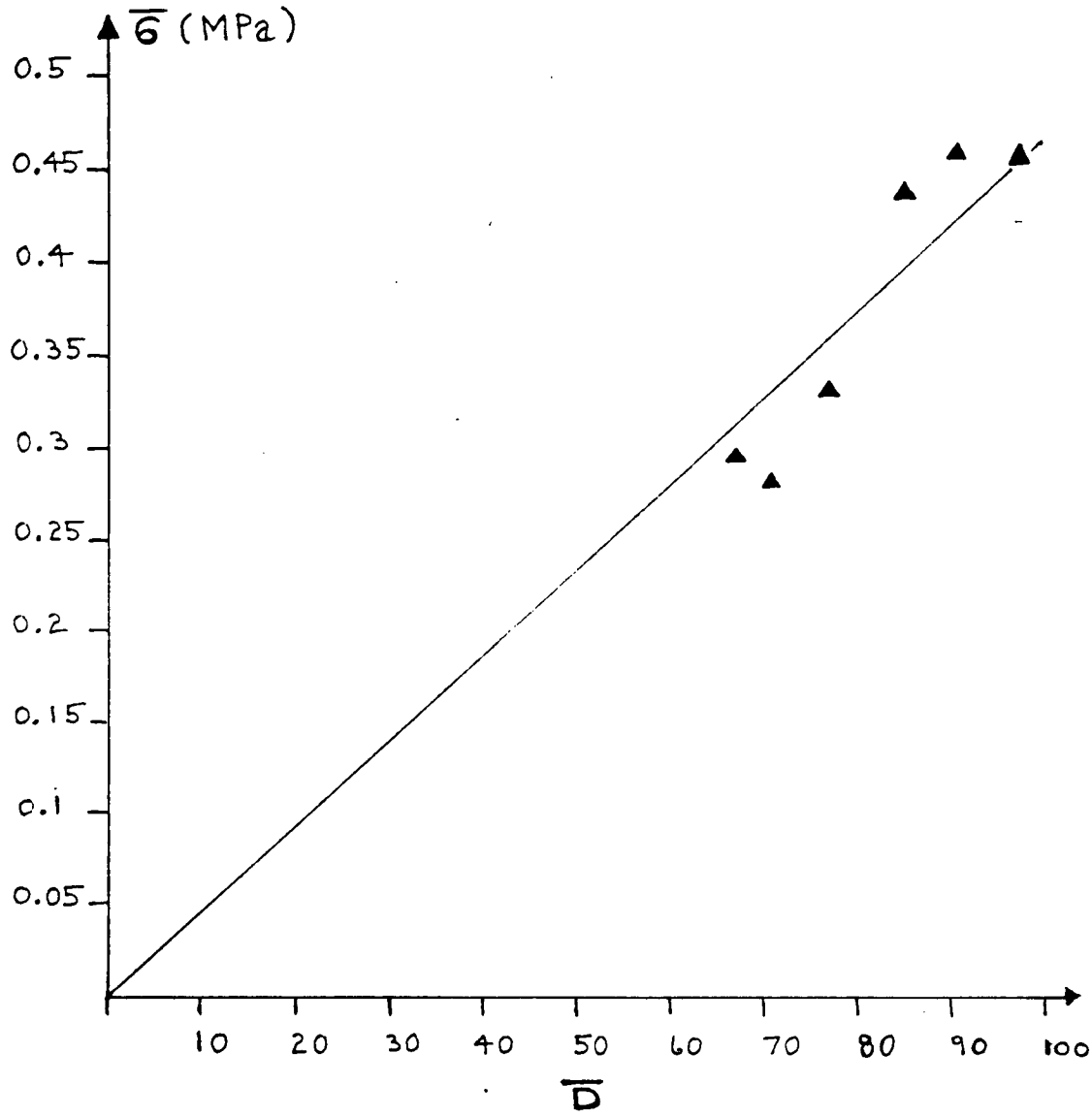

FIG. 4.4.5.

CALIBRATION CURVE OF $\overline{\sigma}$ AGAINST $\overline{D}$ FOR PLASTICINE.

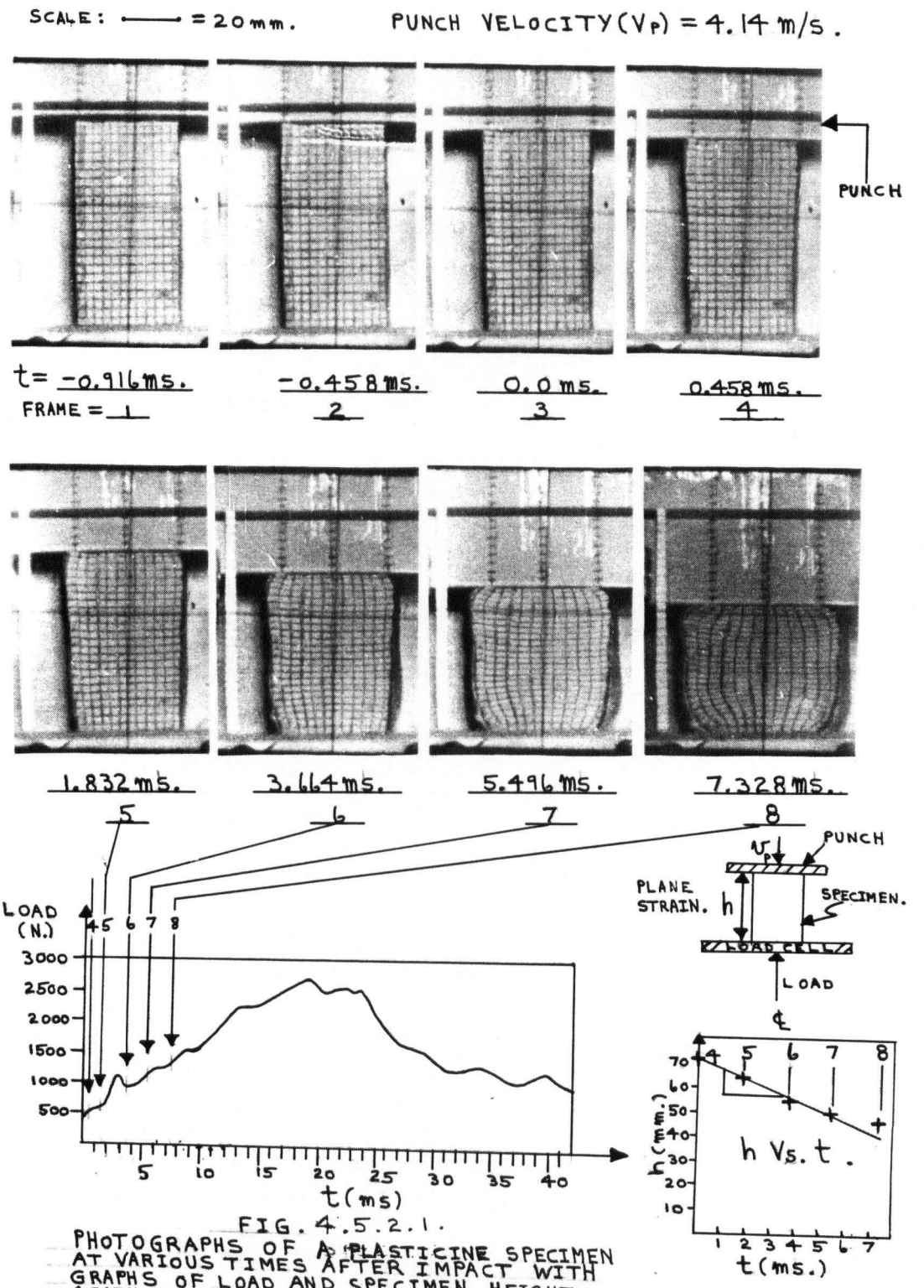

FIG. 4.5.2.1.
PHOTOGRAPHS OF A PLASTICINE SPECIMEN AT VARIOUS TIMES AFTER IMPACT WITH GRAPHS OF LOAD AND SPECIMEN HEIGHT AGAINST TIME. V_P APPROXIMATELY 4 m/s DURING DEFORMATION.

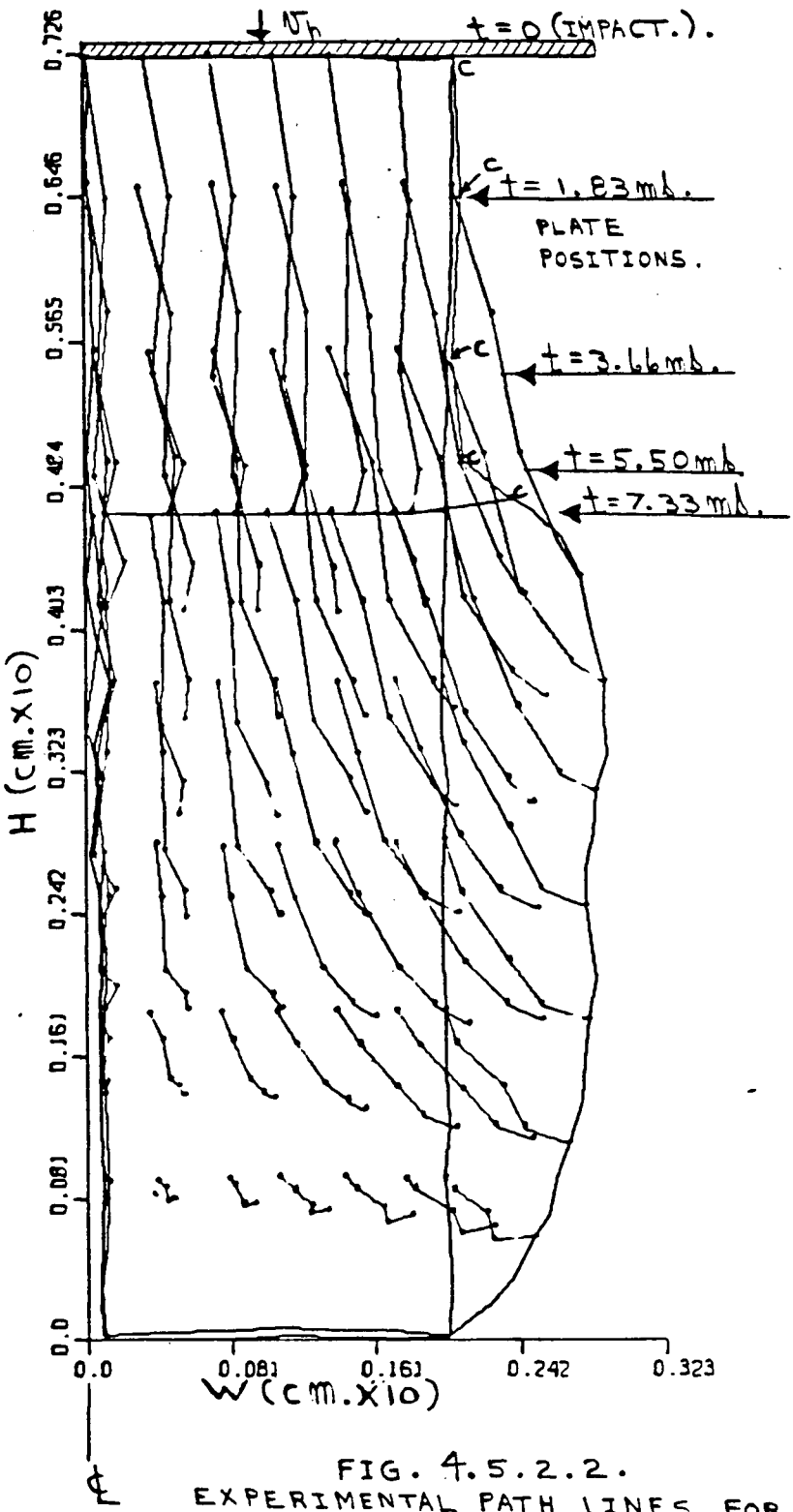

FIG. 4.5.2.2.
EXPERIMENTAL PATH LINES FOR A TYPICAL PLASTICINE SPECIMEN BEING COMPRESSED IN PLANE STRAIN.

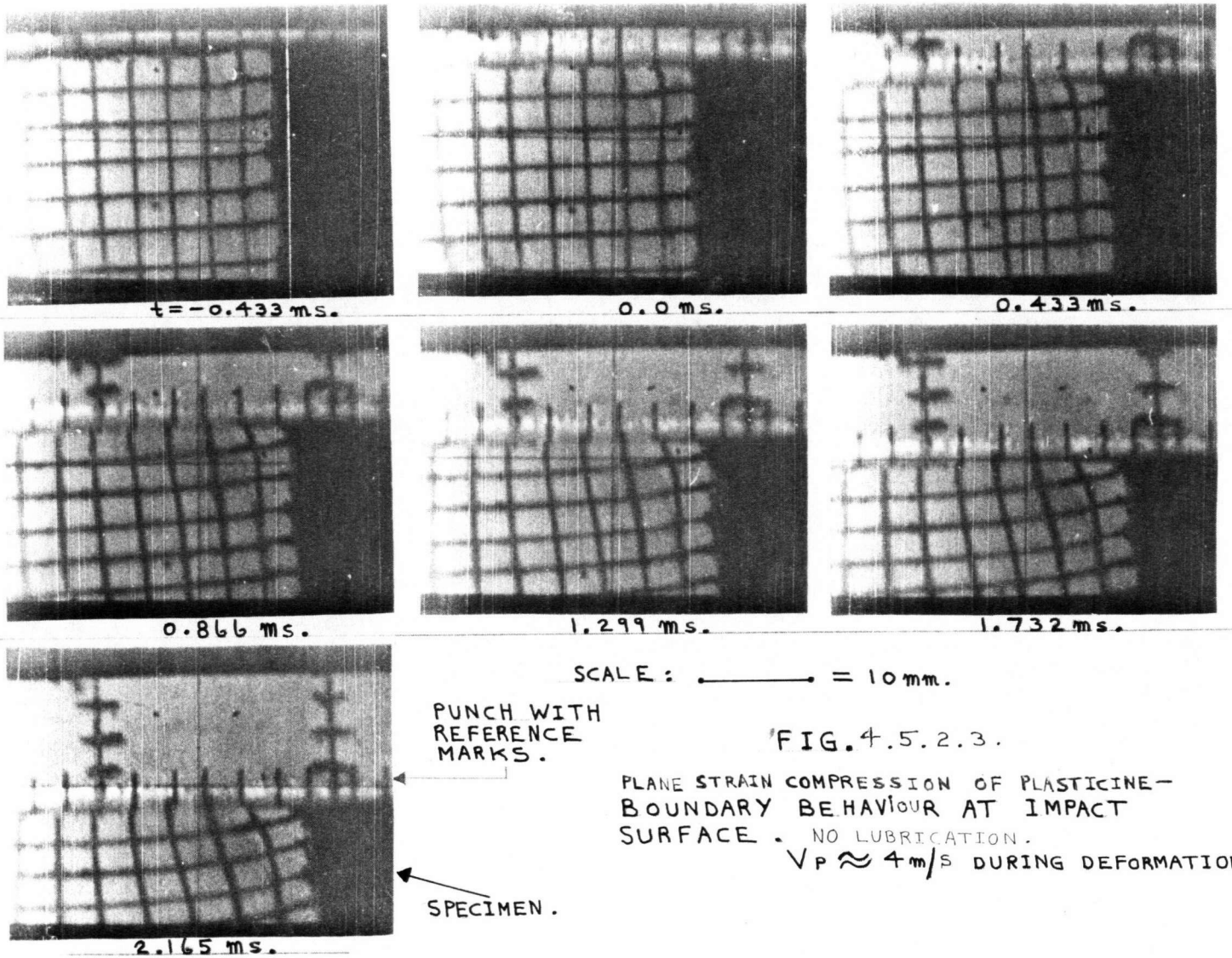

FIG. 4.5.2.3.

PLANE STRAIN COMPRESSION OF PLASTICINE— BOUNDARY BEHAVIOUR AT IMPACT SURFACE. NO LUBRICATION. $V_P \approx 4$ m/s DURING DEFORMATION.

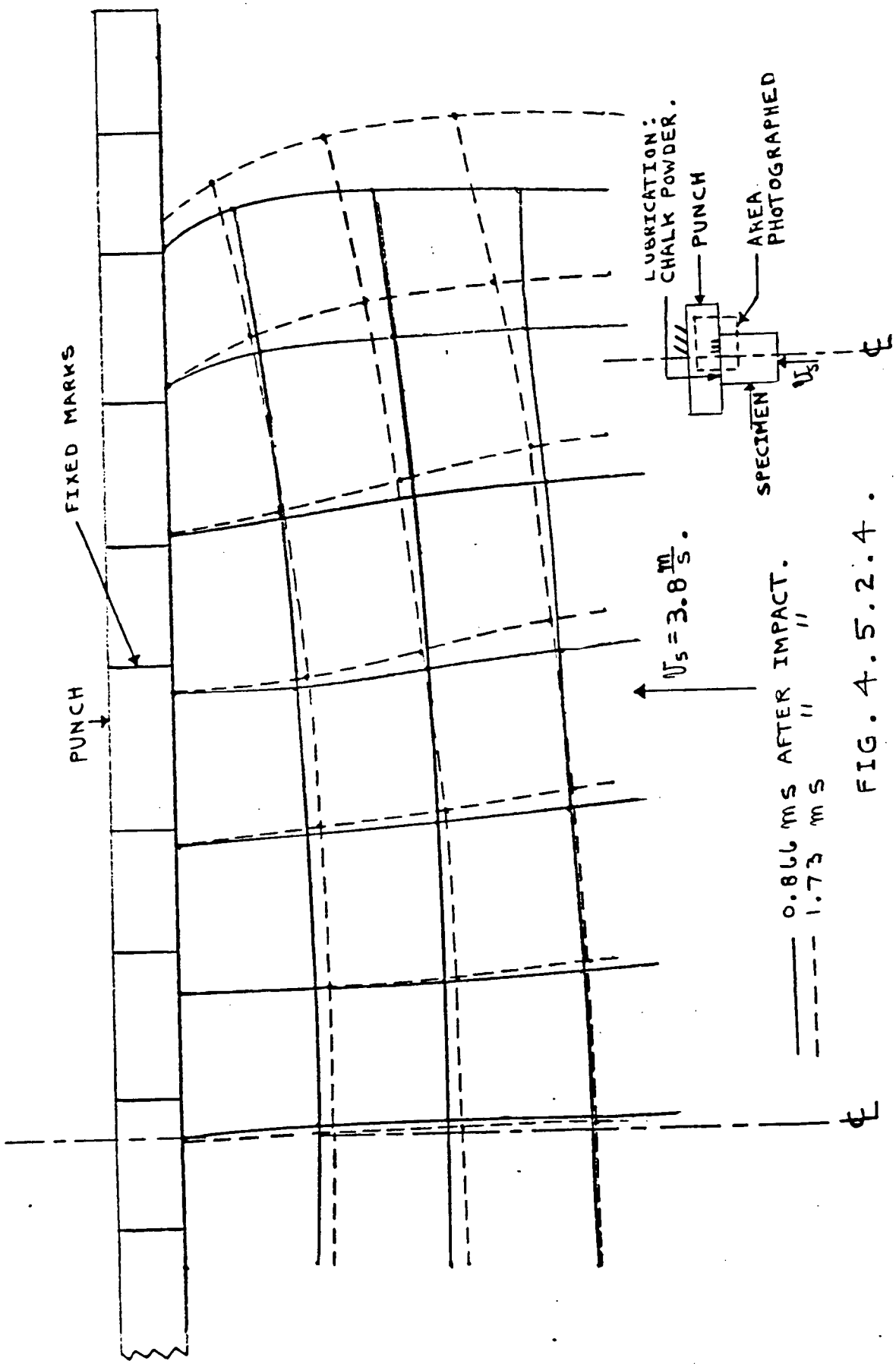

FIG. 4.5.2.4.

A SUPERIMPOSED TRACING FROM TWO PHOTOGRAPHS IN FIG. 3.5.2.3.

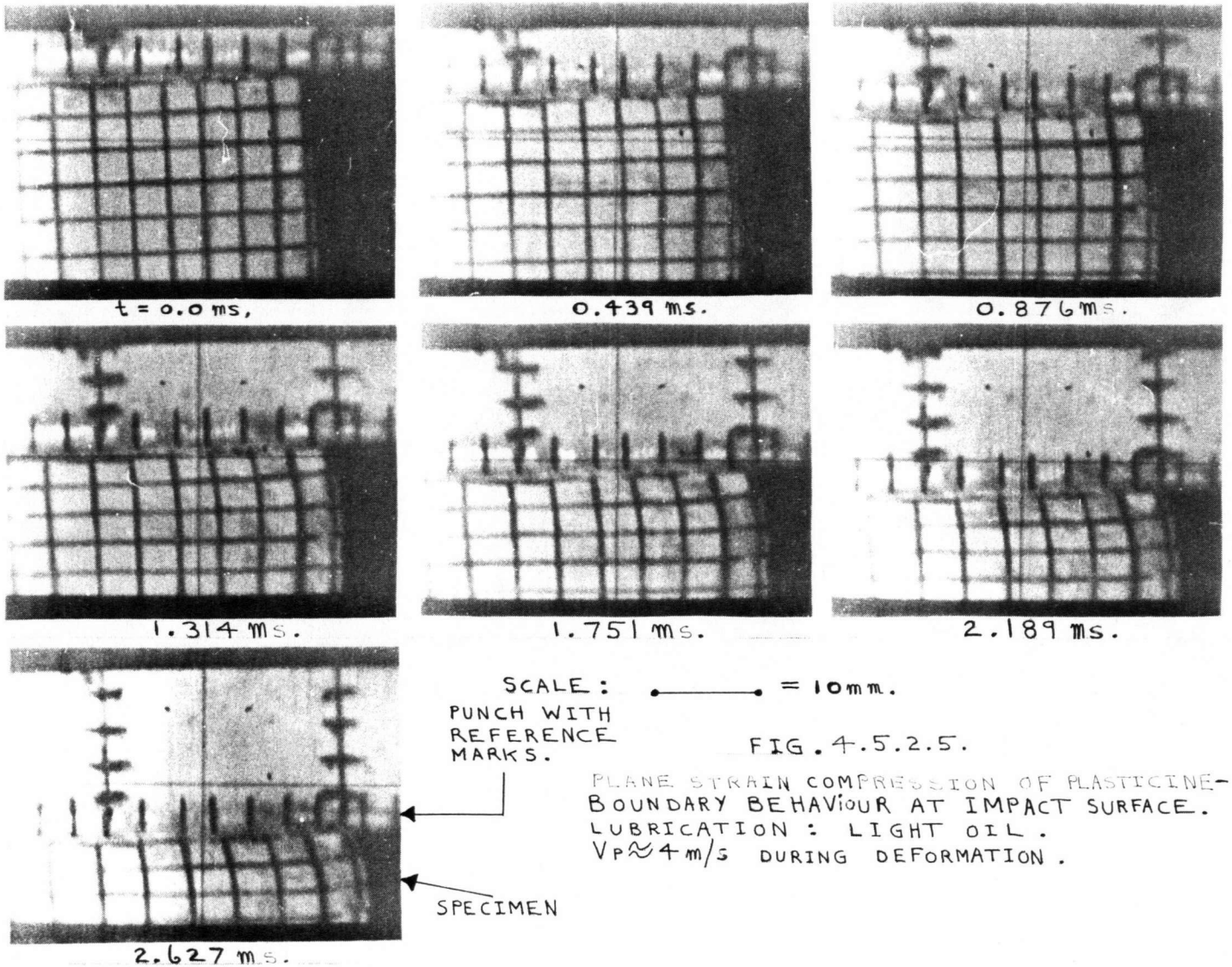

FIG. 4.5.2.5.

PLANE STRAIN COMPRESSION OF PLASTICINE- BOUNDARY BEHAVIOUR AT IMPACT SURFACE.
LUBRICATION : LIGHT OIL.
$V_P \approx 4$ m/s DURING DEFORMATION.

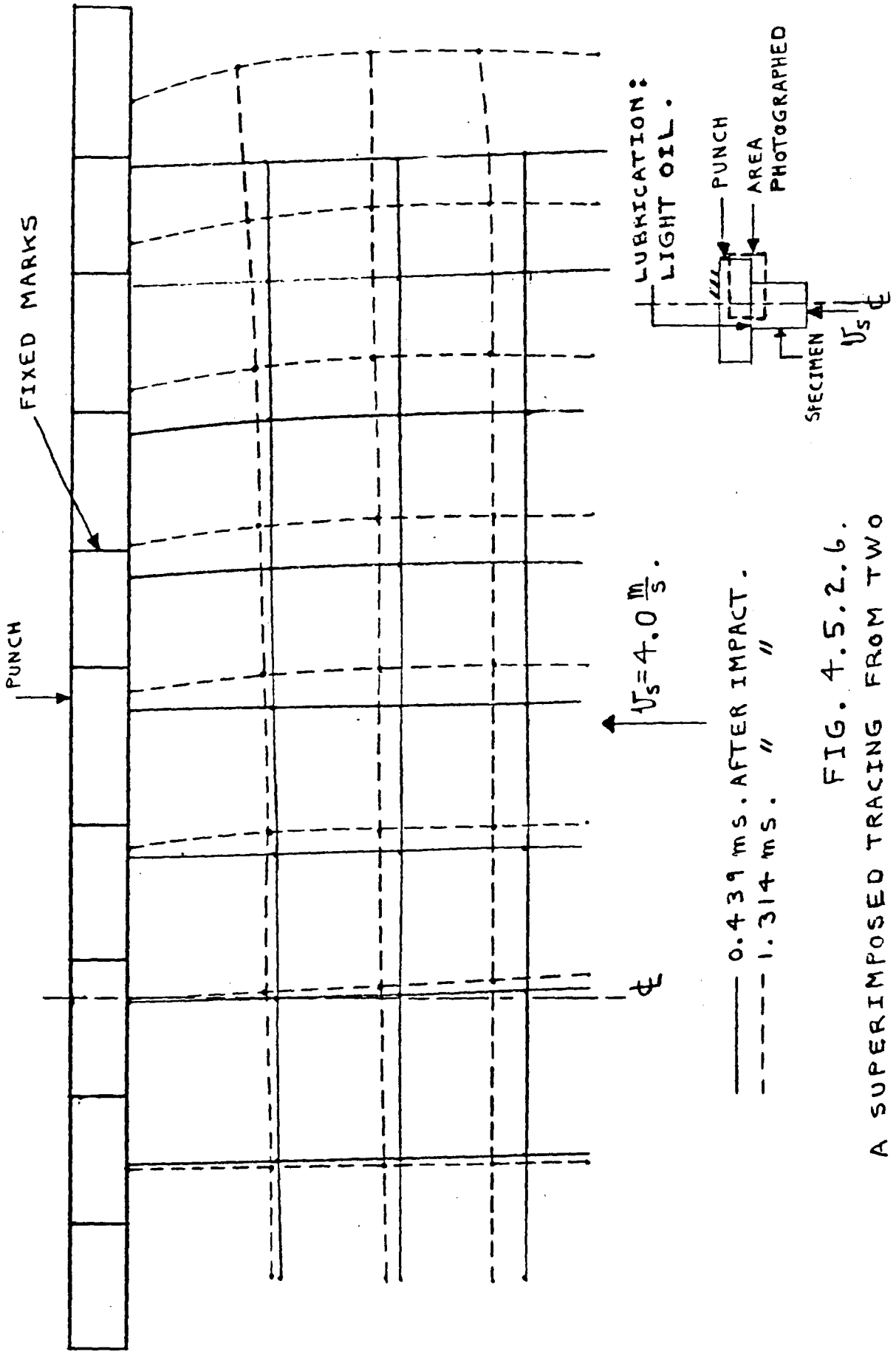

FIG. 4.5.2.6.
A SUPERIMPOSED TRACING FROM TWO PHOTOGRAPHS IN FIG. 3.5.2.5.

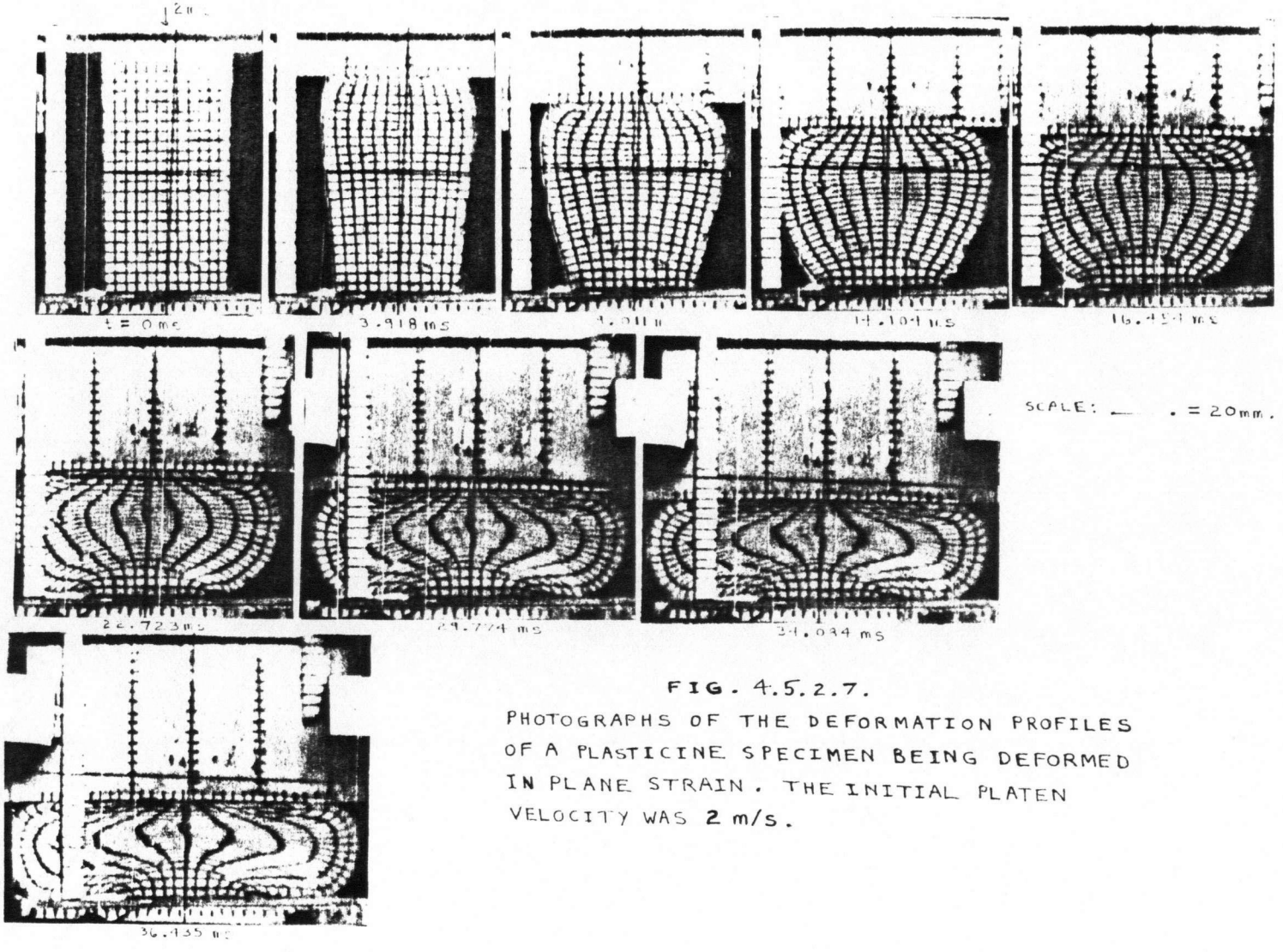

FIG. 4.5.2.7.

PHOTOGRAPHS OF THE DEFORMATION PROFILES OF A PLASTICINE SPECIMEN BEING DEFORMED IN PLANE STRAIN. THE INITIAL PLATEN VELOCITY WAS 2 m/s.

CHAPTER 5

FINITE ELEMENT MODELLING OF PLANE STRAIN COMPRESSION.

In this chapter the results of numerical modelling of plane strain compression are presented. For the purposes of code verification, the computer code predictions were first compared with experimental results. Once it had been established that the model was satisfactory, a systematic series of modelling tests were done. The main purpose of the tests was to investigate the effects of material properties, inertia, friction boundary conditions, and specimen dimensions on the stress and deformation patterns in the material being compressed in plane strain. The results are then used to make fundamental conclusions about the effect of the variables in general die-forging operations.

The following sections are presented in this chapter. Section 5.1 presents the results of some initial tests with the code for the purpose of determining suitable finite element parameters. Section 5.2 presents the results of experimental tests on plasticine and compares them to the finite element results. In addition, a comparison is made with experimental tests on aluminum. Section 5.3 considers some rigid-perfectly plastic results and Section 5.4 some strain rate sensitive and strain hardening results. Section 5.5 considers the dynamic compression of aluminum at 100m/s. Finally, Section 5.6 considers the stress distributions for both the rigid-perfectly plastic quasi-static cases and the dynamic compression of aluminum.

5.1 DETERMINATION OF THE FINITE ELEMENT PARAMETERS.

5.1.1. Homogeneous Compression.

The program was tested for the case of homogeneous plane strain deformation as discussed in chapter 2. In this case the solution is linear and the finite elements are able to represent the solution exactly. Fig. 5.1.1.1 shows a velocity vector plot for this case.

5.1.2. Number Of Elements.

The effect of element size was considered by test calculations in all applications in this work.

Fig. 5.1.2.1 compares the deformation of a 15 and 50 element idealization of an aluminum block at 44% vertical strain. The 15 element case lacks detail but both approximations are quite consistent. The comparison shows that significant detail would be lost if the 15 element case were used intead of the 50. For this case 50 elements was taken as an acceptable amount. However it was found that 144 elements were required to give a satisfactory comparison with our experimental tests on plasticine.

5.1.3. Determination Of Allowable Strain Increment.

During initial program testing a preliminary assessment was made of the maximimum allowable strain increment. A 15 element idealization of a block of aluminum was modelled with a linear distribution of horizontal velocity and a constant vertical velocity on the top boundary. The block was deformed to 83% of its initial height in 1, 2, 4, 8, and 12 incremental steps. In each case the shear stress on the top boundary was plotted after

the required number of incremental steps had been taken to reach the final height. This shear stress is plotted in Fig. 5.1.3.1. It was found that the shear stress did not change significantly between 8 and 12 increments. Thus a 2% incremental strain step gave reasonable accuracy.

5.1.4. Constitutive Relations.

The assumed relation of yield stress to strain hardening and strain rate sensitivity selected for the finite element program is given in equation 3.5.3. In this work the two real materials that are considered are aluminum and plasticine. In the constitutive relations used aluminum is considered strain hardening but not strain rate sensitive. Plasticine is considered to be strain rate sensitive but not strain hardening.

The constitutive relation for the strain hardening case is found from equation 3.5.3 by setting $c_2=0$ to indicate no strain rate sensitivity. This then gives

$$Y=(1+c_1\bar{e})^{\gamma}Y_o \qquad (5.1.4.1)$$

where $\bar{e}$ is given from equation 3.2.5.

Fig. 5.1.4.1 shows curves of $\bar{\sigma}$ against $\bar{e}$ for aluminum obtained from various sources. The one used is indicated and corresponds to the constants $c_1=16.436$, $\gamma=0.25$ with $Y_o=106.18$MPa, the static yield stress for annealed aluminum.

Based upon experimental calibration tests for plasticine in chapter 3 the relation given below was assumed.

$$\bar{\sigma}=4650\bar{D} \qquad (5.1.4.2)$$

Here $\bar{\sigma}$ is in Pa and $\bar{D}$ is in s^{-1}. This relation was used by the finite element code for the modelling of plasticine and

is plotted in Fig. 4.4.5.

5.2 EXPERIMENTAL COMPARISONS.

The purpose of the comparison of the finite element code predictions with experiment was to verify that the numerical model proposed was satisfactory. Once a satisfactory comparison with experiment had been obtained, modelling results without experimental comparison could be accepted with confidence.

5.2.1. Comparison Of The Finite Element Model With Experimental Tests On Plasticine.

The experimental testing technique for plasticine was outlined in Chapter 4. Figs. 5.2.1.1 and 5.2.1.2 show the profile of experimentally deformed plasticine specimens for a compression speed of 2m/s and 4.4 m/s respectively. The experimental results for these two speeds show somewhat different patterns. At 4.4m/s there is less bulging at the top than for 2m/s.

Finite element calculations were done for the case of compression at a speed of 4.4m/s with a coefficient of friction for glass, η_g, of 0, 0.1, and 0.235. The coefficient of friction for the platens was taken as 0.249 for all cases based upon tabulated values. The finite element model will give similar results at 2m/s and 4.4m/s as the dynamic effect is shown not to be a factor at this compression speed and the friction law is velocity independent. Figs. 5.2.1.3(a) and (b), Figs. 5.2.1.4(a) and (b), and Figs 5.2.1.5(a) and (b) show the results for each of the cases respectively. Fig. 5.2.1.6 shows a comparison of the final deformed shapes for plasticine at 2m/s and

4.4m/s with the finite element results for 4.4m/s. Based upon these figures the following conclusions can be drawn.

A). The finite element results with η_g=0.235 predict a deformation pattern that is a good approximation to the experimental result for a compression speed of 2m/s.

B). The finite element results with η_g =0.1 are a good approximation to the experimental results for a compression speed of 4.4m/s.

C). The final deformed shapes, which involve very large plastic deformation, agree remarkably well with the experimental results.

D). Glass friction is an important parameter to include in the analysis if the correct deformation profiles are to be obtained. This conclusion was also reached on the basis of the total load measured during the experimental tests.

E). A velocity independent friction law may not be appropriate for the glass friction on the plasticine specimens.

F). Since, with zero glass friction, the finite element results predicted a symmetric pattern about EF in Fig. 5.2.1.3(a), the effects of inertia on deformed shape are negligible at a platen speed of 4.4m/s.

Figs. 5.2.1.7(a) and (b) summarise theoretical and

experimental load comparisons. The experimental and theoretical loads agree well. In this case the total load on the bottom platen is the sum of the glass friction and plasticine compression loads since this is the total load that the load cell would measure.

Fig. 5.2.1.7(b) shows a comparison of load on the top and bottom platens. In this case the load on the bottom platen does not include the load transmitted to the glass plates by glass friction. Initially inertia makes the loads lower on the bottom platen than on the top. However, they converge together after about 10 ms from impact. Also plotted on this figure is the load curve based upon the simple model presented in section 2.1 with glass friction but not inertia included.

After about 80 ms inertia effects start to become important again. The curves predict that the loads will again become significantly different on the top and bottom platens. The oscillations that occur in the curves after about 70ms are due to folding of material onto the platens. In reality this folding process is a continuous one but in the finite element model the boundaries of the element being used must remain straight. Folding thus occurs in discrete patches which approximate a continuous movement of material onto the boundaries.

Figs. 5.2.1.8(a) and 5.2.1.8(b) show power distributions against time. The latter graph is plotted as a log scale but otherwise the results plotted are identical. Fig. 5.2.1.8(a) shows that the important power losses are platen load, internal deformation power and

glass friction. Kinetic energy, platen friction, and surface traction due to atmospheric pressure have negligibly small power associated with them.

Fig. 5.2.1.8(b) shows more detail regarding small power losses. The rate of change of kinetic energy of the material is initially high, drops to a minimum at about 10 ms and then continues to increase. This is consistent with the conclusions reached earlier regarding the effects of inertia. Platen friction also follows approximately the same trend. Initially the material slides along the top platen rapidly after impact. It then reaches a minimum and starts to increase again due to more rapid movement along the top platen and folding of material onto the top and bottom platens as the specimen height reduces.

5.2.2. Comparison Of The Finite Element Model With Experimental Tests On Aluminum.

The data published by Shabaik(7) for quasi-static compression of aluminum was used for the experimental tests to be compared with predictions of the finite element model. The results for deformed shapes are shown in Fig. 5.2.2.1. Strain hardening was assumed with the constitutive relation presented in equation 5.1.4.1.

The master-slave node method for platen friction was assumed in this case with the master node at the top right of the specimen as indicated in Fig. 5.2.2.1. The horizontal velocity at the master node was taken from the experimental values. For this purpose a factor β was defined as the ratio of the horizontal velocity at the master node to the velocity that would occur for the free

boundary if the compression were homogeneous. That is, if V_1 is the horizontal velocity of the master node, and V_H the velocity of the free boundary of a specimen of the same height and volume but deforming homogeneously, then $V_1 = \beta V_H$. This allowed a suitable smoothing of V_1 between experimental points.

A good agreement between the finite element model and the experimentally deformed specimen was obtained. A further comparison with experiment is obtained by examining the flow line diagrams for each case as shown in Figs. 5.2.2.2(a) and (b).

5.3. RIGID PERFECTLY PLASTIC RESULTS.

In the previous section the model was found to give a good agreement to experimental results. It is now possible to proceed to predict results for which experimental comparison is not available.

By definition, a rigid-perfectly plastic material is one with a constant yield stress. As such, the results will be independent of the rate of strain.

Consideration will now be given to the compression in plane strain of a block of rigid-perfectly plastic material. The results of the modelling for this case were compared to upper bound solutions given in section 2.3. Section 5.3.1 considers case 1: The compression of a tall block of height to width ratio (H_o/D_o) of 4. Section 5.3.2 considers case 2: the compression of a short block with $H_o/D_o=0.839$. This section also considers rectangular blocks with $H_o/D_o=0.25$ and 0.125 respectively.

For all cases the material is assumed to have a

constant yield stress of Y_o=106.18MPa, the value for annealed aluminum. Strain hardening and strain rate sensitivity are ignored to isolate the behaviour for $\bar{\sigma}=Y_o$. A constant coefficient of friction of 0.174 for the platens was assumed. This was was the average value obtained with the master-slave node method in section 5.2.2.

5.3.1. Case 1. $H_o/D_o=4$.

Fig. 5.3.1.1 shows the initial mesh used for this case and the deformed shapes at various stages of compression. From an examination of these deformed shapes it was concluded that the upper bound solution discussed in section 2.3 was appropriate for describing the pattern of deformation. This upper bound velocity discontinuity pattern is superimposed on the deformed shapes for comparison.

Figs.5.3.1.2(a) and (b) present velocity distributions for the finite element solution. For comparison with these curves Figs 5.3.1.3(a) and (b) were constructed from the velocity discontinuity patterns and hodographs in Figs. 2.3.1.2 and 2.3.2.1. Before proceeding to describe how these curves were constructed some definitions will be made.

As shown in Fig. 5.3.1.1 an X-Y coordinate system is defined with origin at o, the centre of mass of the specimen. The Y axis is vertical and the X axis horizontal. Each line such as 3-3 is referred to as a y grid line and the results are plotted at nodes along these lines. 3-3 refers to the 3'rd y grid line as it is the third from the left. OA is the first y grid line and IE the 9'th.

Similarly, OI is the first X grid line and AE the 9'th.

The hodograph shown in Fig. 2.3.1.2 indicates that the normalised vertical velocity V_y/V_o is unity in region ABE, 0.75 in BHFE, 0.5 in BCH and FGH,0.25 in ICHG, and 0 in IOC. With these velocities available Fig. 5.3.1.3(a) was constructed by plotting the vertical velocity along the 9'th y grid line with symbol "o", along the 5'th with symbol "◇", and along the first with "□".

The intersections of x and y grid lines define the node points. For each of these node points the value of vertical velocity is dependent upon the region into which it falls. Thus for the 5'th y grid line in Fig. 5.3.1.1 with H/D=2.023, V_y/V_o is zero for the first two nodal points in the region IOC. The velocity then jumps to 0.25 for the third node which falls in region ICHG. The velocity then increases to 0.5 for the 4'th node and stays at that value for the 5'th and 6'th nodes. The velocity then increases again to 0.75 for the 7'th node which falls in region EBHF. The 8'th and 9'th nodes fall in region BAE and hence have a normalised vertical velocity of unity. These points are plotted in Fig. 5.3.1.3(a). Fig. 5.3.1.3(b) for H/D=1.117 was plotted in a similar way.

The comparison of the simple model results in Figs. 5.3.1.3(a) and (b) with the velocities in Figs.5.3.1.2(a) and (b) for the appropriate case shows some very similar trends. The finite element results show velocities for all grid lines but those plotted from the simple model are sufficient to show a similar distribution of velocity spatially for each H/D and a similar trend with

deformation. It is concluded that the simple model gives a satisfactory comparison with the finite element results.

The H/D ratios for comparison in the previous discussion were selected because the velocity discontinuity patterns were reasonably well developed for those values. For each of these cases prior deformation had taken place. In the present finite element model the only cause for any variation in the results for the velocity field, provided the material is not strain hardening, is the shape of the free boundary. It was thus decided to investigate the effect of the boundary shape on the results.

Five cases were considered. Undistorted blocks with H/D ratios of 1.5, 2, 3, and 3.5 were modelled under the same conditions as previously. A 5'th block of H/D=2.023 was considered in which the mesh was equally spaced as for the others but the boundary was distorted to the shape found experimentally. This latter case proved a useful check on any mesh effects which might change the numerical solution. Distorted mesh effects does not in this case amount to a change in the physical model.

The results are shown in Figs.5.3.1.4 and 5.3.1.5. The discontinuity patterns are drawn directly onto the displaced shape plots as previously. The results without the distorted boundary are quite distinct from the results with a distorted boundary. They indicate no tendency to the formation of a concavity in the boundary as in the previous case.

At H/D=2 the result with the undeformed boundary is quite distinct from the one with a deformed boundary at

H/D=2.023. The case of the regular mesh with a deformed boundary is also shown in Fig. 5.3.1.5 and is in good agreement with the result in Fig. 5.3.1.2(a).

In conclusion, the modelling has shown that the simplified model assumed only holds when the boundary is able to distort suitably.

Fig. 5.3.1.6 shows that the critical H/D value for concavity formation for the boundary is between H/D=3 and H/D=3.5. The results suggest that if the specimen is too short formation of a concave boundary cannot occur.

Fig. 5.3.1.7 is a path line plot depicting the flow history for the case shown in Fig. 5.3.1.1. This plot shows quite clearly the change in the mode of deformation at H/D=2.023 suggested by the simple model. For example, the path line ABC corresponds to the path of a point on the boundary of the specimen. A change of curvature in the path followed by this material point occurs at the spatial point B when H/D=2.023. This change of curvature is consistent with the simple models shown in Fig. 2.3.1.2 and Fig. 2.3.2.1. When $H/D \geq 2$ the velocity V_y in region ICHG (see Fig. 2.3.1.2) has a finite y component of velocity. For $H/D < 2$, however, V_y in Fig. 2.3.2.1 has no Y component of velocity. It is thus the development of the region FHG in Fig. 2.3.2.1 that causes the Y components of velocity to decrease and the X components to increase. This results in the observed change of curvature of the path lines at H/D=2.023.

5.3.2. Case 2. $H_o/D_o=0.839$.

Fig. 5.3.2.1 shows the deformed meshes obtained for the compression of a block of rigid plastic material of initial height to width ratio of 0.839. The simple model velocity discontinuities from Fig. 2.3.3.1 are also shown. The velocity patterns are plotted in Fig. 5.3.2.2 and are in good agreement with the predictions of the simple model.

Since for this case the right boundary of the specimen remains straight, the strain history of the specimen will not influence the velocity fields. Thus for the purposes here it will be sufficient to assume that for $H/D<1$ the velocity field for an undistorted block can be used for one that has been strained provided the same volume of material is being considered in each case and the specimen heights are the same. In order to avoid unnecessary computer calculation, unstrained blocks were next considered with the purpose of comparing the velocity patterns in each with the simple model.

Fig. 5.3.2.3 and Fig. 5.3.2.4 show comparisons of the simple model depicted in Fig. 2.3.3.1 with the finite element results for the case of unstrained blocks of the appropriate H/D ratio.

Fig. 5.3.2.3 shows the results for the case H/D=0.25. The top part of this figure shows both the finite element mesh used for the finite element calculations and the velocity discontinuities of the simple model. Also shown with the simple model is a hodograph and the resulting velocity vectors within each of the rigid regions. Since the velocity field must be symmetric about GH in Fig.

5.3.2.3 these velocity vectors are plotted on the lower half of the specimen for clarity.

In region edH the simple model predicts zero y component of velocity while in region cde a finite component of velocity equal to the platen velocity is predicted. The finite element calculations indicate a local maximum in the V_Y in region cde for the intermediate y grid lines CD and EF. Similarly a local minimum in the finite element solution on these grid lines is indicated for region cbd. It can be concluded from the comparison that the simple model for this case does give a satisfactory comparison with the finite element results.

Fig. 5.3.2.4 shows an even more remarkable agreement of the simple model with the finite element solution. Along the CD y grid line the local maxima of V from the finite element results are clearly defined. On the EF y grid line the maxima become less well resolved. This change is also predicted by the simple model because the GH y grid line is made up only of the sides of the rigid regions such as cbd wherein $V_y=0$. As in the previous case the finite element solution does not predict the rigid region aGb. This rigid region is the crude representation in the simple model for the actual boundary condition of V =0.

5.3.3. Load Predictions For The Rigid-perfectly Plastic Case.

Fig. 5.3.3.1 shows a comparison of the finite element results for the rigid-perfectly plastic case with the simple models presented in chapter 2. The method of construction of this graph will first be described.

There are two distinct regimes to consider; namely, H/D>1 and H/D<1. For H/D>1 finite element calculations were done both for a straining history from H/D=4 to H/D=1.117 and for unstrained blocks of H/D= 1.5, 2, 3, and 3.5. The only simple solutions considered for this case were the homogeneous solution and the velocity discontinuity pattern. Both these simple solutions gave $\sigma_Y/2K=1$, where σ_Y is the normal platen traction.

The finite element results for this case are plotted in Fig. 5.3.3.1. The finite element results for the undeformed blocks are in excellent aggreement with the simple model results. A value of $\sigma_Y/2K=1$ with negligible deviation was obtained.

The platen normal tractions for the case of the blocks being strained, however, showed significant deviation. At H/D=4 concavity formation for the boundary occurred. For lower values of H/D, the results from the block being strained differ from those obtained from an unstrained block of the same equivalent H/D.

It is clear that the normal platen traction increases with strain for the case where a concave boundary forms. At H/D=1.433 the platen traction is a maximum with the value at H/D=1.117 somewhat less. Fig. 5.3.1.1 shows that between H/D=1.433 and H/D=1.117 the element at the top right hand corner of the specimen (at point E in Fig. 5.3.1.1) has had one of its sides fold onto the platen.

The reason for the increase of platen traction can now be explained. If a vertical line is drawn down from E in Fig. 5.3.1.1 and the excess material removed from the right

of this line the platen normal traction would be 2K. With the excess material included, however, the amount of material in contact with the platens remains the same but additional platen traction is required because of the extra power involved in distorting the additional material.

It is also of interest to compare a result quoted in ref. 28, originally due to Hill, for the case of compression with overhanging platens. This solution is plotted in Fig. 5.3.3.1 for comparison. In the case of overhanging platens D refers to the width of the platens rather than the specimen width. The comparison shows that the increase of traction is well below that which would occur for a very wide specimen where the platens would essentially be indenters. In this respect the comparison is consistent.

Different considerations apply for the case H/D<1 in Fig. 5.3.3.1. In this case the effects of platen friction will become more important than in the case of H/D>1 because of the larger amount of material in contact with the platens and the increased velocity of sliding that occurs with wide specimens. The simple model in Fig. 2.3.3.1 can be expected to apply only for low values of friction since the rigid blocks must be able to slide along the platens. Thus σ_y=2K will not be a good estimate for significant values of the coefficient of friction.

Plotted in Fig. 5.3.3.1 are the points corresponding to an undistorted right boundary corresponding to the cases shown in Figs.5.3.2.3 and 5.3.2.4. Also plotted in Fig. 5.3.3.1 are the points corresponding the distorted boundary

case which involved straining from H/D=0.839. This latter case is the one shown in Fig. 5.3.2.1.

All the finite element results involved significant values of the friction coefficient with the result that the platen traction of σ_y=2K was significantly exceeded. Most of the finite element results are in good agreement with the slip line field solution given by Hill and plotted in Fig. 5.3.3.1.

It can be concluded that the finite element results for the rigid-perfectly plastic case gave results that are consistent with approximate closed form solutions.

5.4. RIGID PLASTIC STRAIN HARDENING AND STRAIN RATE SENSITIVE RESULTS.

For this case equation 5.1.4.2 for plasticine was used to describe the strain rate sensitivity. This relation implies that there is no strain hardening and the quasi-static yield stress is zero.

Figs. 5.4.1.1 and 5.4.1.2 show the deformation patterns and velocity fields calculated. These results parallel those presented in Figs. 5.3.1.1 and 5.3.1.2(a). For consistency with the results in Fig. 5.3.1.1 the platen coefficient of friction was taken as 0.174 and the glass friction was taken as zero.

The results in Fig. 5.4.1.1 show that no concavity develops in this case and the velocity curves in Fig. 5.4.1.2 show very little dispersion. The velocities are essentially those of the homogeneous solution.

Conceptually the strain rate sensitivity of the material prevents a concentration of deformation from

occurring. The velocity discontinuities in Fig. 5.3.1.1 can be regarded as concentrated lines of deformation. The strain rate sensitivity of the material would make these lines have a large effective stress. Homogeneous deformation thus occurs rather than concentrated bands of deformation.

Calculations were done for other H/D ratios with results that were consistent with this interpretation.

5.4.1. Strain Hardening Results For H/D>1.

Strain hardening can be expected to have the same effect as strain rate sensitivity. However, the effect can be expected to be delayed somewhat because strain is required to increase the yield stress of the material. Initially the solution will be the same as for the constant yield stress case but as straining takes place the deformation bands in the material will harden and force material away from the bands to distort. Thus strain hardening should lead to homogeneous deformation as does strain rate sensitivity.

Fig. 5.4.2.1 to 5.4.2.3 show the results for the strain hardening case and can be compared with 5.3.1.1 to 5.3.1.2(b) for the constant yield stress case and to 5.4.1.1 and 5.4.1.2 for the strain rate sensitive case. The results show that, in the strain hardening case, a concave boundary does form as previously. However, strain hardening prevents it from forming to the same depth.

Fig. 5.4.2.2 for the velocity curves when compared with those in Fig. 5.3.1.2(a) shows the effect of strain hardening very clearly. Even at H/D=3.327 the dispersion in

the curves for Y<12mm is reduced in Fig. 5.4.2.2 when compared with that in Fig. 5.3.1.2(a).

For lower values of H/D the effect is more pronounced. At H/D= 2.023, for example, the curves for the constant yield stress case show that the y components of velocity are essentially antisymmetric about a horizontal line drawn in the specimen at y=10mm if this line is considered to have a zero y component of velocity. For the strain hardening case in Fig. 5.4.2.2, however, the y components of velocity indicate that the velocities are closer to the homogeneous values for y<10mm than they are for y>10mm.

Comparison of Fig. 5.4.2.3 for H/D=1.433 with Fig. 5.3.1.2(b) indicates that in the strain hardening case the inversion in the curves about a common point no longer occurs. In the constant yield stress case this inversion occurs when H/D=1.218. The absence of the inversion in the V_y velocity curves at higher values of H/D in the strain hardening case than in the constant yield stress case indicates that the development of the concave boundary persists in the latter case for higher strain levels in compression.

It is thus concluded that the expected results for the strain hardening case hold; namely, that straining causes the concentrated bands of deformation that occur in the constant yield stress case to harden. This, in turn forces the spread of deformation and a more uniform energy density to occur spatially in the material than in the constant yield stress case.

5.5. THE DYNAMIC COMPRESSION OF ALUMINUM.

The purpose of this section is to examine the effect of inertia on the deformation patterns in aluminum. The calculations were done using equation 5.1.4.1 for the variation of yield stress with strain hardening. A constant coefficient of friction of 0.174 was assumed on the platen boundaries. This was the average value obtained from the calculations in section 5.2.2 in which the master slave node method was used.

The top boundary of the specimen was initially given an acceleration of 10^{20}m/s^2 to a speed of 100m/s to approximate an infinite acceleration. The speed of 100m/s was maintained until t=37.69μs. The top platen velocity was then set to zero with the result that the top boundary of the specimen moved away from the platen.

Displaced shape plots are presented in Figs. 5.5.1 and 5.5.2. The top of the specimen initially was displaced the most with the lower part of the specimen not being affected by the impact. The displaced shape plot in Fig. 5.5.2 for t=23.91μs indicates this time that the bottom part of the specimen is moving approximately as much as the top.

One effect of inertia is thus to make the material move nonsymmetrically about the horizontal centre line of the specimen shown in EF in Fig. 5.5.1. In the absence of inertia the pattern would be symmetric about this line.

At t=23.91μs the displacement pattern has become approximately symmetric about EF but the curvature of the y grid lines is distinct from that observed in Fig. 5.3.2.1 for example. Strain hardening would account to a certain

extent for the suppression of any deformation bands in the material but not to the extent observed in Figs. 5.5.1 and 5.5.2. Thus even when the pattern has become symmetric about EF inertia effects are still very dominant. At t=37.69μs in Fig. 5.5.2, for example, the change of curvature of the y grid lines at GF is consistent with the formation of deformation bands as a comparison with Fig. 5.3.2.1 indicates. At the top of the specimen, however, the curvature of the y grid lines is similar to that shown in the deformed meshes for plasticine presented in section 5.2.1. Plasticine has been shown to be strain rate sensitive which leads to homogeneous deformation.

These observations show that initially there is a transient effect as all parts of the specimen are unequally accelerated from a stationary condition. When this transient effect is complete inertia is still dominant in causing homogeneous deformation. In the present case being considered inertia effects are dominant over effects of material properties and the deformation profiles can be expected to be essentially independent of the material constitutive behavior assumed.

The displaced shape plot for t=45.11μs in Fig. 5.5.2 is for the unloading case. The fact that significant movement occurs when the top platen that was initially deforming the specimen was removed in the calculation is indicative of the fact that inertia effects are dominant. The top of the specimen tends to move in more at the centre than at the edge. Essentially an unloading wave is moving into the specimen from the top right corner.

5.6. STRESS RESULTS.

5.6.1. Stress Results For Rigid-perfectly Plastic Quasi-static Compression.

In this section the normal stress on the top platen will be examined on blocks of rigid-perfectly plastic material for a wide range of H/D. The stresses for the cases shown in Figs. 5.3.1.4 , 5.3.2.3 and 5.3.2.4 will be examined.

Figs. 5.6.1.1 and 5.6.1.2 show the normal platen stresses for various H/D for unstrained blocks of rigid-perfectly plastic material. The results show that for H/D>2 the normal stresses on the platen can be quite different than the same stress components within the material. A friction hill does not hold in the case of H/D>2.

Also shown in Fig. 5.6.1.1 are the stresses for a specimen with H/D=2.023 with pre-strain to show that the conclusion is not affected by the boundary shape.

5.6.1.2, however, shows that friction hills do hold for flat specimens of small H/D. In this case the boundary stresses do not deviate significantly from the values in the material away from the platens.

Fig. 5.6.1.3 summarises the platen normal stresses for various H/D ratios and various material characteristics. Fig.5.6.1.3(a) shows that for a rigid-perfecly plastic material a friction hill only occurs when H/D>0.45. For higher H/D values an inverse friction hill holds.

Fig. 5.6.1.3(b) shows that for the strain hardening case a friction hill exists at higher values of H/D than

for the constant yield stress case. Similarly, Fig. 5.6.1.3(c) shows that for the strain rate sensitive case a friction hill holds at all the H/D values given.

These observations are consistent with the conclusions reached earlier; namely, that both strain hardening and strain rate sensitivity lead to homogeneous deformation. As the effective deformation rate becomes uniform throughout the material a friction hill will tend to form on the platens. This follows from the simple solution in section 2.2 which assumes that the stress over a vertical plane in the material is uniform.

5.6.2. Stress Results For Dynamic Compression.

Figs. 5.6.2.1 and 5.6.2.2 show the stress results for dynamic compression of aluminum considered in section 5.5. The results indicate that a friction hill holds on the top boundary in all cases but that an inverse friction hill holds on the lower boundary initially. At t=23.1 s, however, a friction hill also starts to form on the lower platen. Inverse friction hill on the lower boundary is a dynamic effect.

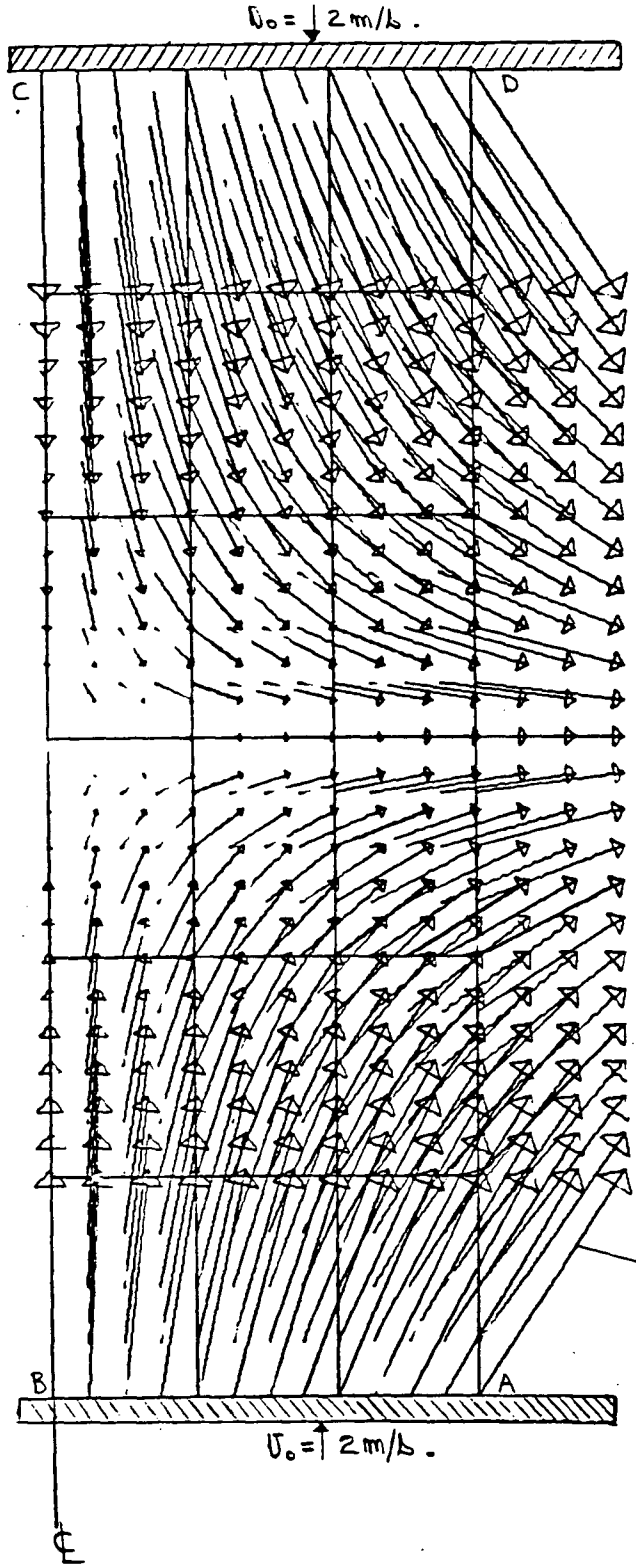

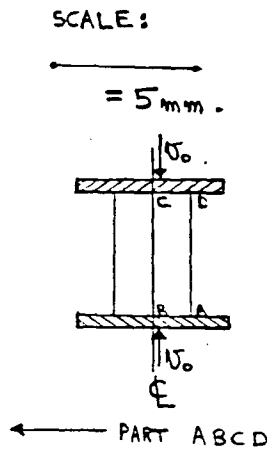

FIG. 5.1.1.1.

VELOCITY FIELD FOR HOMOGENEOUS COMPRESSION BETWEEN FRICTIONLESS PLATES .

VELOCITY VECTORS

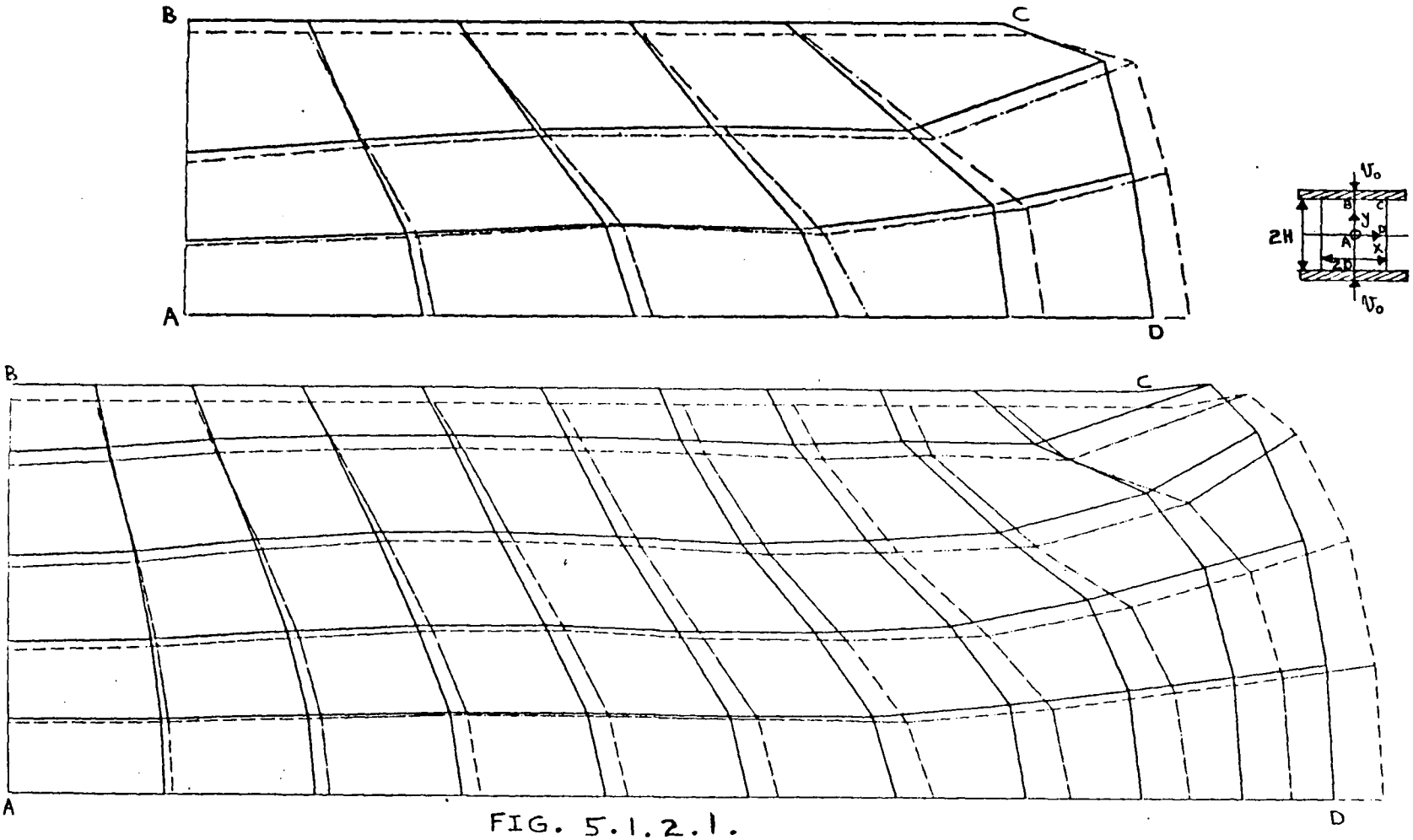

FIG. 5.1.2.1.

COMPARISON FOR ALUMINIUM BETWEEN 15 ELEMENT AND 50 ELEMENT PREDICTIONS OF DEFORMED SHAPES FOR $H/H_o = 0.582$ (SOLID LINE) AND $H/H_o = 0.559$ (DOTTED LINE).

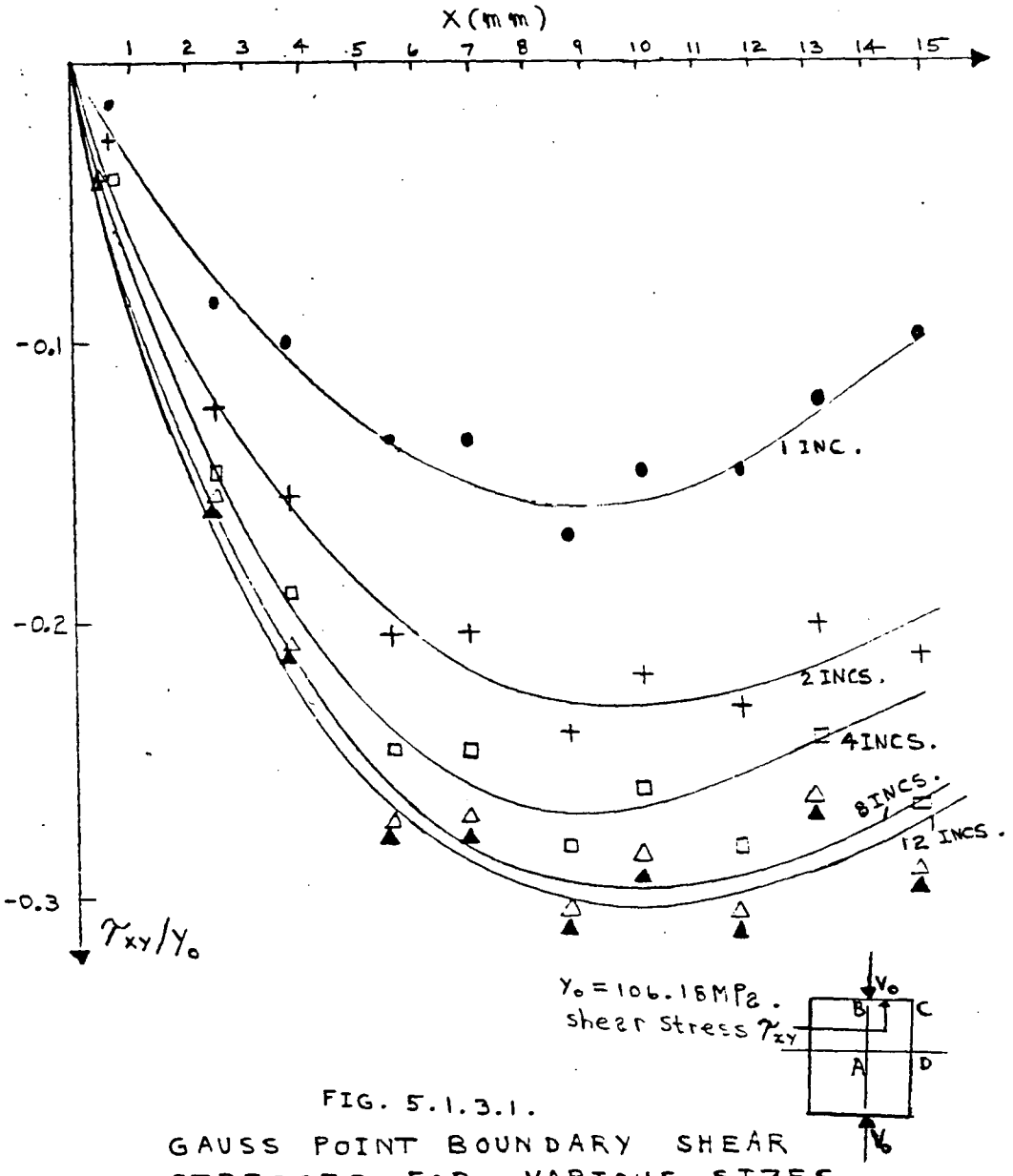

FIG. 5.1.3.1.

GAUSS POINT BOUNDARY SHEAR STRESSES FOR VARIOUS SIZES OF INCREMENTAL STRAIN STEPS TO ACHIEVE A FRACTIONAL HEIGHT REDUCTION OF 0.831 .

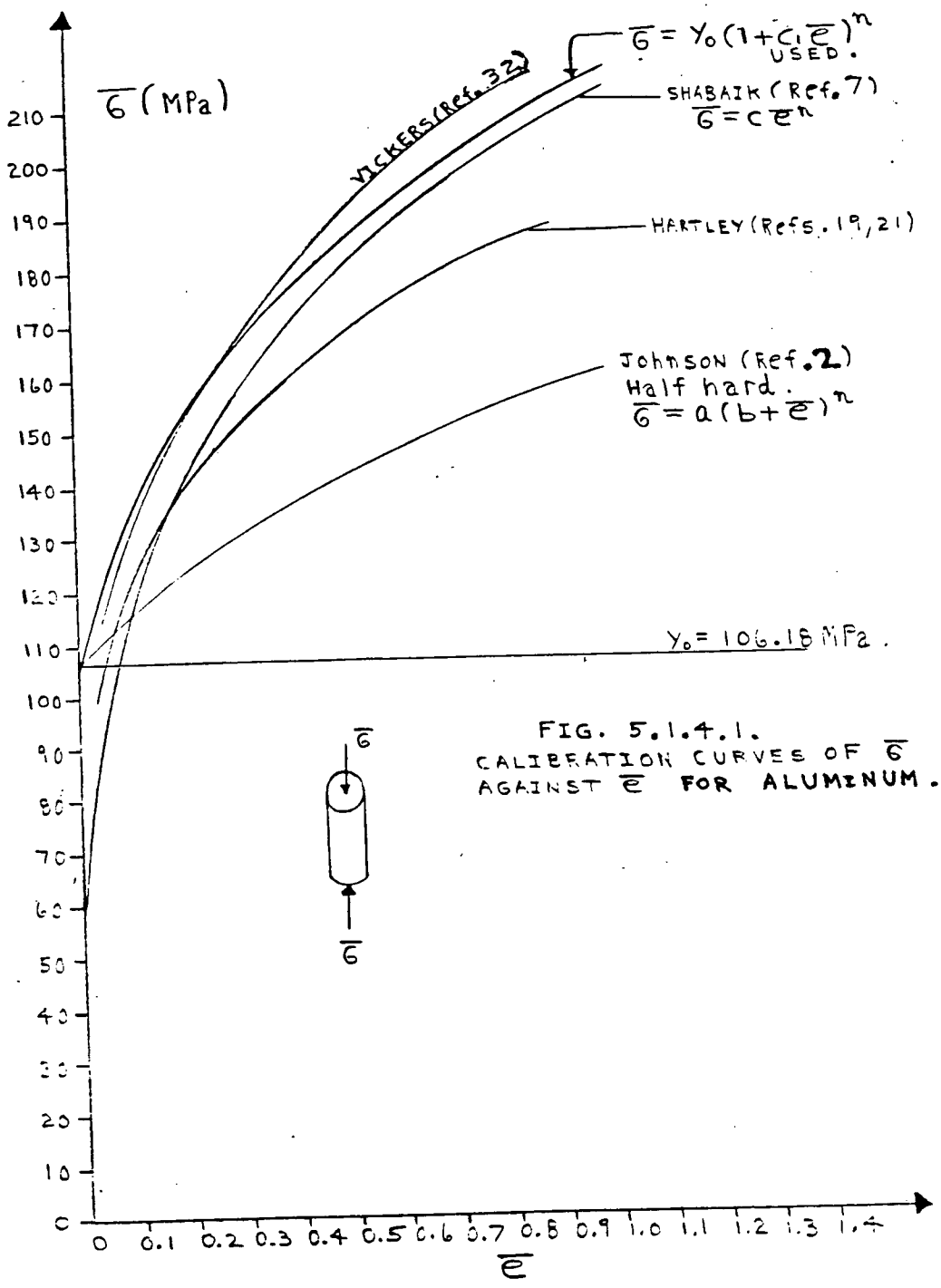

FIG. 5.1.4.1.
CALIBRATION CURVES OF $\bar{\sigma}$ AGAINST $\bar{\varepsilon}$ FOR ALUMINUM.

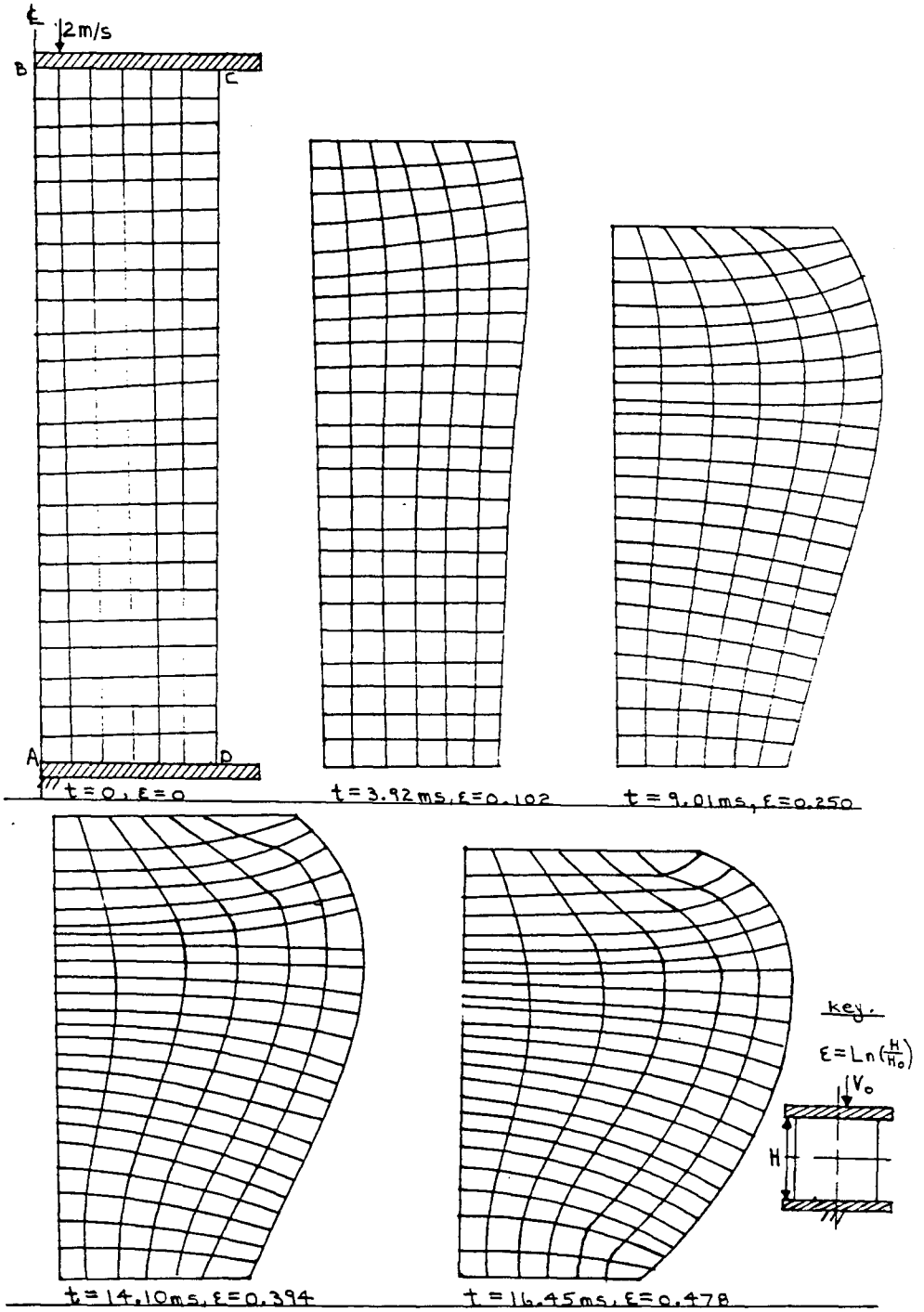

FIG. 5.2.1.1.

EXPERIMENTAL DEFORMED PROFILES FOR THE PLANE STRAIN COMPRESSION OF PLASTICINE.

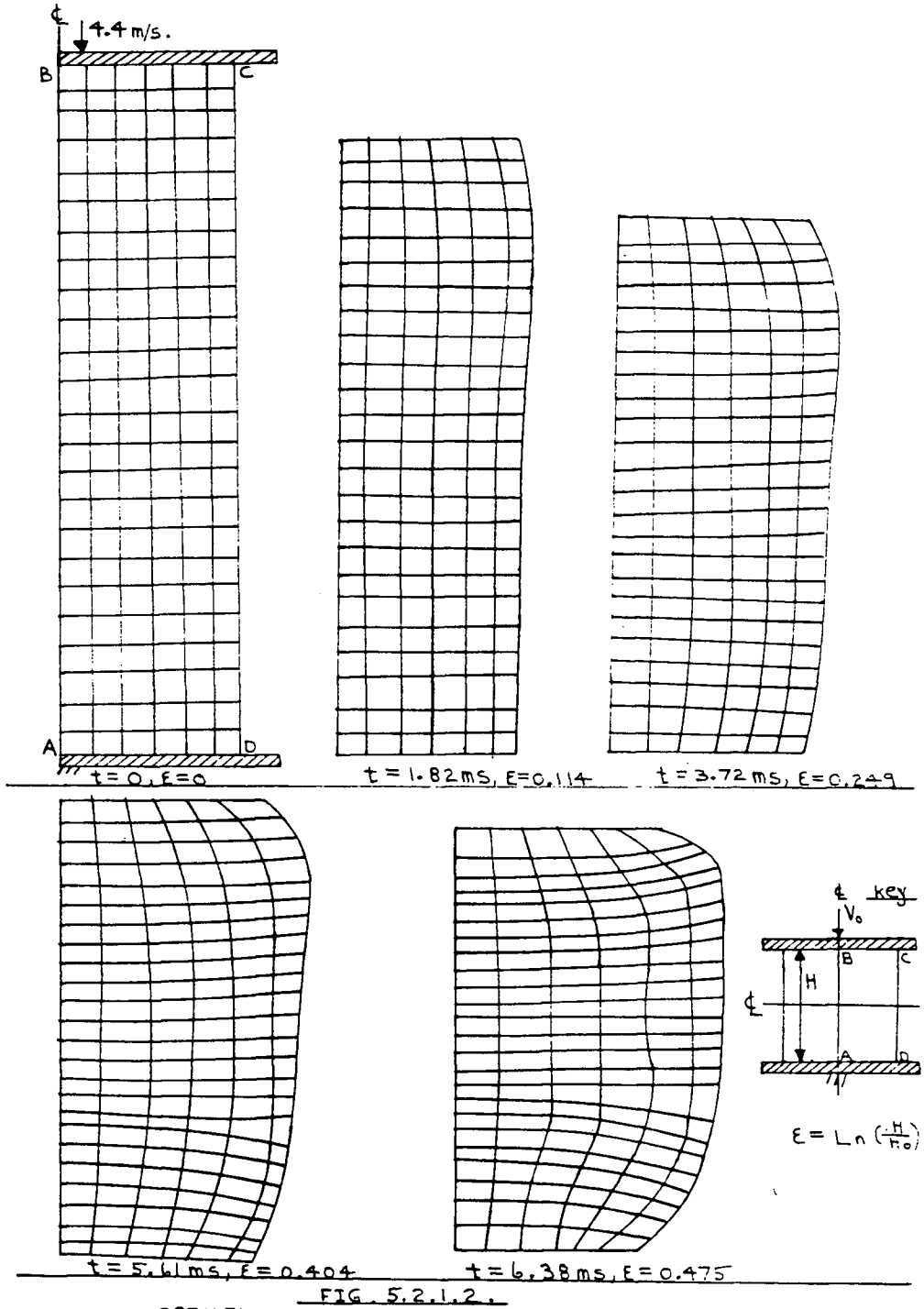

FIG. 5.2.1.2.

EXPERIMENTAL DEFORMED PROFILES FOR THE PLANE STRAIN COMPRESSION OF PLASTICINE.

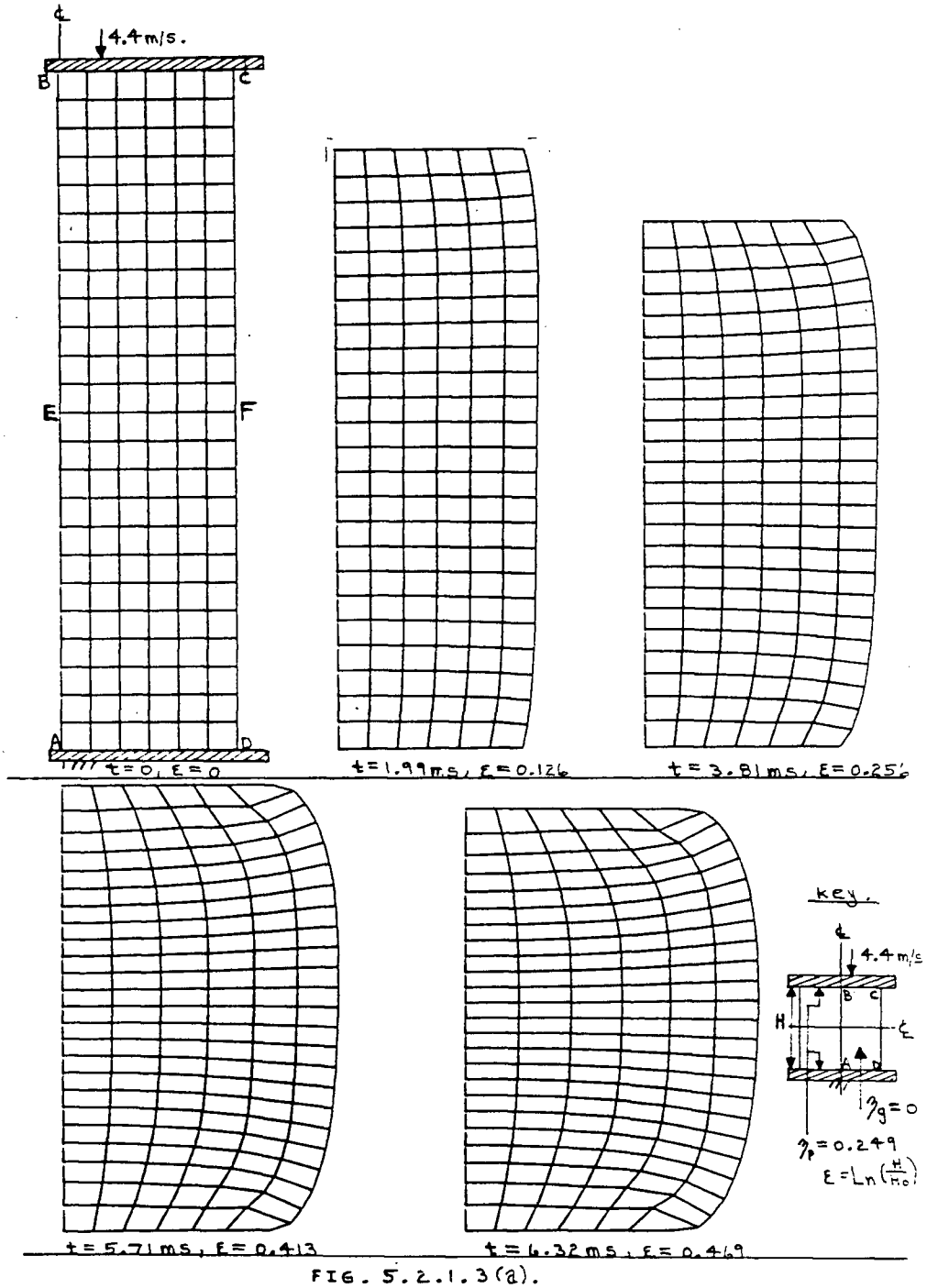

FIG. 5.2.1.3(a).

THEORETICAL DEFORMED PROFILES FOR t = 0 TO 6.32 ms FOR THE PLANE STRAIN DYNAMIC COMPRESSION OF PLASTICINE AT 4.4 m/s WITH $\gamma_g = 0$.

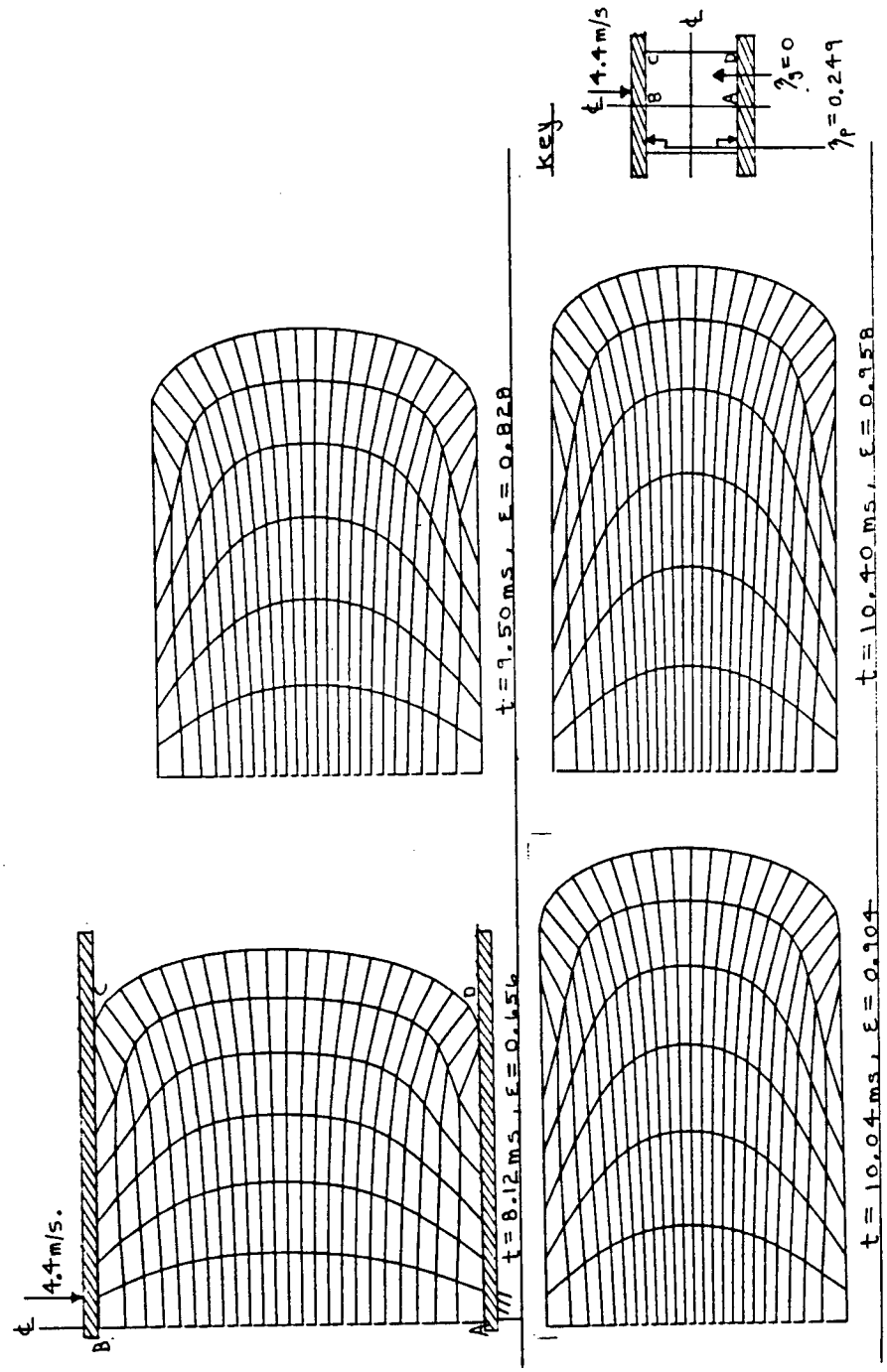

FIG. 5.2.1.3(b).
THEORETICAL DEFORMED PROFILES FROM t = 8.12ms TO 10.40ms FOR THE PLANE STRAIN DYNAMIC COMPRESSION OF PLASTICINE AT 4.4 m/s WITH $\gamma_g = 0$.

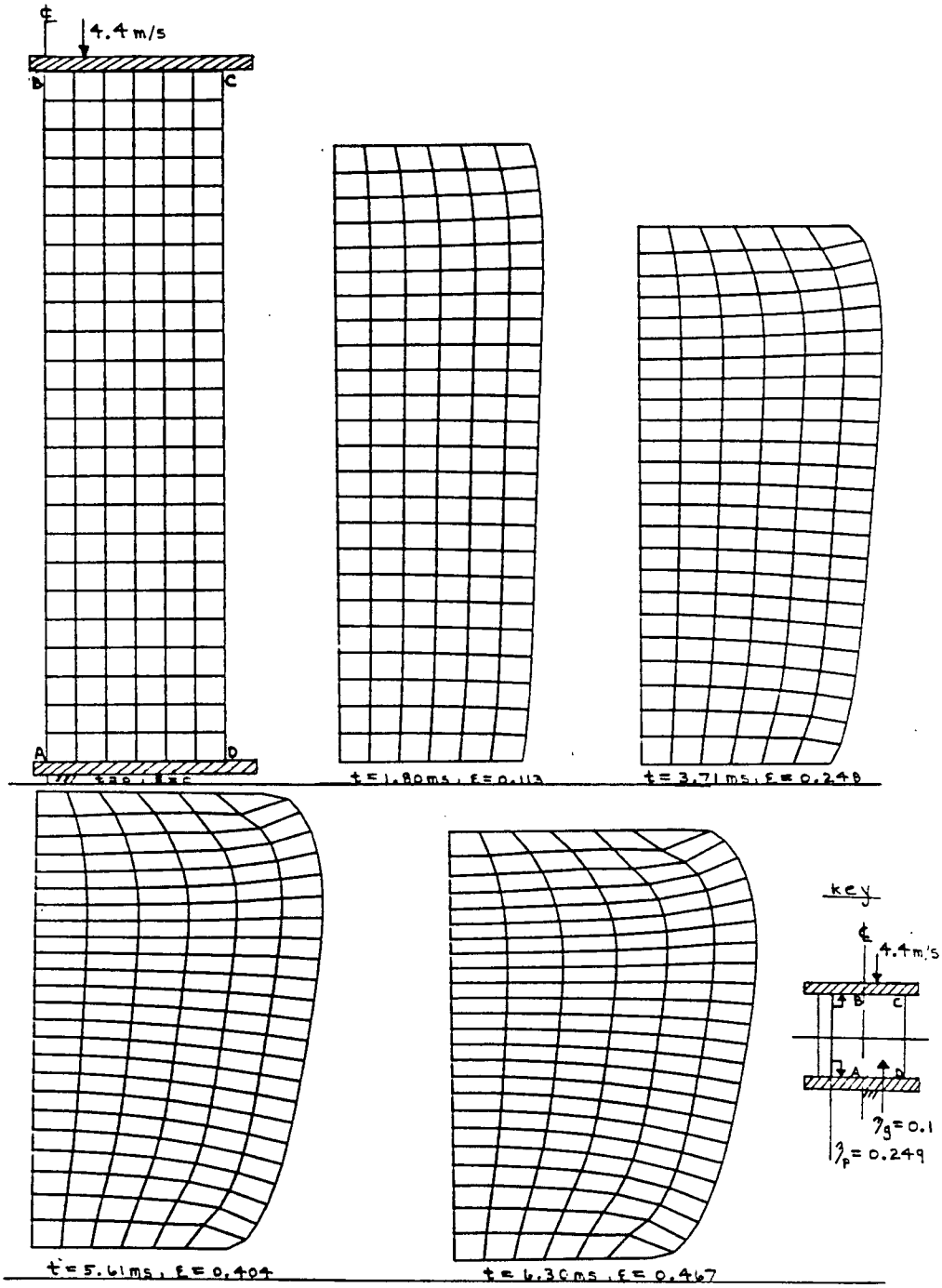

FIG. 5.2.1.4(a).

THEORETICAL DEFORMED PROFILES FROM $t = 0$ TO 6.30ms FOR THE PLANE STRAIN DYNAMIC COMPRESSION OF PLASTICINE AT 4.4 m/s WITH $\gamma_g = 0.1$.

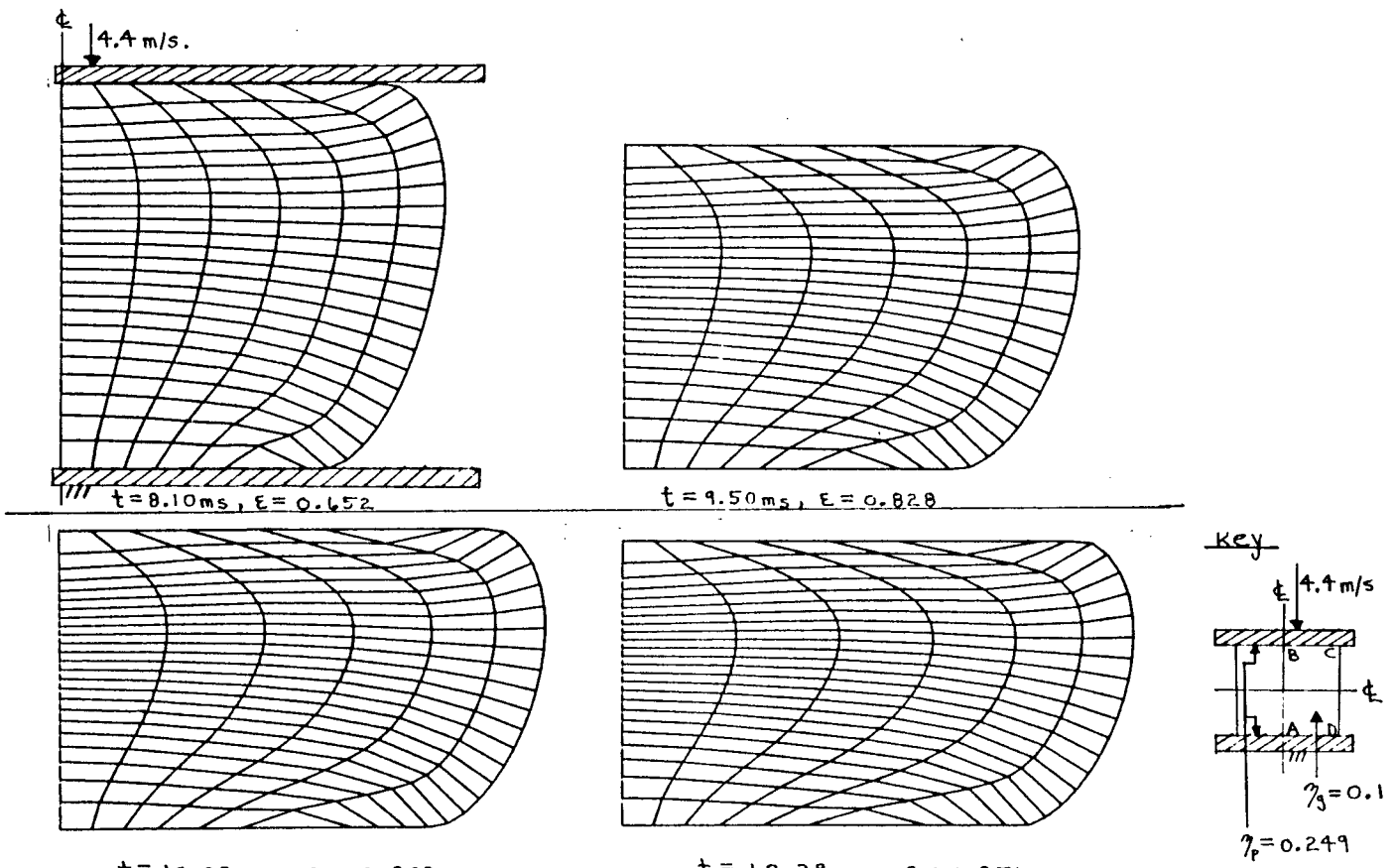

FIG. 5.2.1.4(b).

THEORETICAL DEFORMED PROFILES FROM t = 8.1ms TO 10.39 ms FOR THE PLANE STRAIN DYNAMIC COMPRESSION OF PLASTICINE AT 4.4 m/s WITH $\gamma_g = 0.1$.

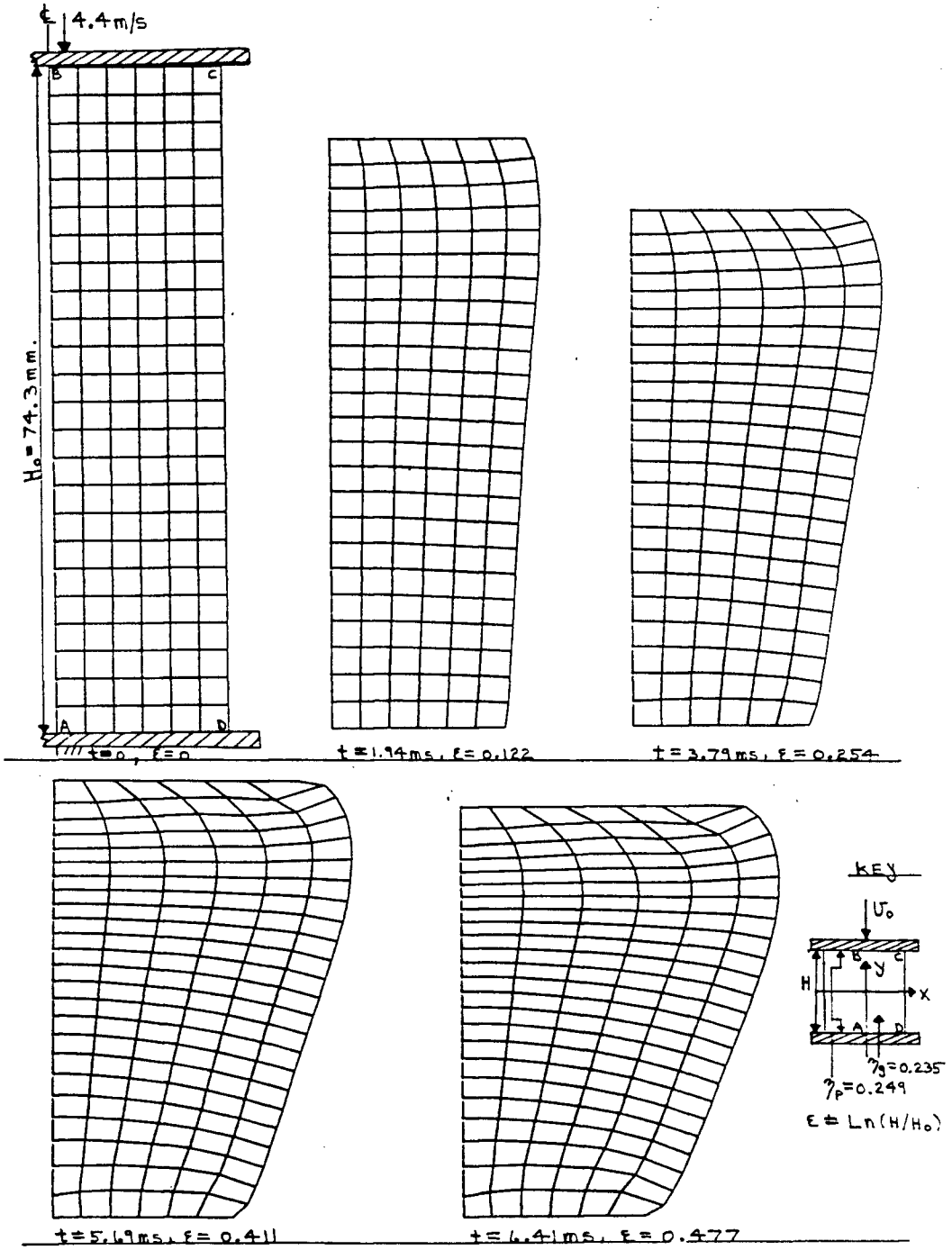

FIG. 5.2.1.5(a).

THEORETICAL DEFORMED PROFILES FROM t = 0 TO 6.41 ms FOR THE PLANE STRAIN DYNAMIC COMPRESSION OF PLASTICINE AT 4.4 m/s WITH γ_g = 0.235 .

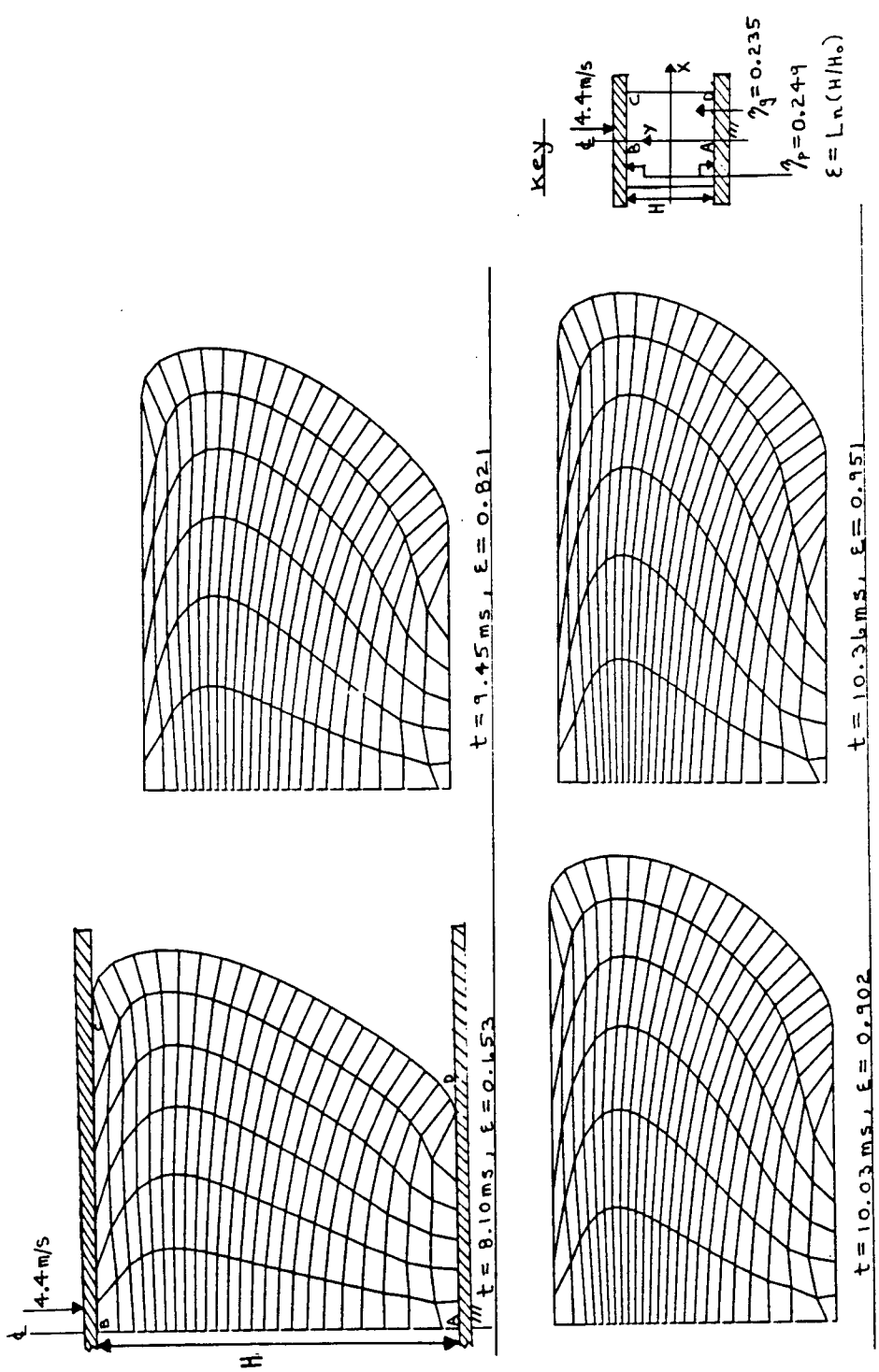

FIG. 5.2.1.5(b).
THEORETICAL DEFORMED PROFILES FROM t = 8.1ms TO 10.36 ms FOR THE PLANE STRAIN DYNAMIC COMPRESSION OF PLASTICINE AT 4.4 m/s WITH γ_g = 0.235 .

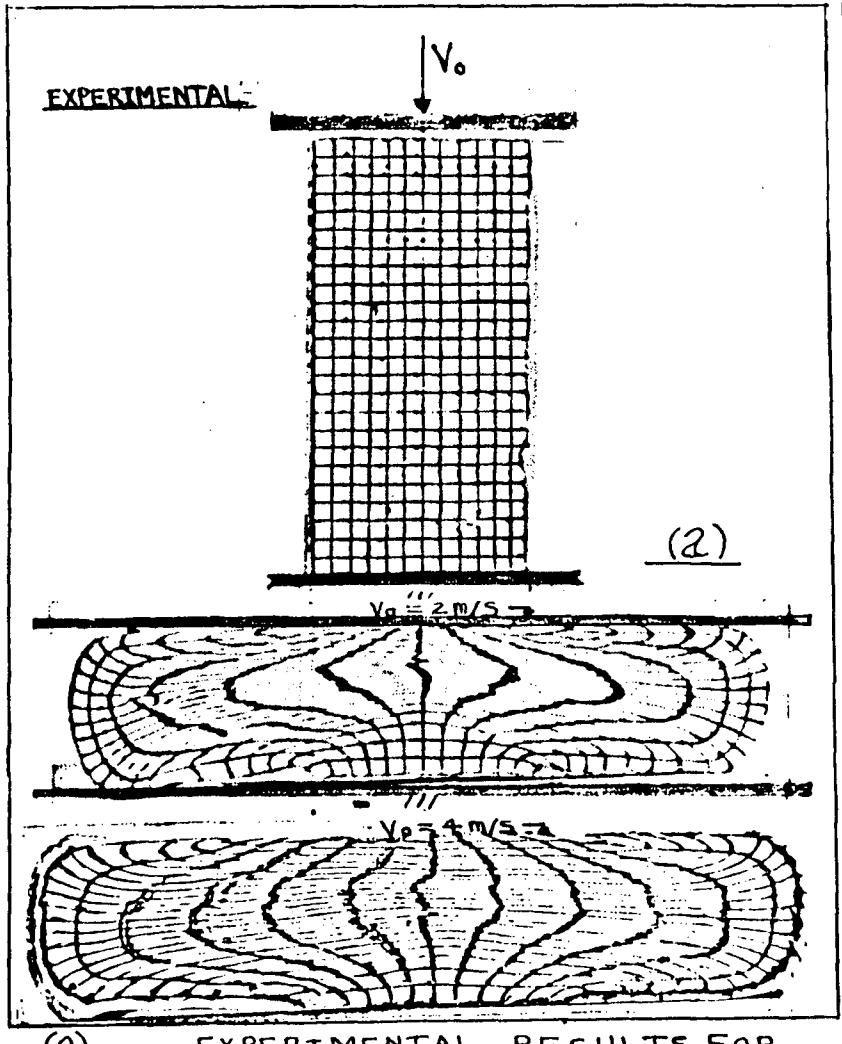

(a). EXPERIMENTAL RESULTS FOR THE PLANE STRAIN COMPRESSION OF PLASTICINE.

(b) THEORETICAL RESULTS FOR THE DYNAMIC PLANE STRAIN COMPRESSION OF PLASTICINE FOR THREE VALUES OF GLASS FRICTION COEFFICIENT, η_g, OF 0.235, 0.1, AND 0. A PLATEN FRICTION COEFFICIENT, η_p, OF 0.249 WAS USED FOR ALL CASES.

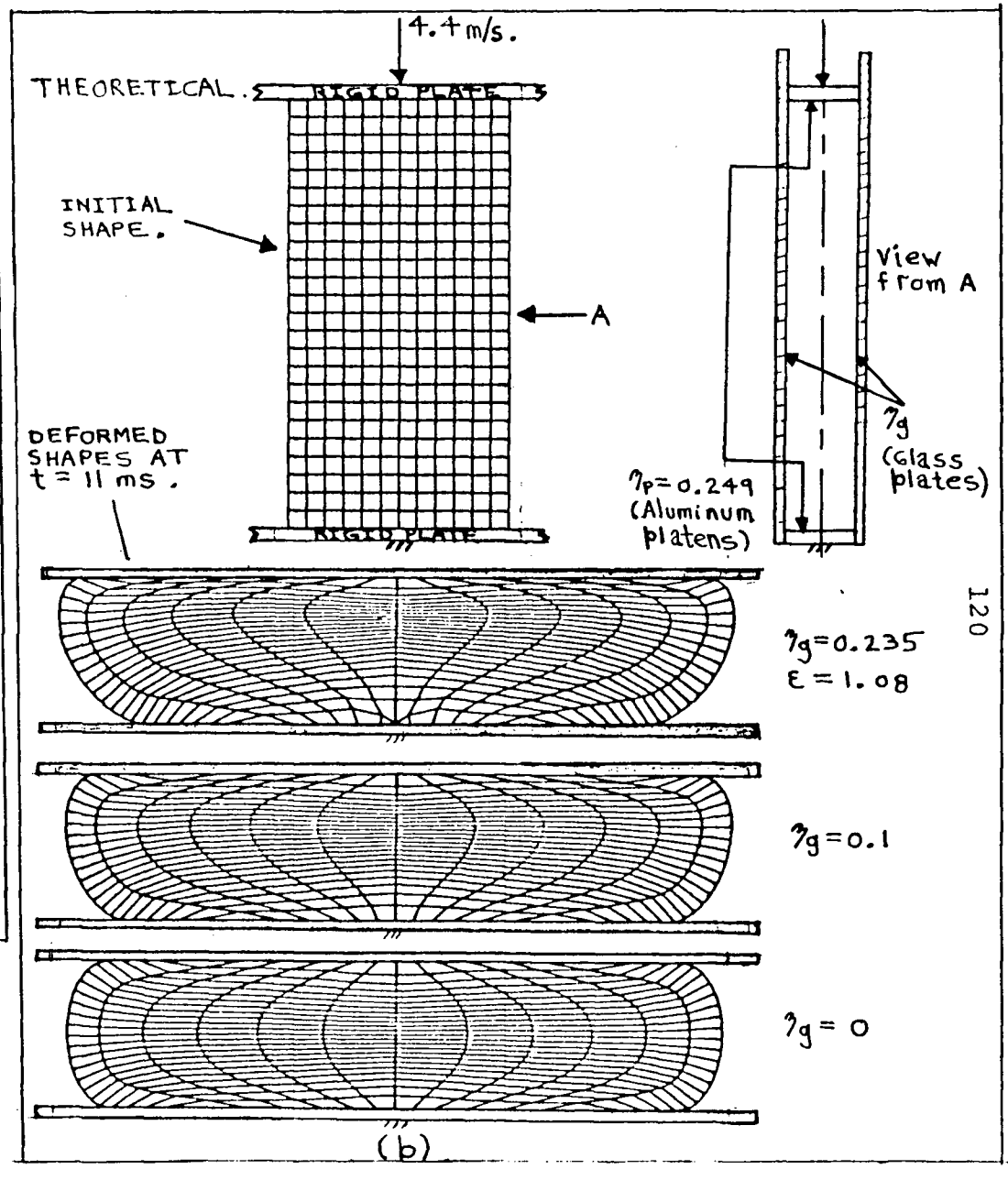

FIG. 5.2.1.b.

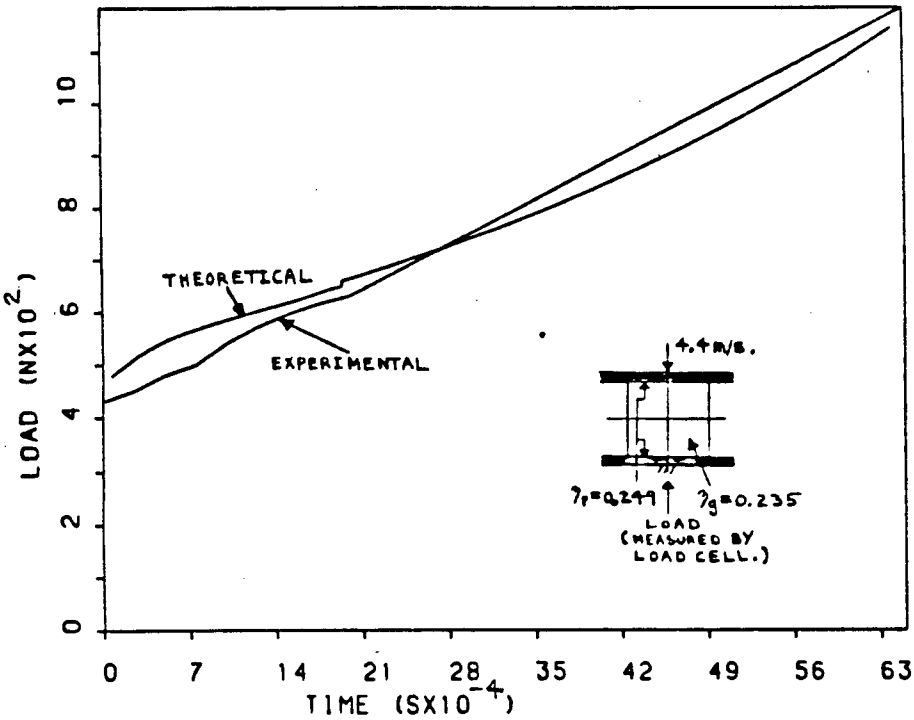

FIG. 5.2.1.7(a).
EXPERIMENTAL AND CALCULATED LOADS FOR PLASTICINE.

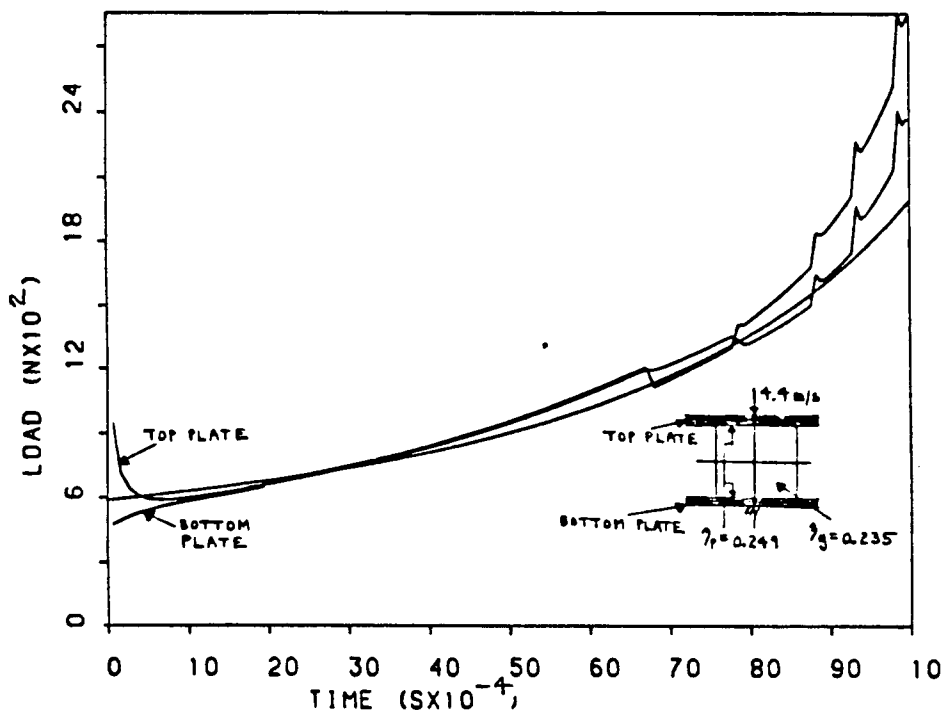

FIG. 5.2.1.7(b).
CALCULATED LOADS FOR PLASTICINE.

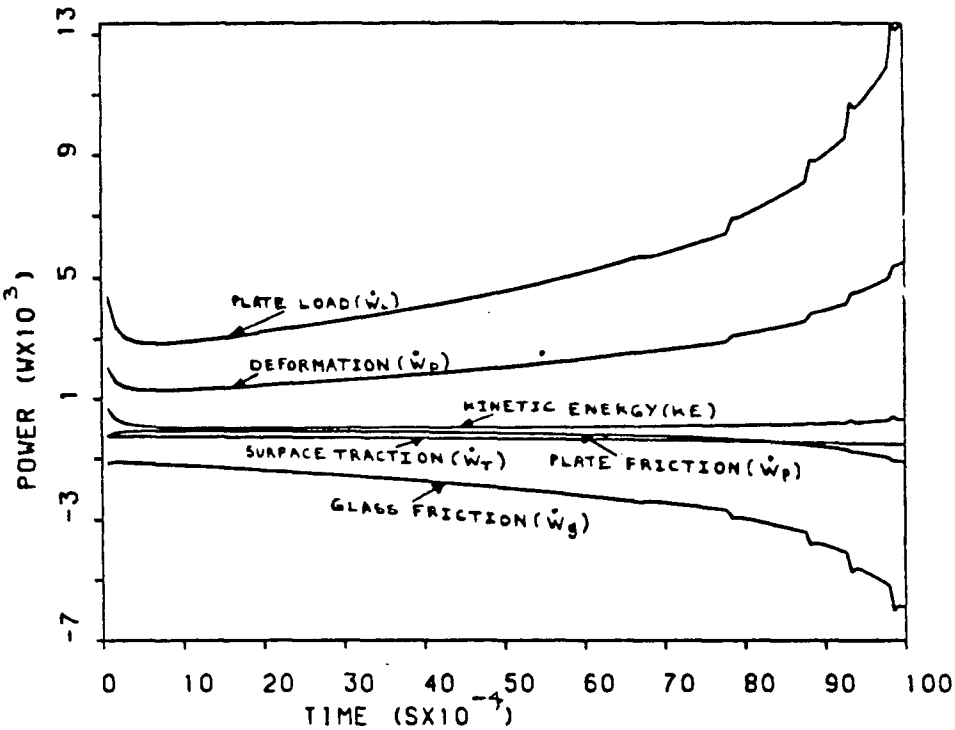

FIG. 5.2.1.8(a).
POWER DISTRIBUTION FOR PLANE STRAIN COMPRESSION OF PLASTICINE.

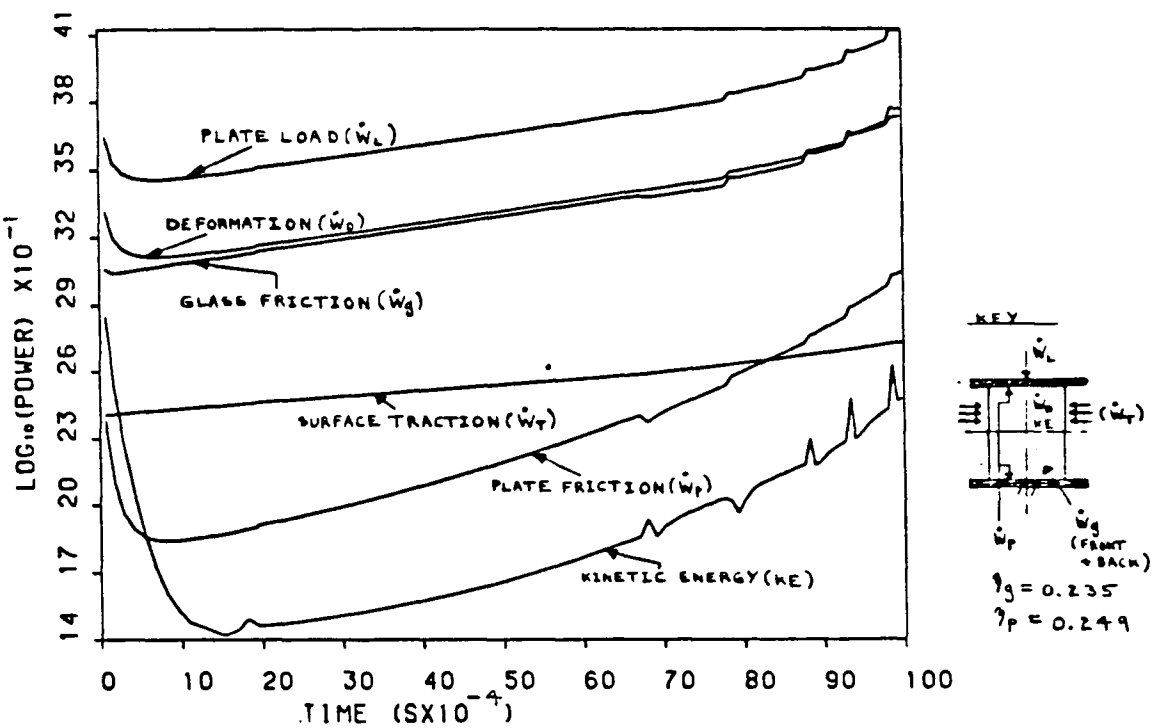

FIG. 5.2.1.8(b).
POWER DISTRIBUTION FOR PLANE STRAIN COMPRESSION OF PLASTICINE.

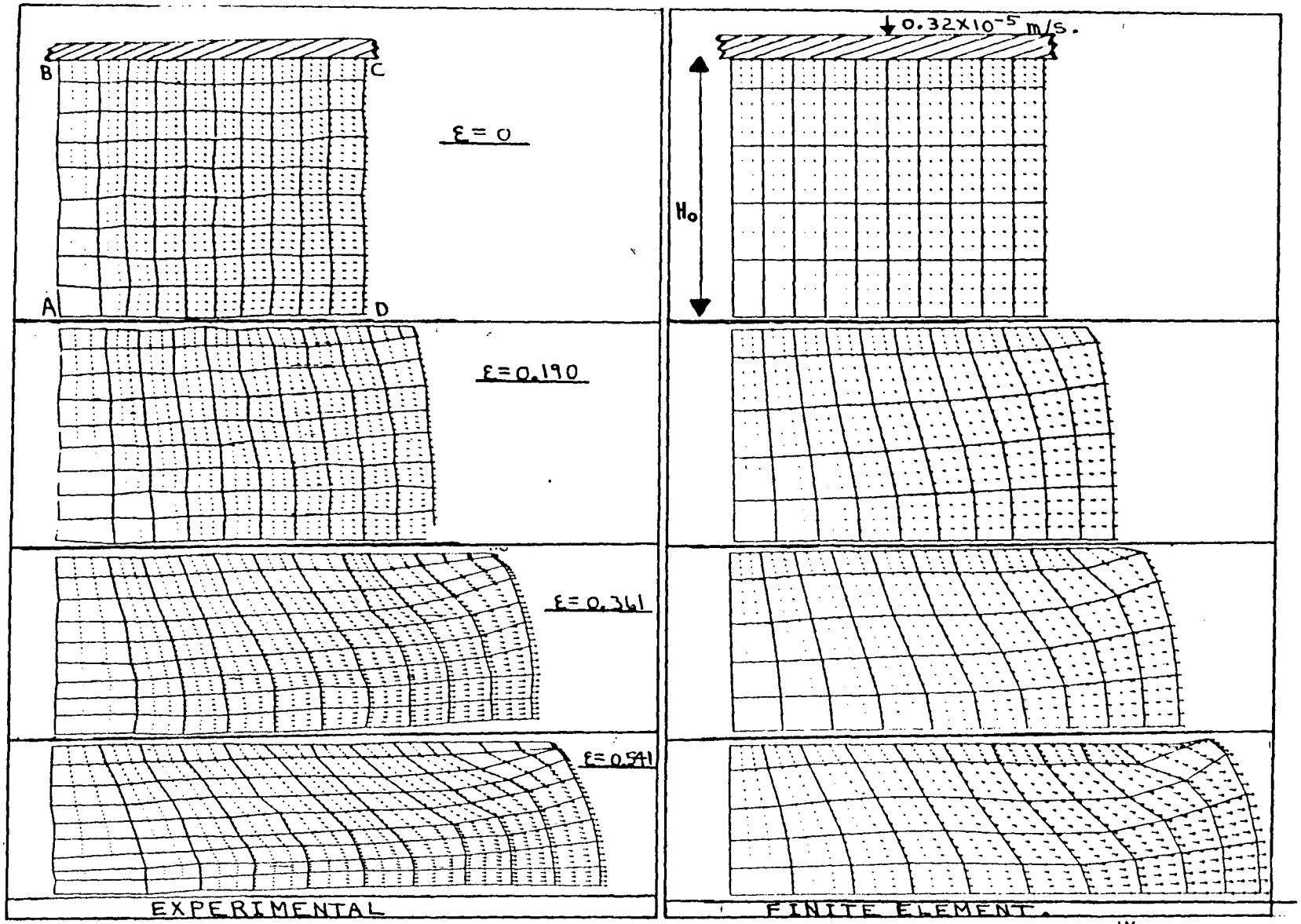

FIG. 5.2.2.1.

COMPARISON FOR ALUMINUM OF EXPERIMENTAL AND FINITE ELEMENT DEFORMED PROFILES WITH VELOCITY VECTORS.

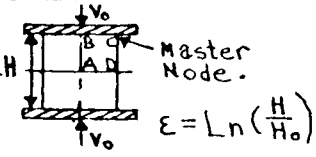

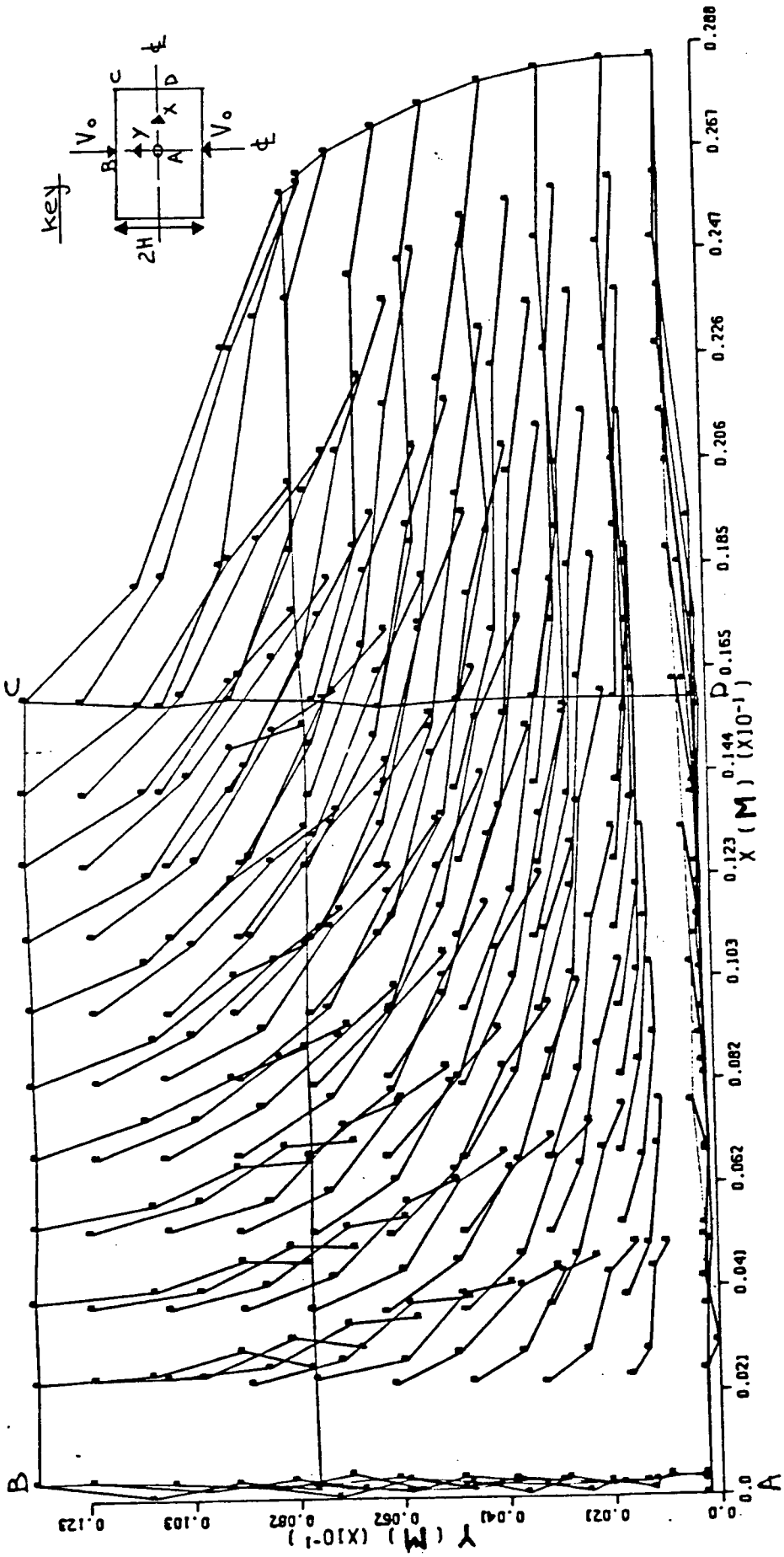

FIG. 5.2.2.2(a).

AN EXPERIMENTAL FLOW PLOT FOR THE PLANE STRAIN COMPRESSION OF ALUMINUM.

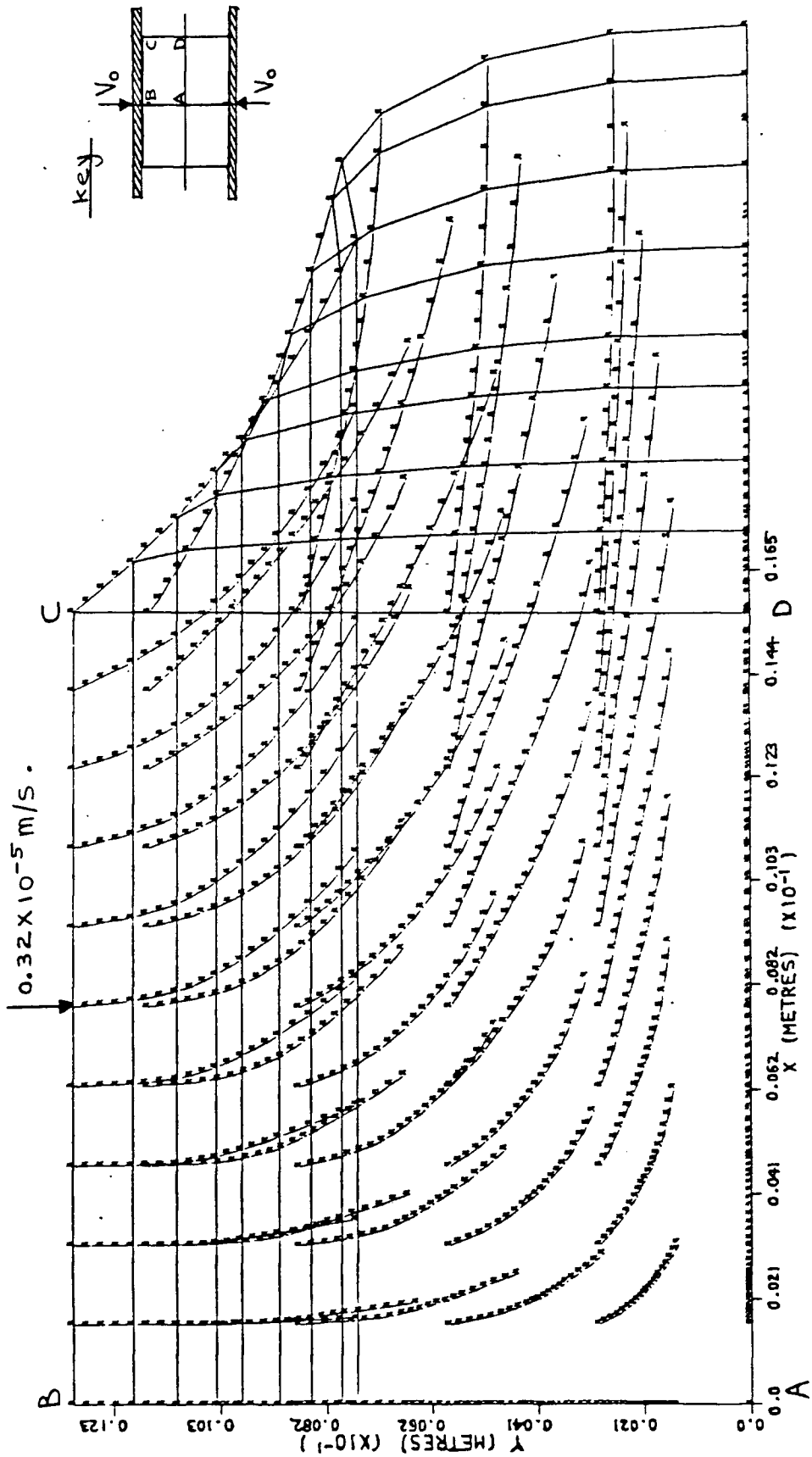

FIG. 5.2.2.2.(b).

THEORETICAL FLOW PLOT CORRESPONDING TO THE EXPERIMENTAL FLOW PLOT GIVEN IN FIG. 5.2.2.2(a).

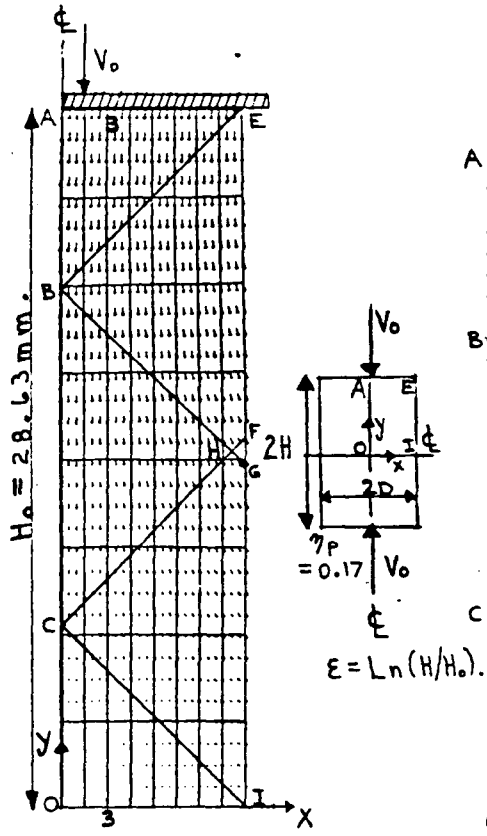

$\varepsilon = 0$
$H/D = 3.826$

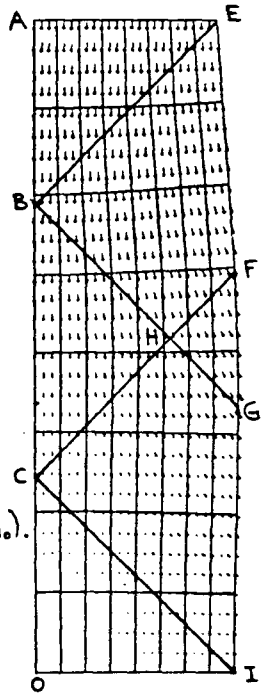

$\varepsilon = 0.092$
$H/D = 3.327$

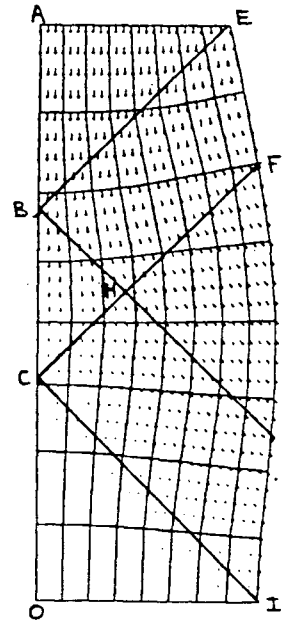

$\varepsilon = 0.217$
$H/D = 2.593$

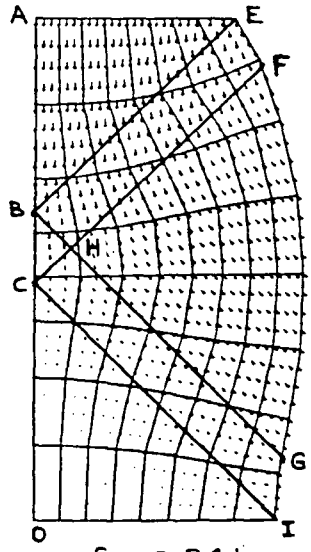

$\varepsilon = 0.341$
$H/D = 2.023$

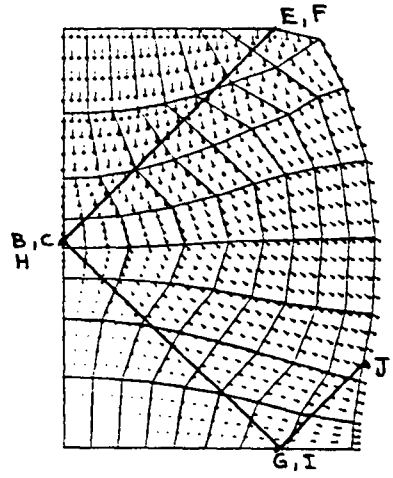

$\varepsilon = 0.512$
$H/D = 1.433$

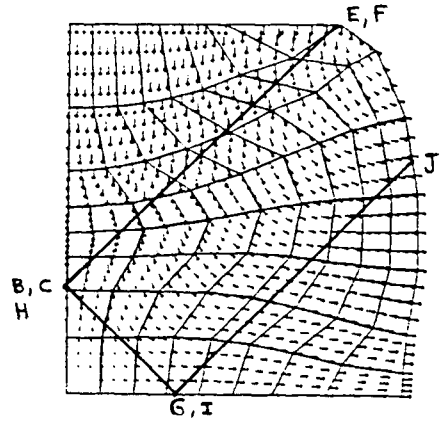

$\varepsilon = 0.639$
$H/D = 1.117$

FIG. 5.3.1.1.

DEFORMED SHAPES WITH VELOCITY VECTOR PLOTS AT VARIOUS STAGES OF COMPRESSION FROM $H_o/D_o = 4$ FOR CASE 1. A PROPOSED UPPER BOUND SOLUTION IS ALSO GIVEN.

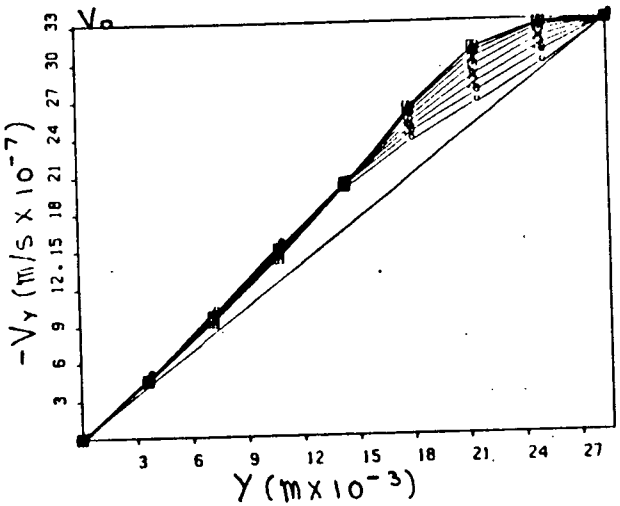

$\varepsilon = 0.022$ $\quad H/D = 3.826$

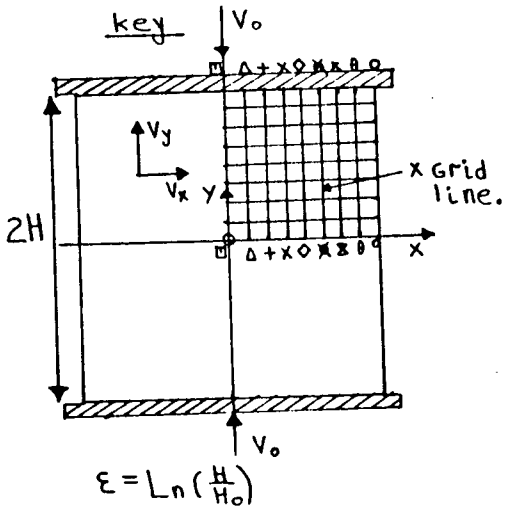

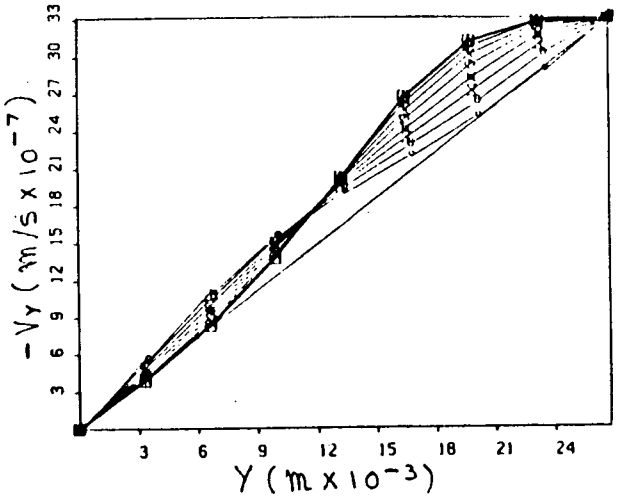

$\varepsilon = 0.092$ $\quad H/D = 3.327$

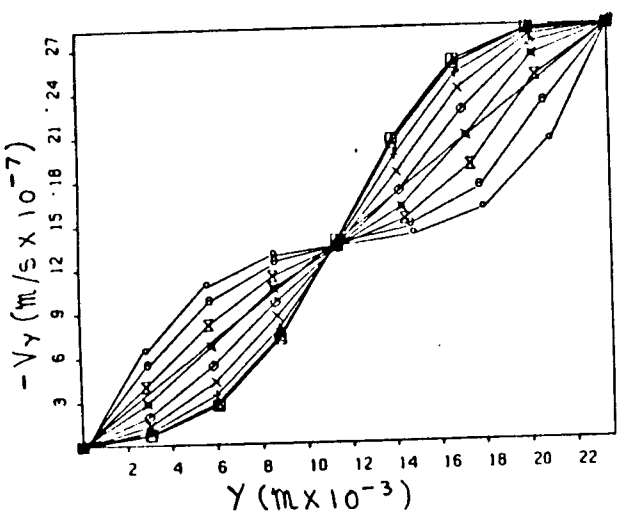

$\varepsilon = 0.217$ $\quad H/D = 2.593$

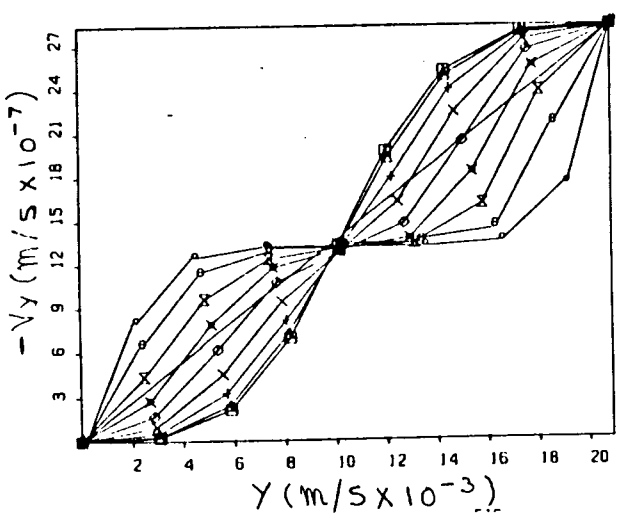

$\varepsilon = 0.341$ $\quad H/D = 2.023$

FIG. 5.3.1.2(a).

GRAPHS OF $-V_y$ AGAINST Y ALONG X GRID LINES FOR CASE 1.

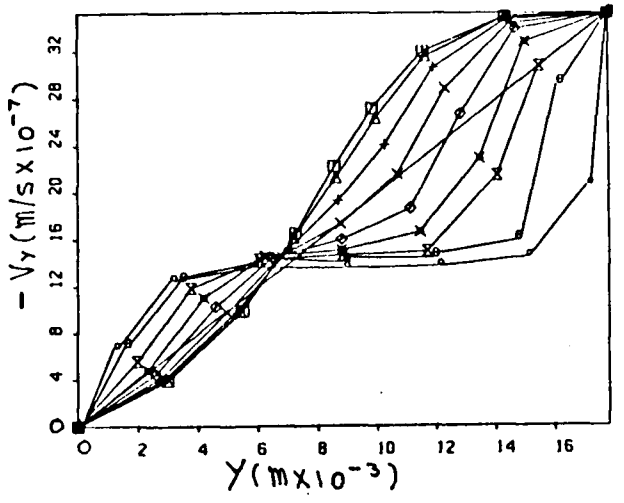

$\varepsilon = 0.512$ $H/D = 1.433$

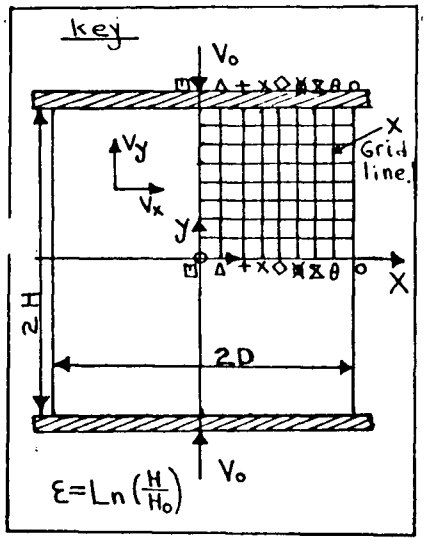

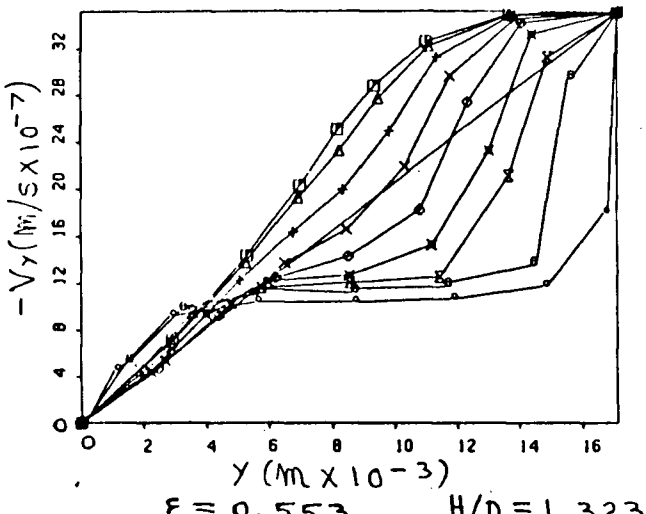

$\varepsilon = 0.553$ $H/D = 1.323$

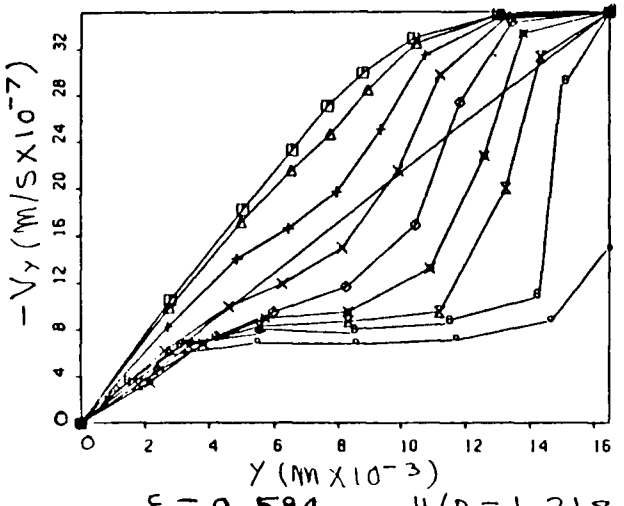

$\varepsilon = 0.594$ $H/D = 1.218$

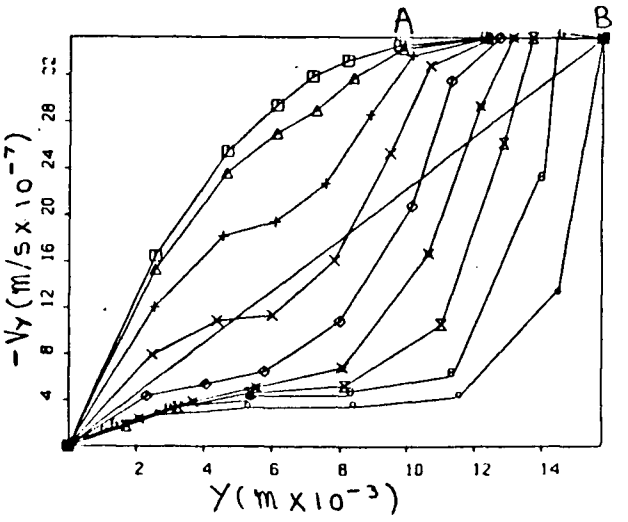

$\varepsilon = 0.639$ $H/D = 1.117$

FIG. 5.3.1.2(b).

FUTHER GRAPHS OF $-V_y$ AGAINST Y ALONG X GRID LINES FOR CASE 1.

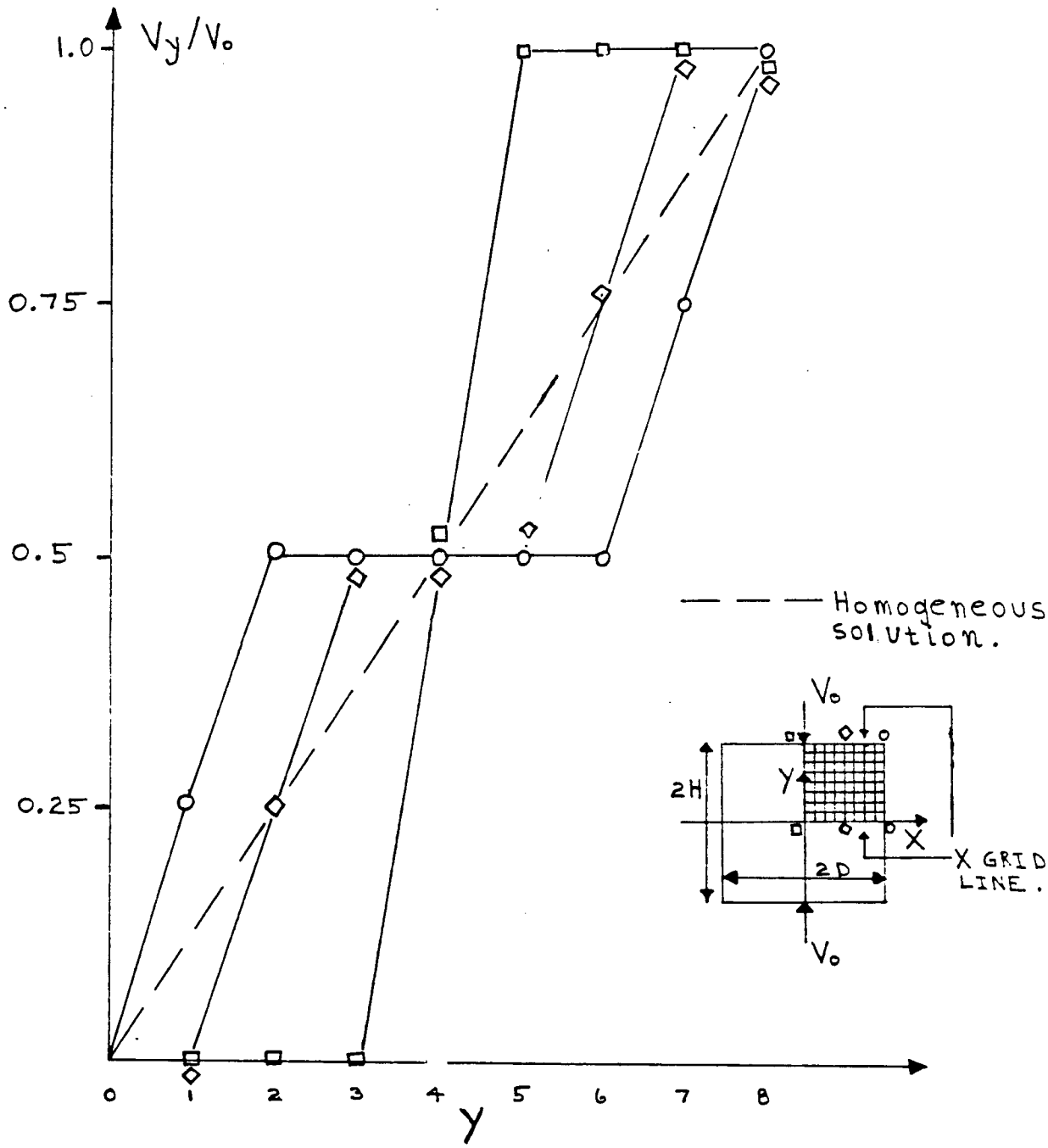

FIG. 5.3.1.3.(a).

GRAPHS OF $-V_y/V_o$ AGAINST Y ALONG X GRID LINES FOR THE UPPER BOUND MODEL FOR CASE 1 AT H/D = 2.023.

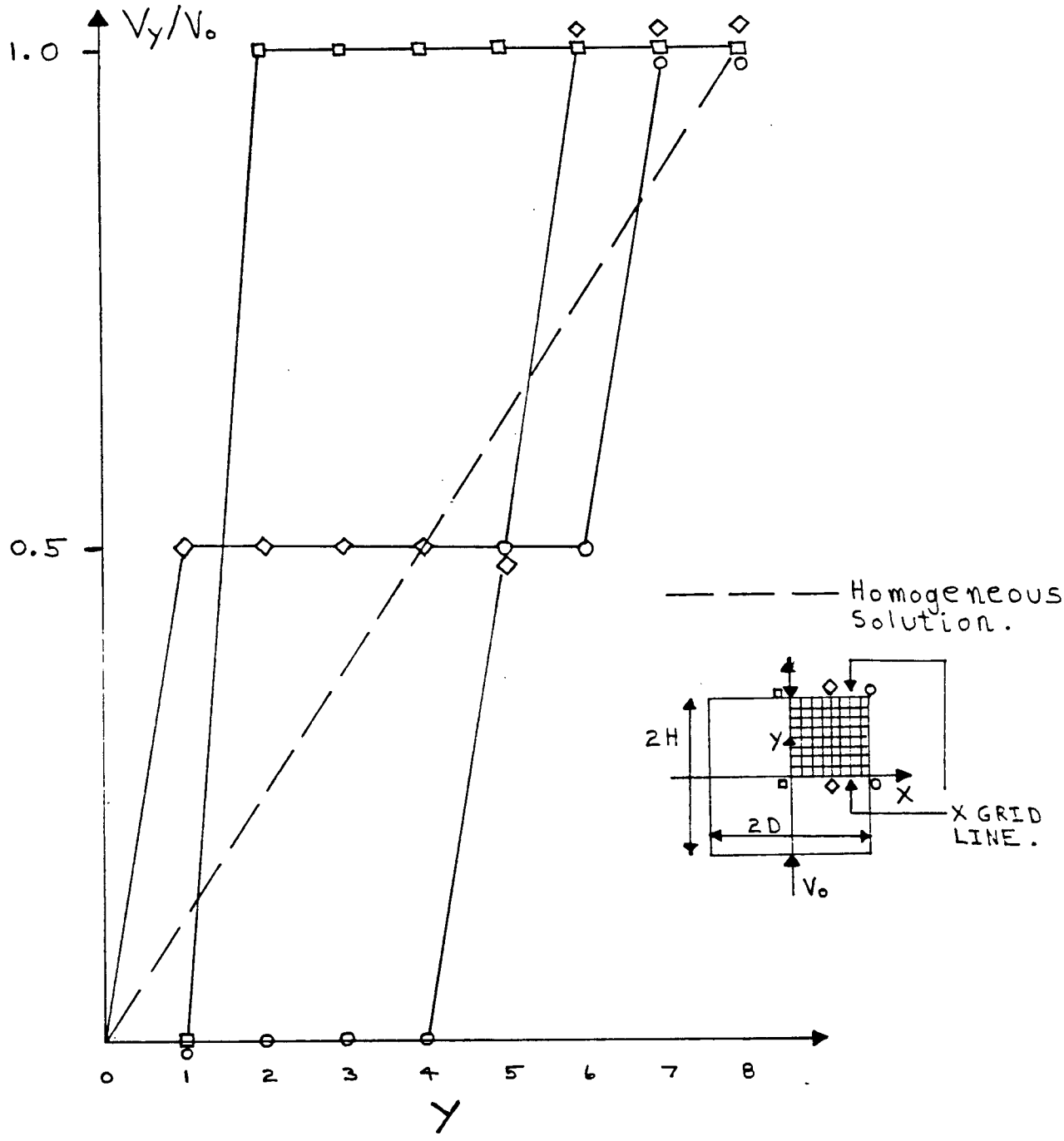

FIG. 5.3.1.3(b).

GRAPHS OF V_y/V_o AGAINST Y ALONG X GRID LINES FOR THE UPPER BOUND MODEL FOR CASE I AT H/D = 1.117.

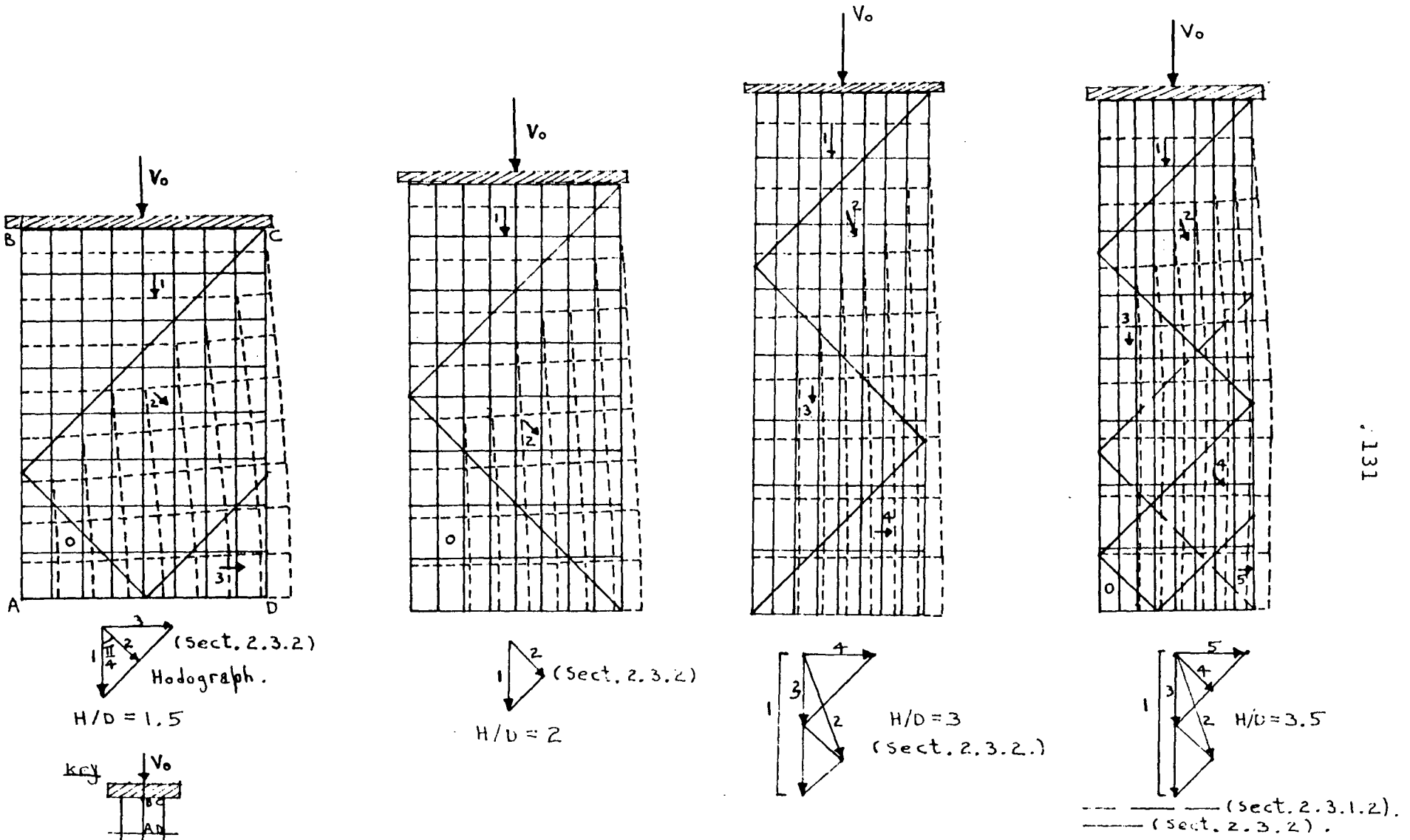

FIG. 5.3.1.4.

FINITE ELEMENT DISPLACED SHAPE PLOTS FOR THE START OF PLANE STRAIN COMPRESSION OF RECTANGULAR BLOCKS OF ALUMINUM. H/D OF 1.5, 2, 3, AND 3.5 ARE SHOWN.

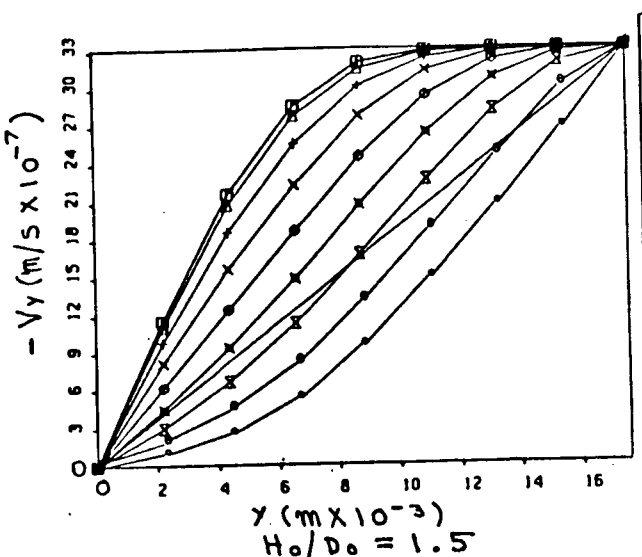

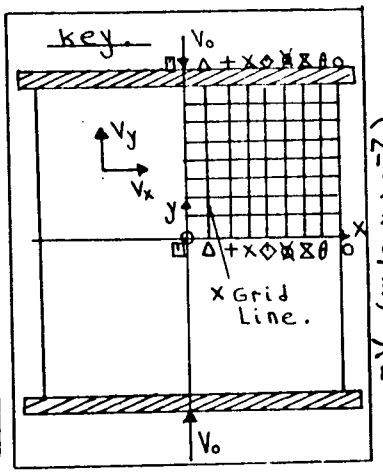

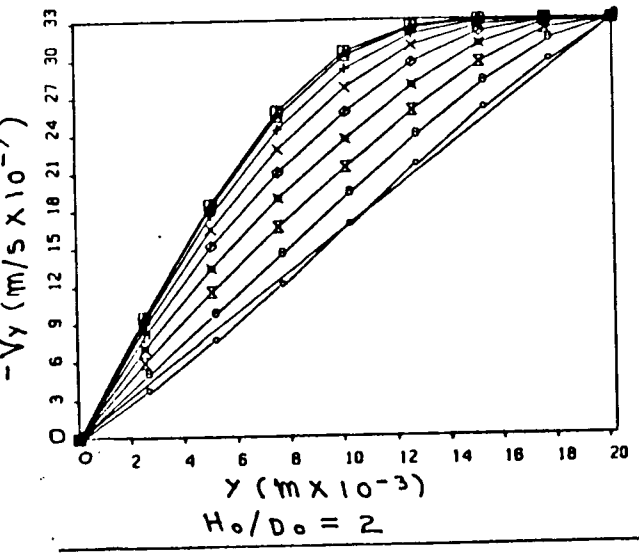

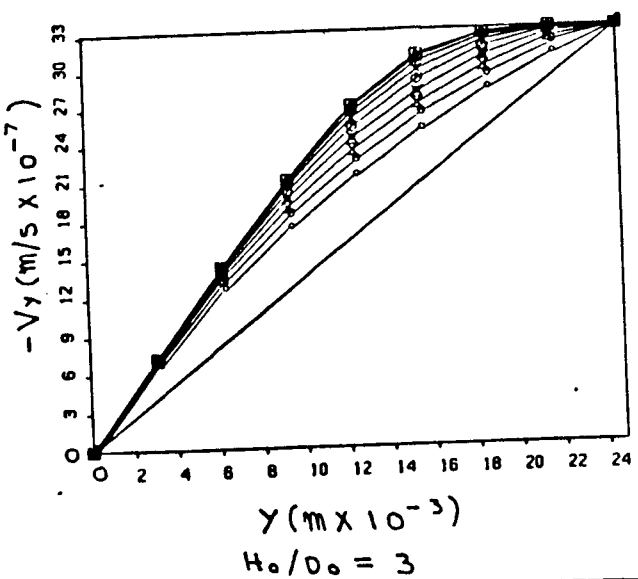

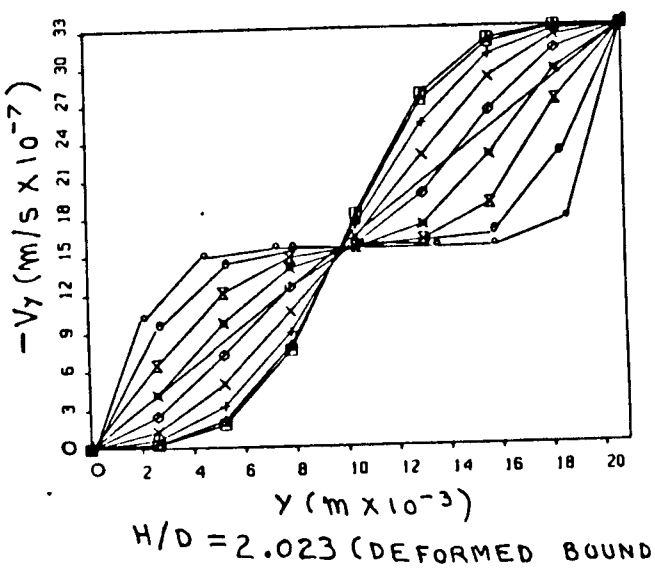

FIG. 5.3.1.5.

GRAPHS OF $-V_y$ AGAINST Y ALONG X GRID LINES FOR VARIOUS H_o/D_o RATIOS (UNDERORMED BLOCKS) AND ONE H/D RATIO FOR A BLOCK WITH A DEFORMED BOUNDARY.

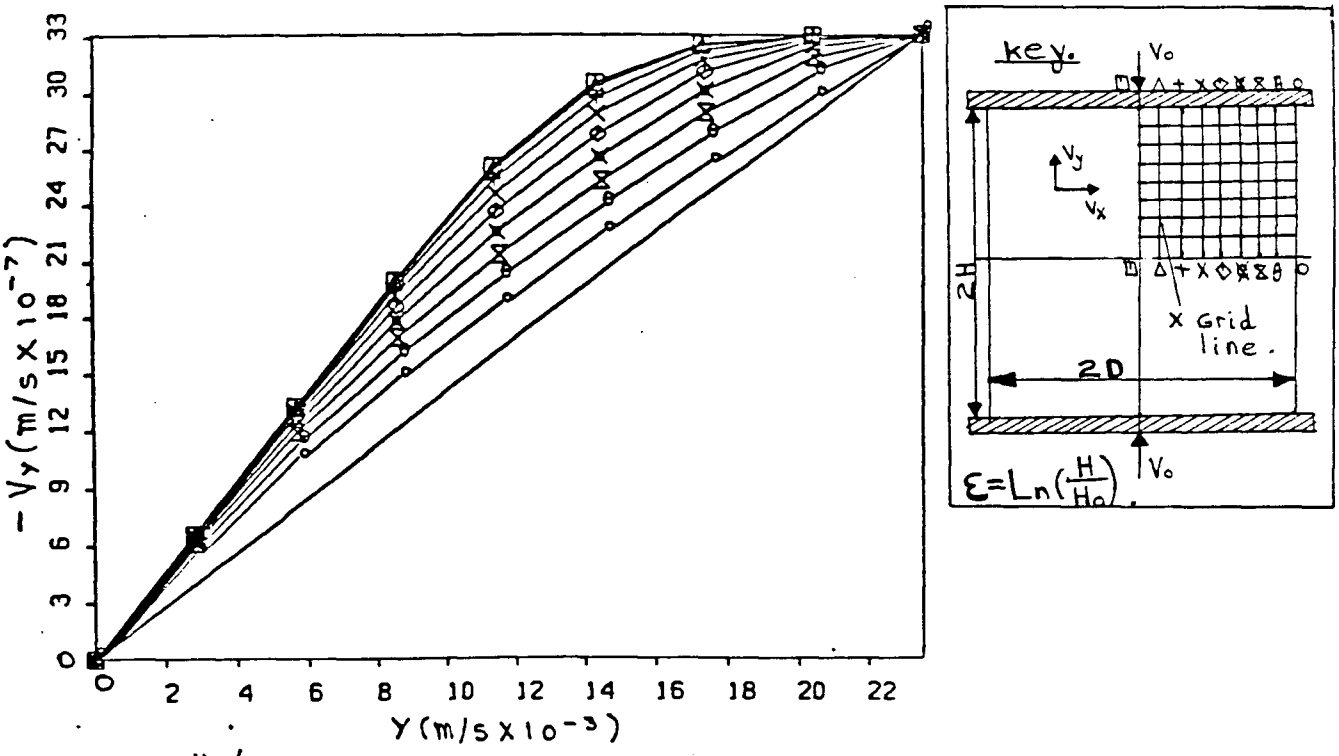

$H_o/D_o = 3$, $\varepsilon = 0.052$

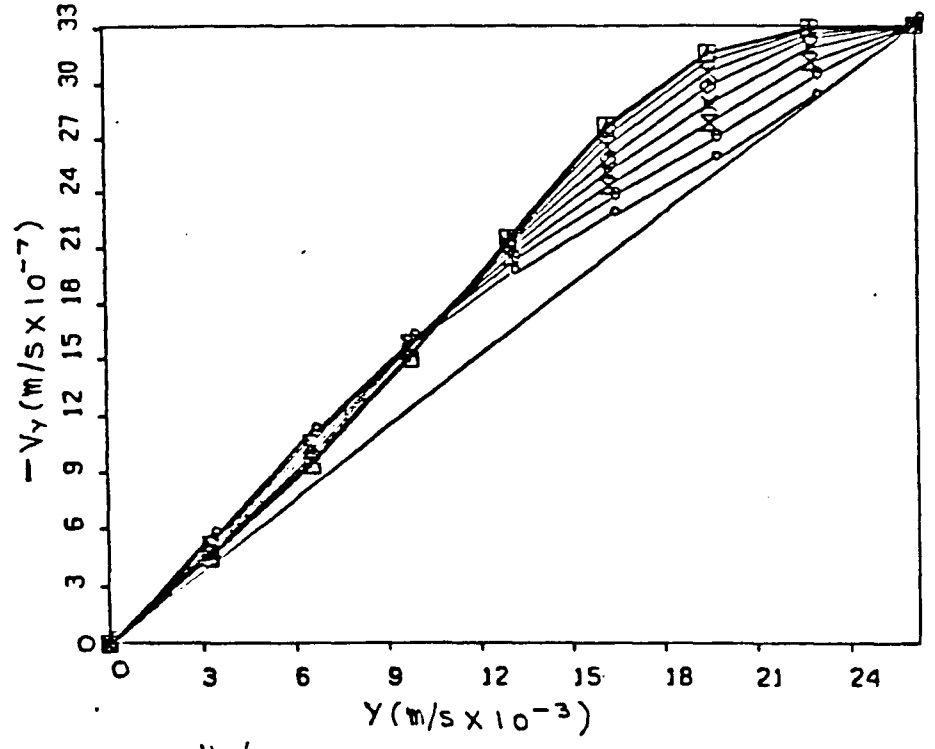

$H_o/D_o = 3.5$ $\varepsilon = 0.024$

FIG. 5.3.1.6.
$-V_y$ AGAINST Y FOR TWO SLIGHTLY STRAINED BLOCKS OF $H_o/D_o = 3$ AND 3.5 .

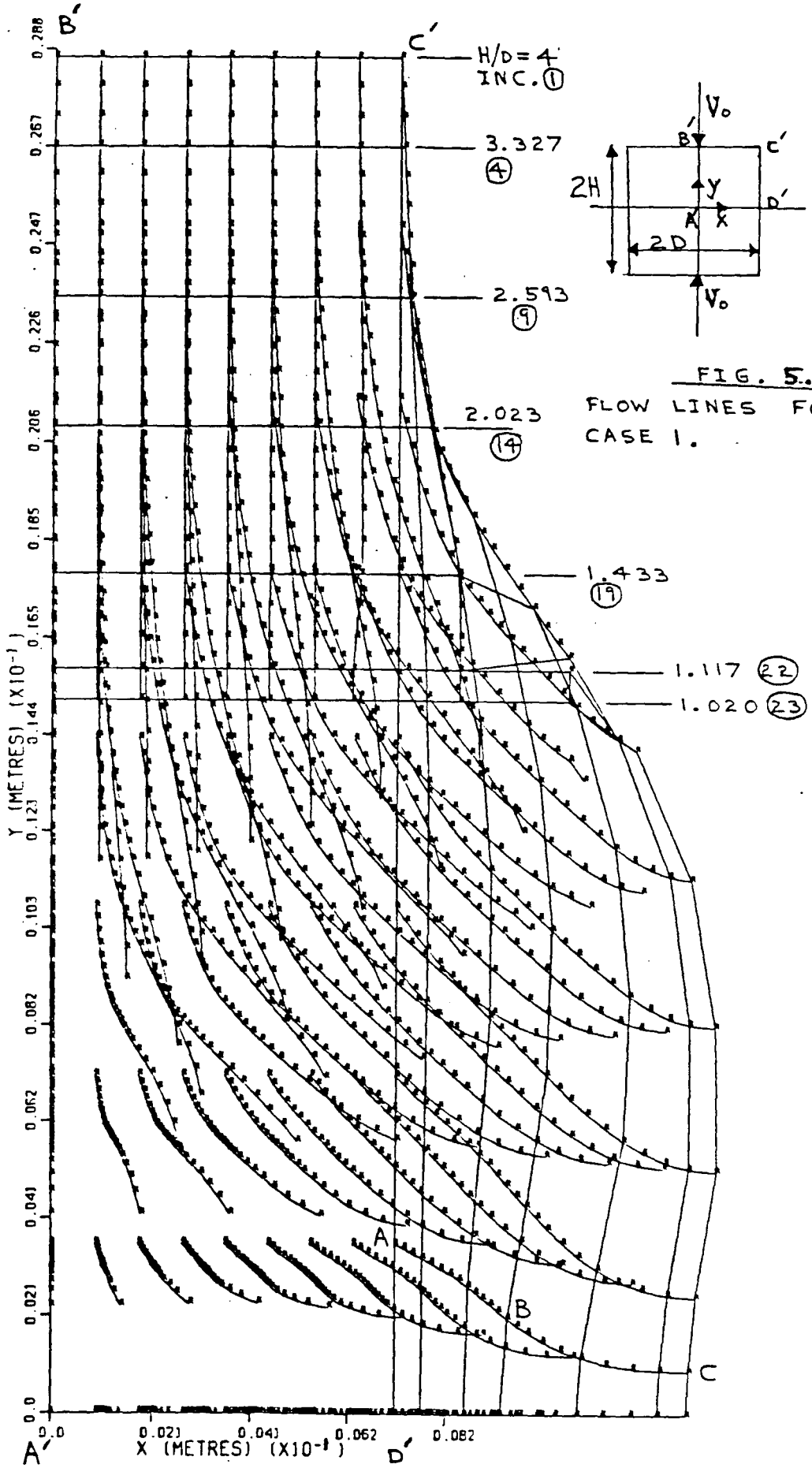

FIG. 5.3.1.7
FLOW LINES FOR CASE 1.

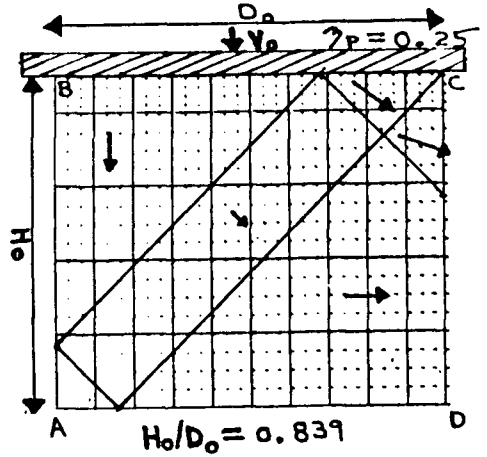

$H_o/D_o = 0.839$

$\varepsilon = 0$

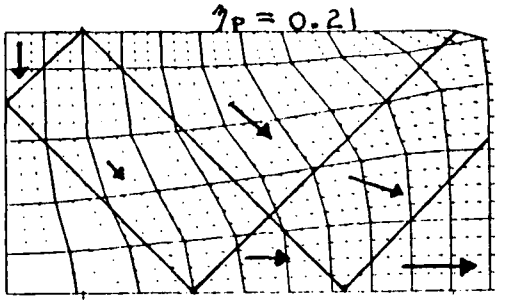

$H/D = 0.523$

$\varepsilon = 0.236$

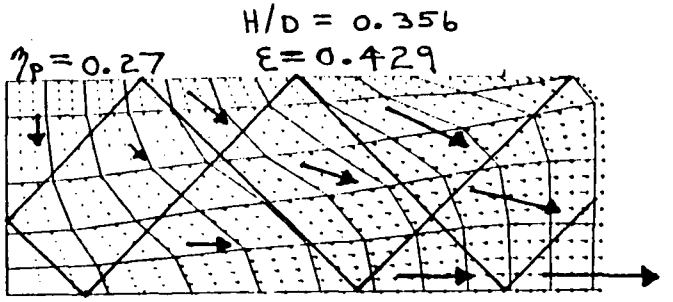

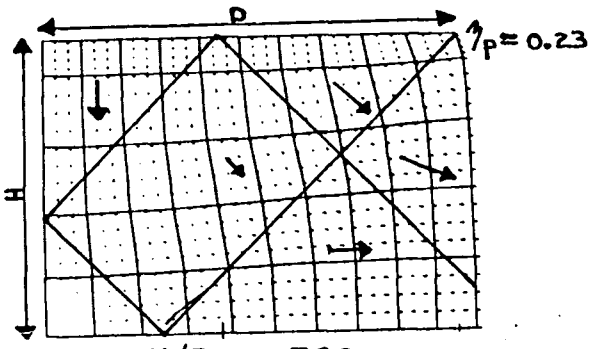

$H/D = 0.700$

$\varepsilon = 0.091$

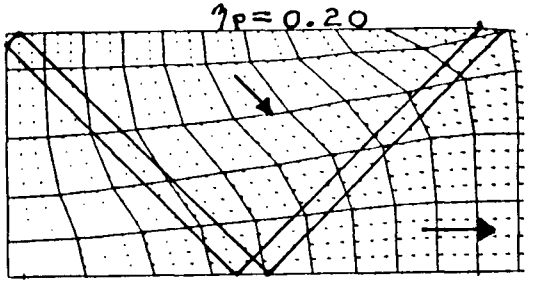

$H/D = 0.475$

$\varepsilon = 0.284$

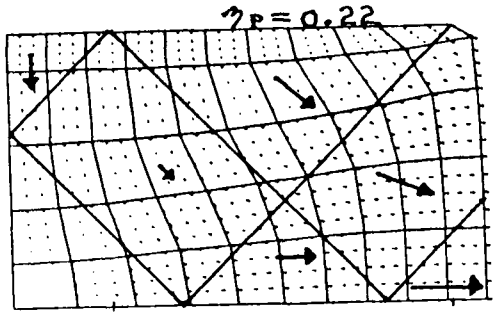

$H/D = 0.574$

$\varepsilon = 0.190$

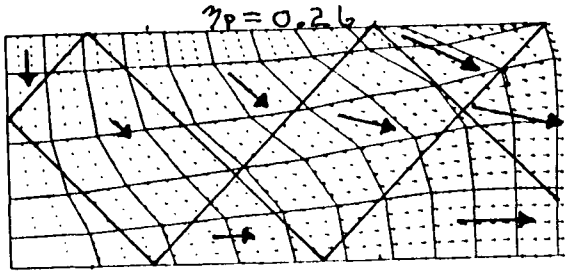

$H/D = 0.408$

$\varepsilon = 0.361$

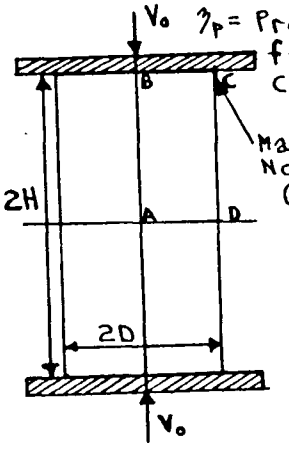

$\varepsilon = \mathrm{Ln}\left(\frac{H}{H_o}\right)$.

FIG. 5.3.2.1

DEFORMED SHAPES FOR THE QUASI-STATIC PLANE STRAIN COMPRESSION OF A RIGID-PERFECTLY PLASTIC MATERIAL BETWEEN RIGID AND PARALLEL PLATENS. THE MASTER-SLAVE NODE METHOD WAS USED FOR PLATEN FRICTION WITH $\beta = 0.675$.

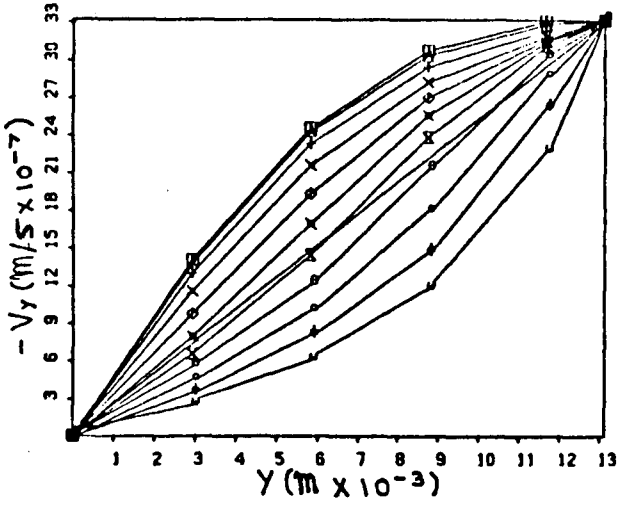

ε=0.022 H/D=0.803

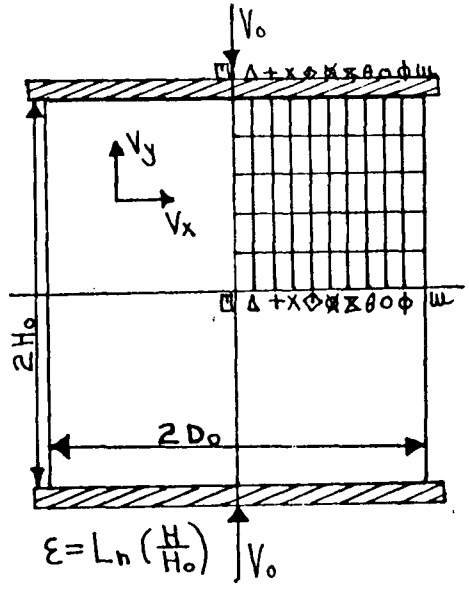

$\varepsilon = Ln\left(\frac{H}{H_0}\right)$

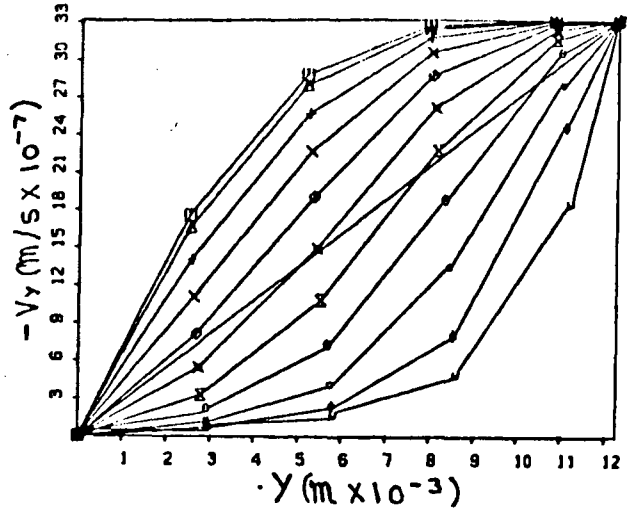

ε=0.091 H/D=0.700

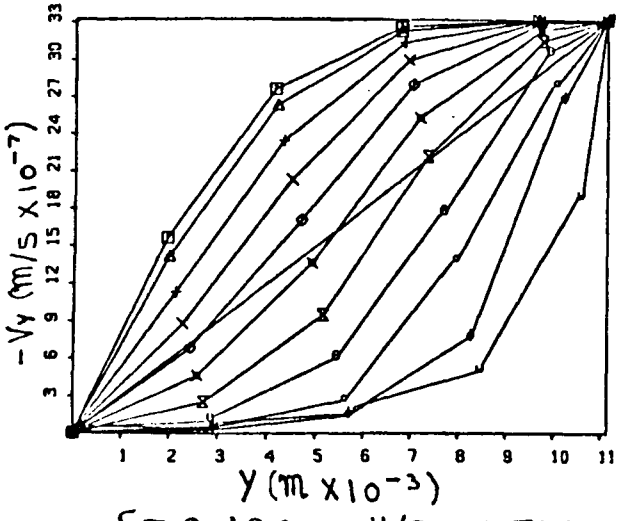

ε=0.190 H/D=0.574

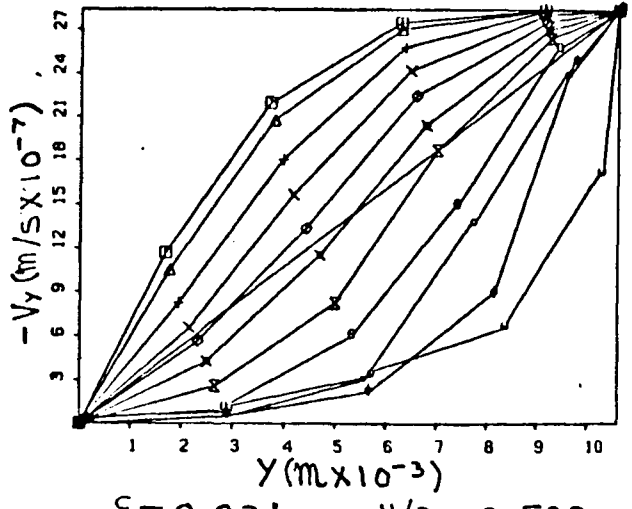

ε=0.236 H/D=0.523

FIG. 5.3.2.2

GRAPHS OF -Vy AGAINST Y ALONG X GRID LINES FOR CASE 2.

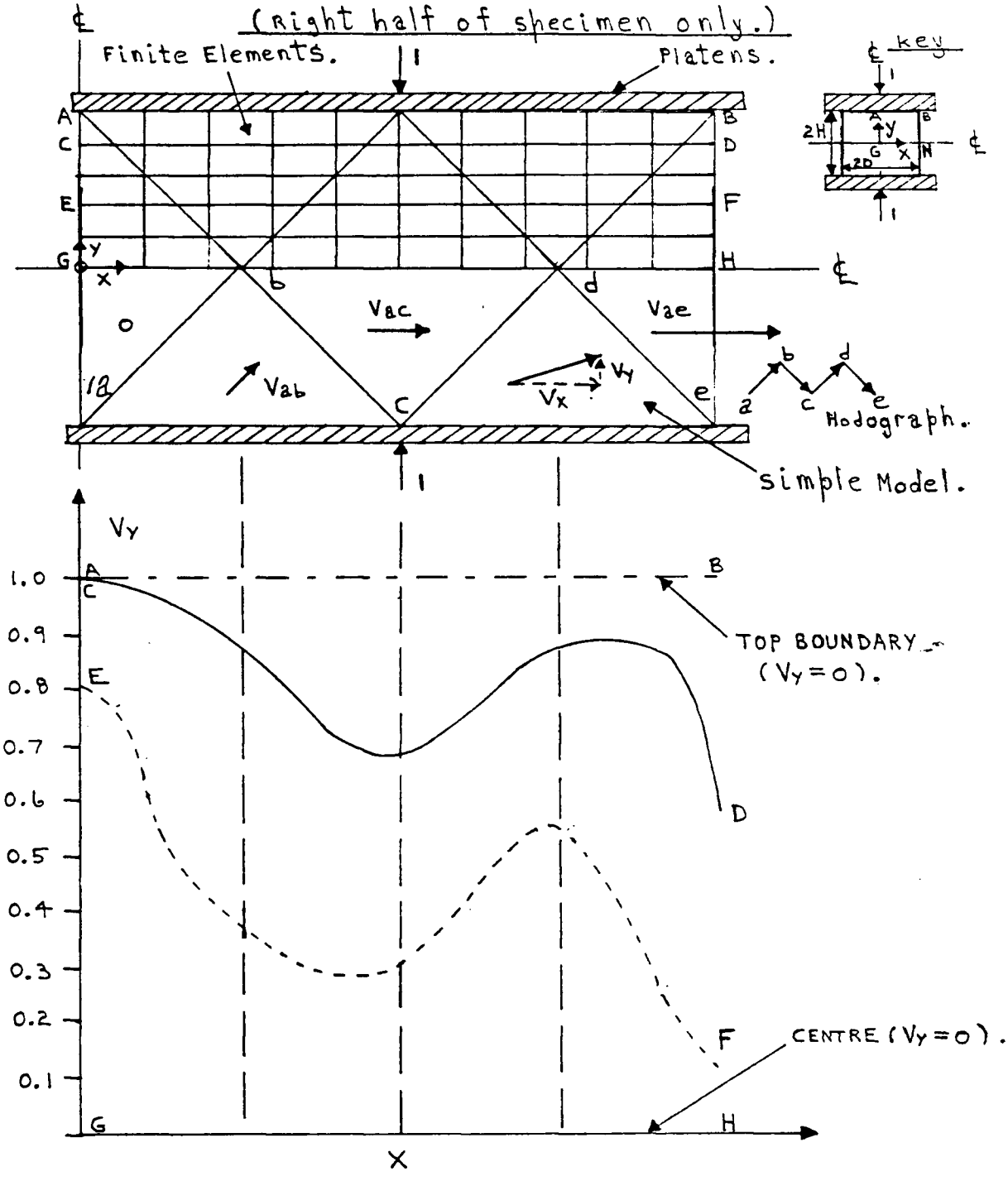

FIG. 5.3.2.3.
A COMPARISON OF V_Y AGAINST X FROM THE FINITE ELEMENT CALCULATIONS WITH THE SIMPLE MODEL PREDICTIONS FOR THE CASE H/D = 0.25 .

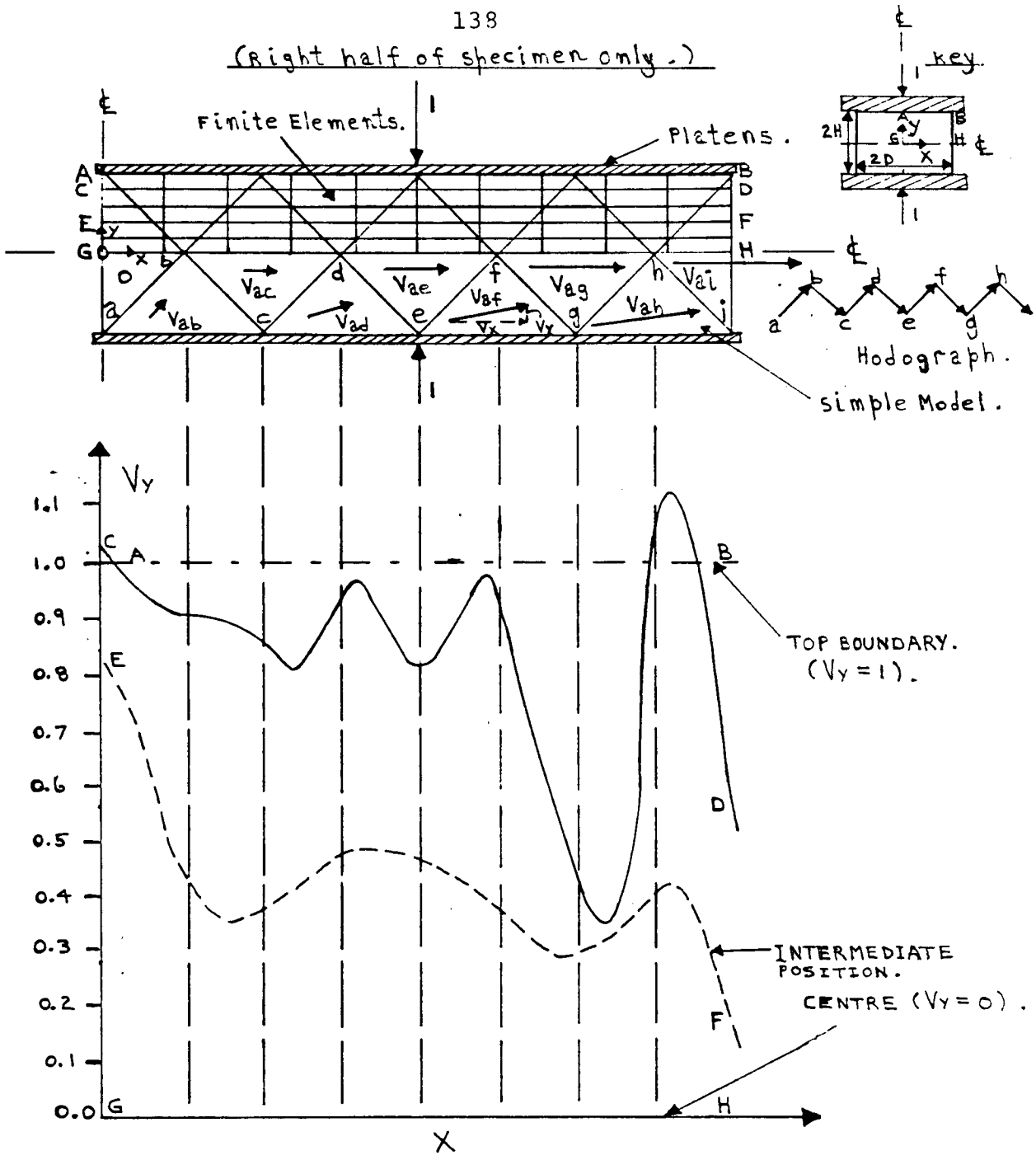

FIG. 5.3.2.4

A COMPARISON OF V_y AGAINST X FROM THE FINITE ELEMENT CALCULATIONS WITH THE SIMPLE MODEL PREDICTIONS FOR THE CASE H/D=0.125.

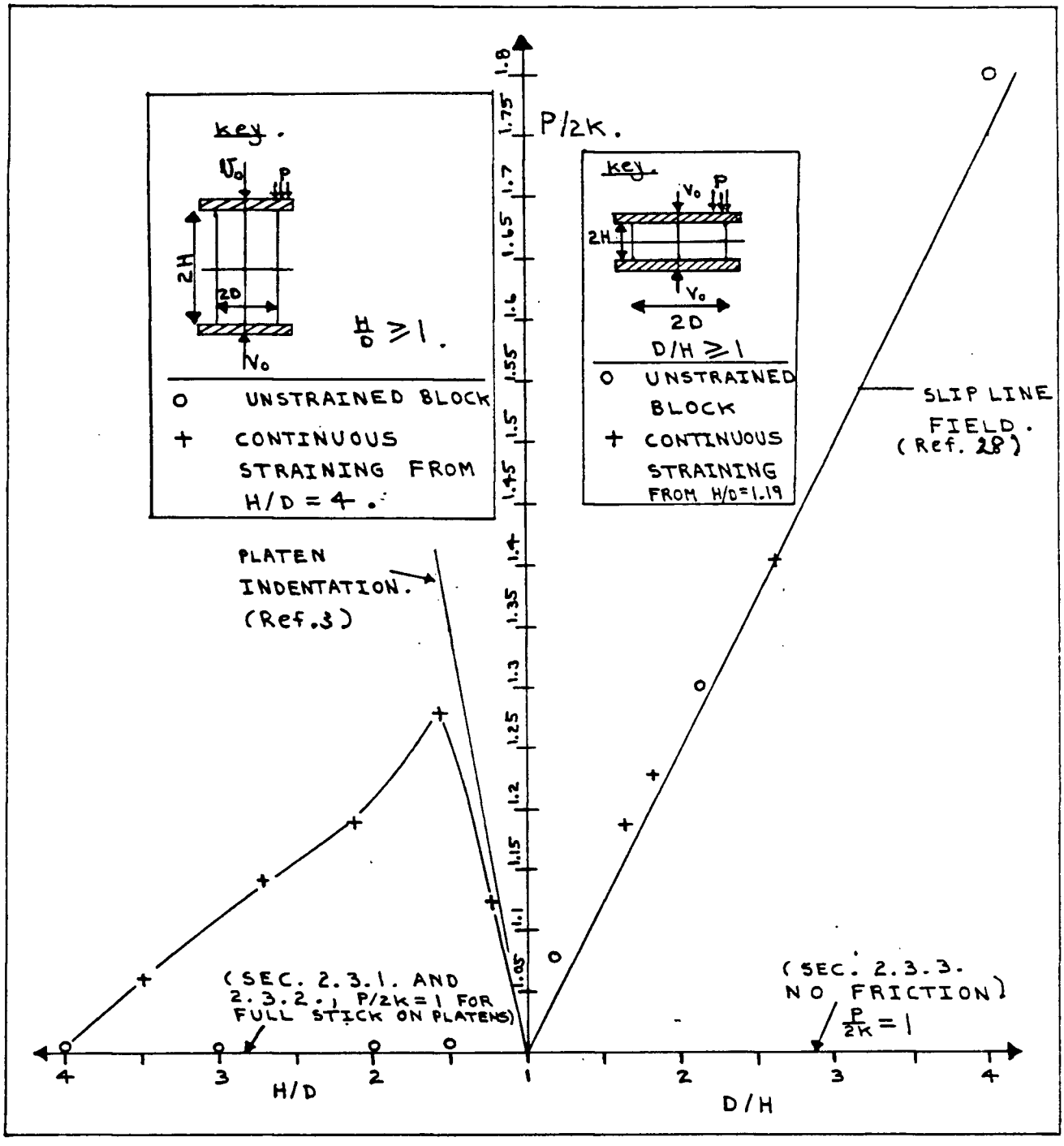

FIG. 5.3.3.1.

A COMPARISON OF NORMAL PLATEN TRACTION FROM THE FINITE ELEMENT CALCULATIONS FOR A RIGID-PERFECTLY PLASIC MATERIAL WITH THE PREDICTIONS OF APPROXIMATE CLOSED FORM SOLUTIONS.

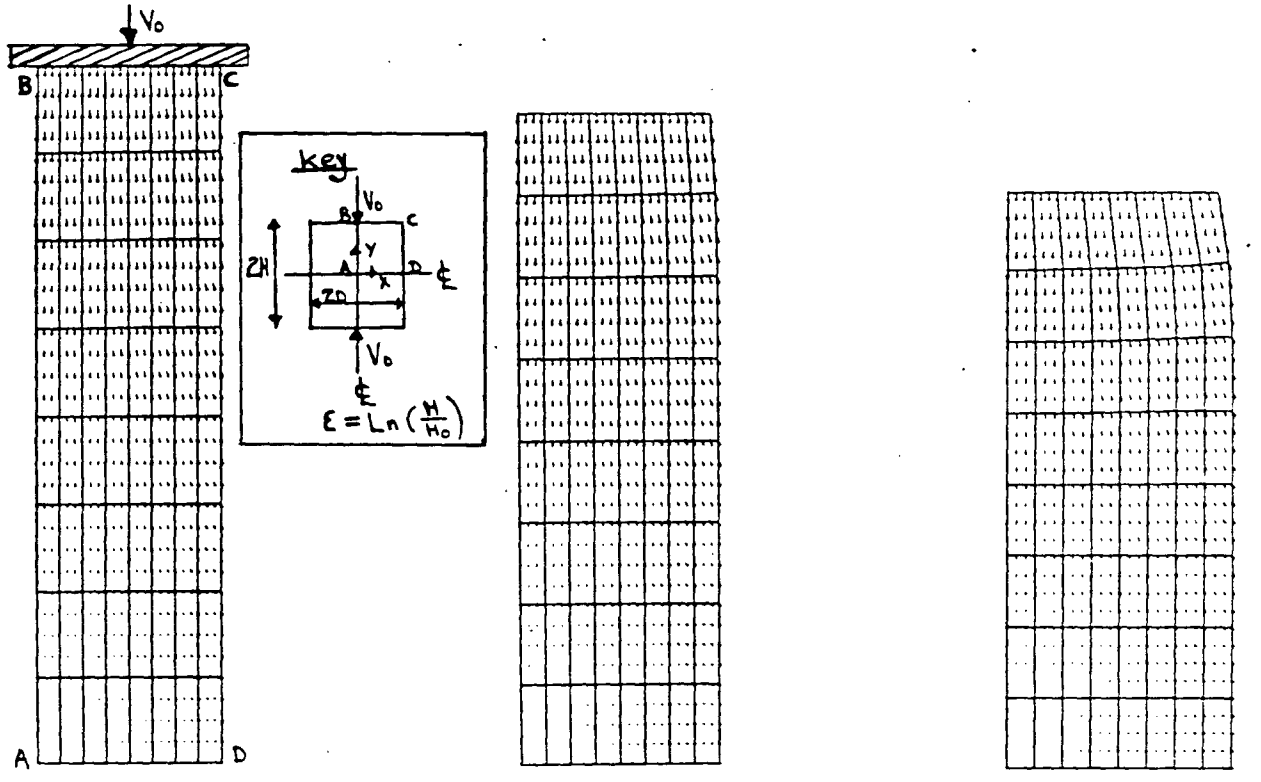

FIG. 5.4.1.1

DEFORMED SHAPES WITH VELOCITY VECTOR PLOTS AT VARIOUS STAGES OF COMPRESSION FROM $H_o/D_o = 4$ FOR PLASTICINE.

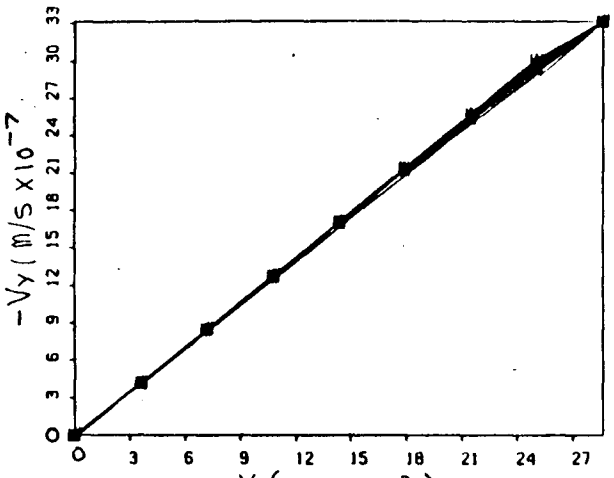

$\varepsilon = 0.022$ $\quad H/D = 3.826$

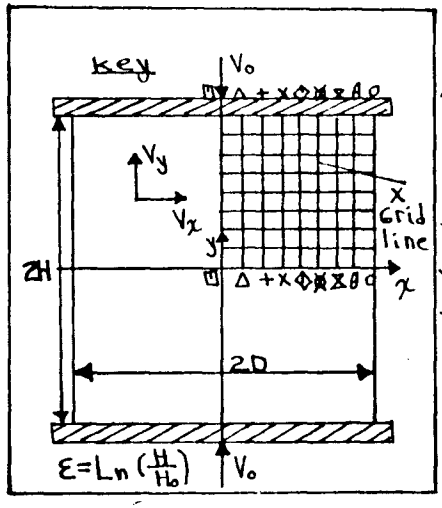

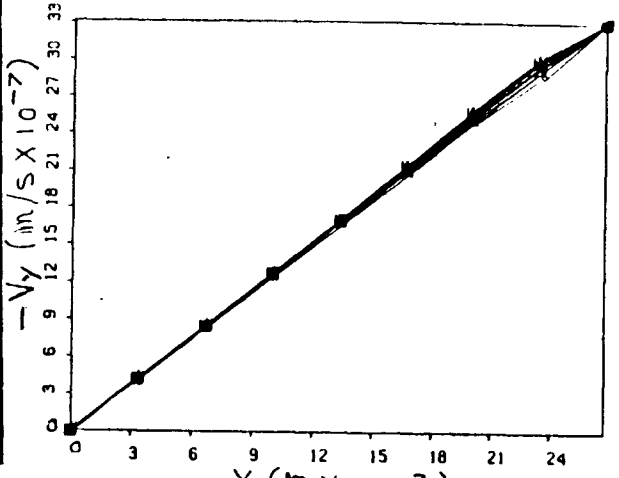

$\varepsilon = 0.092$ $\quad H/D = 3.327$

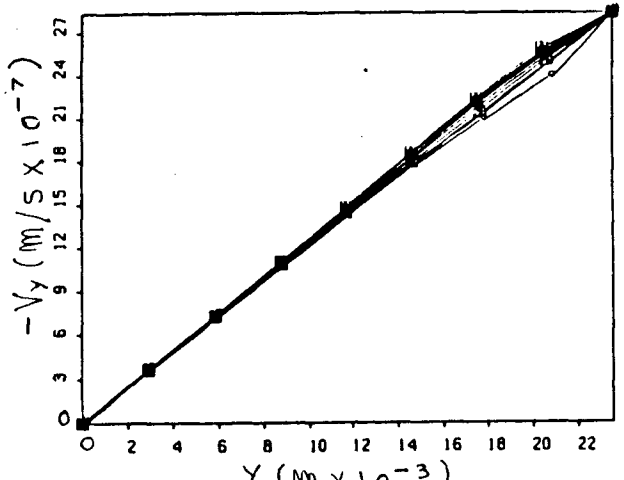

$\varepsilon = 0.217$ $\quad H/D = 2.593$

FIG. 5.4.1.2.

GRAPHS OF $-V_y$ AGAINST Y ALONG X GRID LINES FOR PLASTICINE.

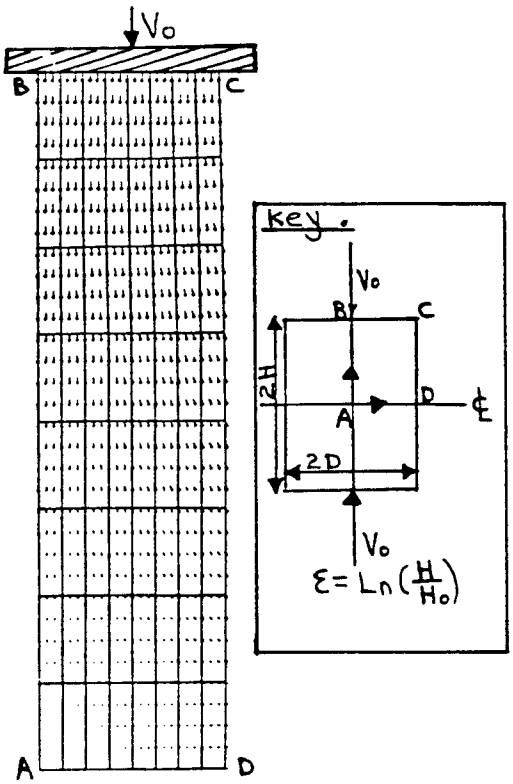

ε = 0.022
H/D = 3.826

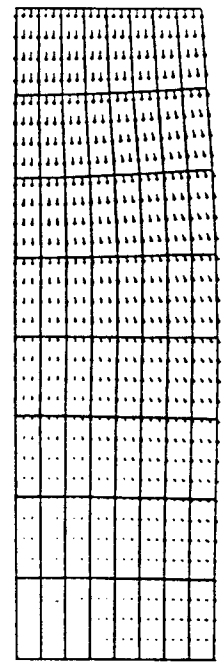

ε = 0.092
H/D = 3.327

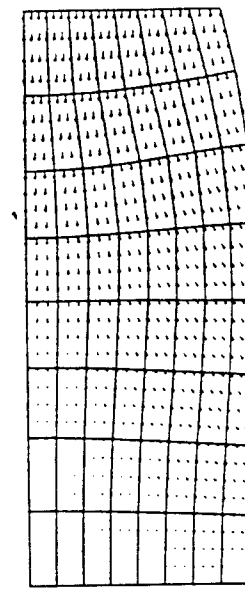

ε = 0.217
H/D = 2.593

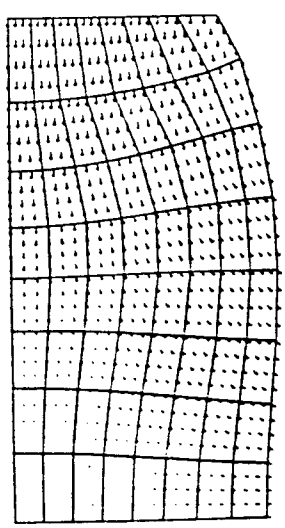

ε = 0.341
H/D = 2.023

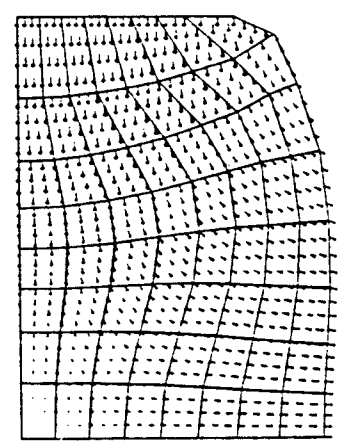

ε = 0.512
H/D = 1.433

FIG.5.4.2.1.

DEFORMED SHAPES WITH VELOCITY VECTOR PLOTS AT VARIOUS STAGES OF COMPRESSION FROM $H_o/D_o = 4$ FOR ALUMINUM.

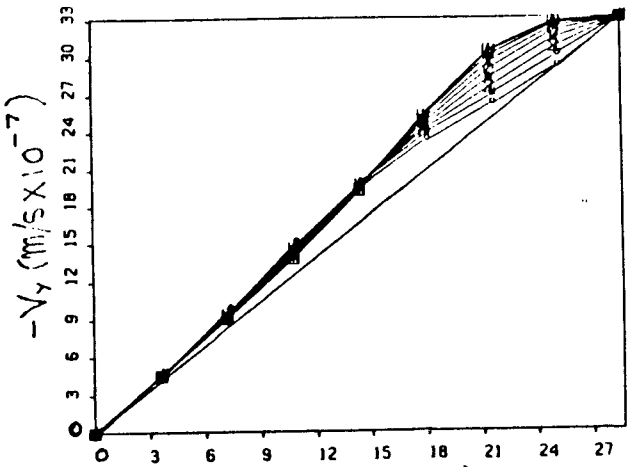

$\varepsilon = 0.022$ $H/D = 3.826$

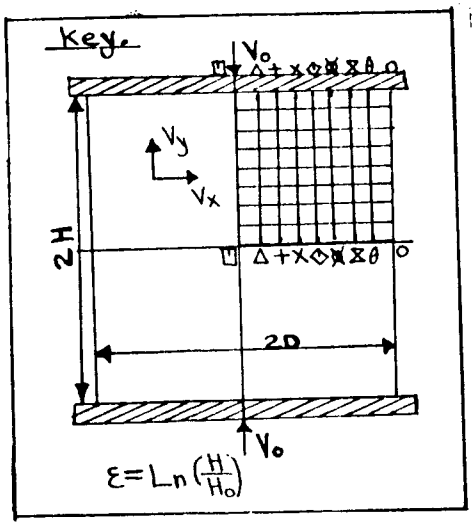

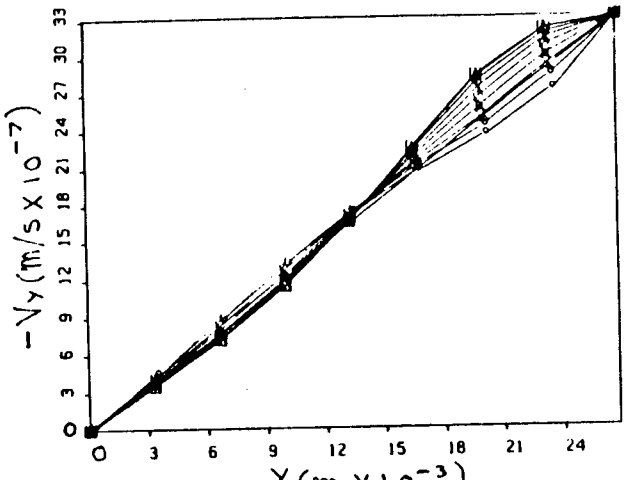

$\varepsilon = 0.092$ $H/D = 3.327$

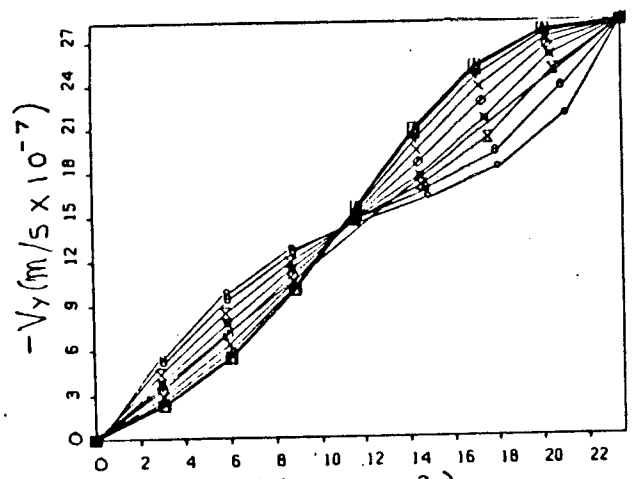

$\varepsilon = 0.217$ $H/D = 2.593$

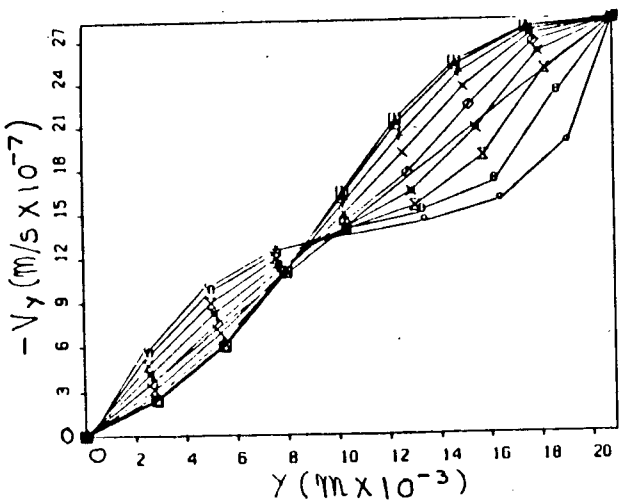

$\varepsilon = 0.341$ $H/D = 2.023$

FIG. 5.4.2.2.

GRAPHS OF $-V_y$ AGAINST Y ALONG X GRID LINES FOR ALUMINUM.

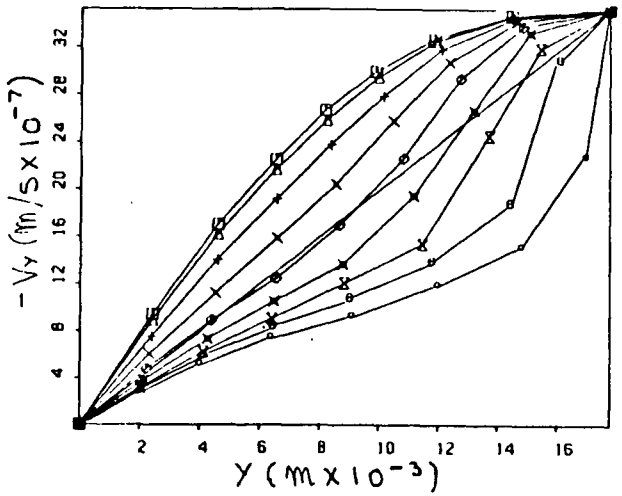

$\varepsilon = 0.512$ $\quad H/D = 1.433$

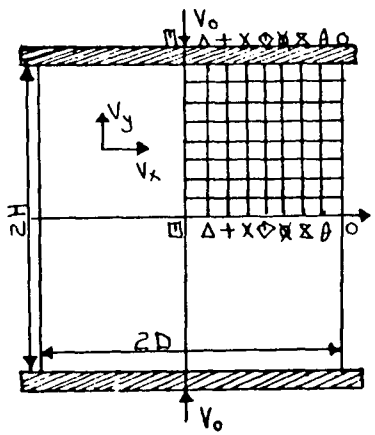

FIG . 5.4.2.3.

A FUTHER GRAPH OF $-V_Y$ AGAINST Y ALONG X GRID LINES FOR ALUMINUM.

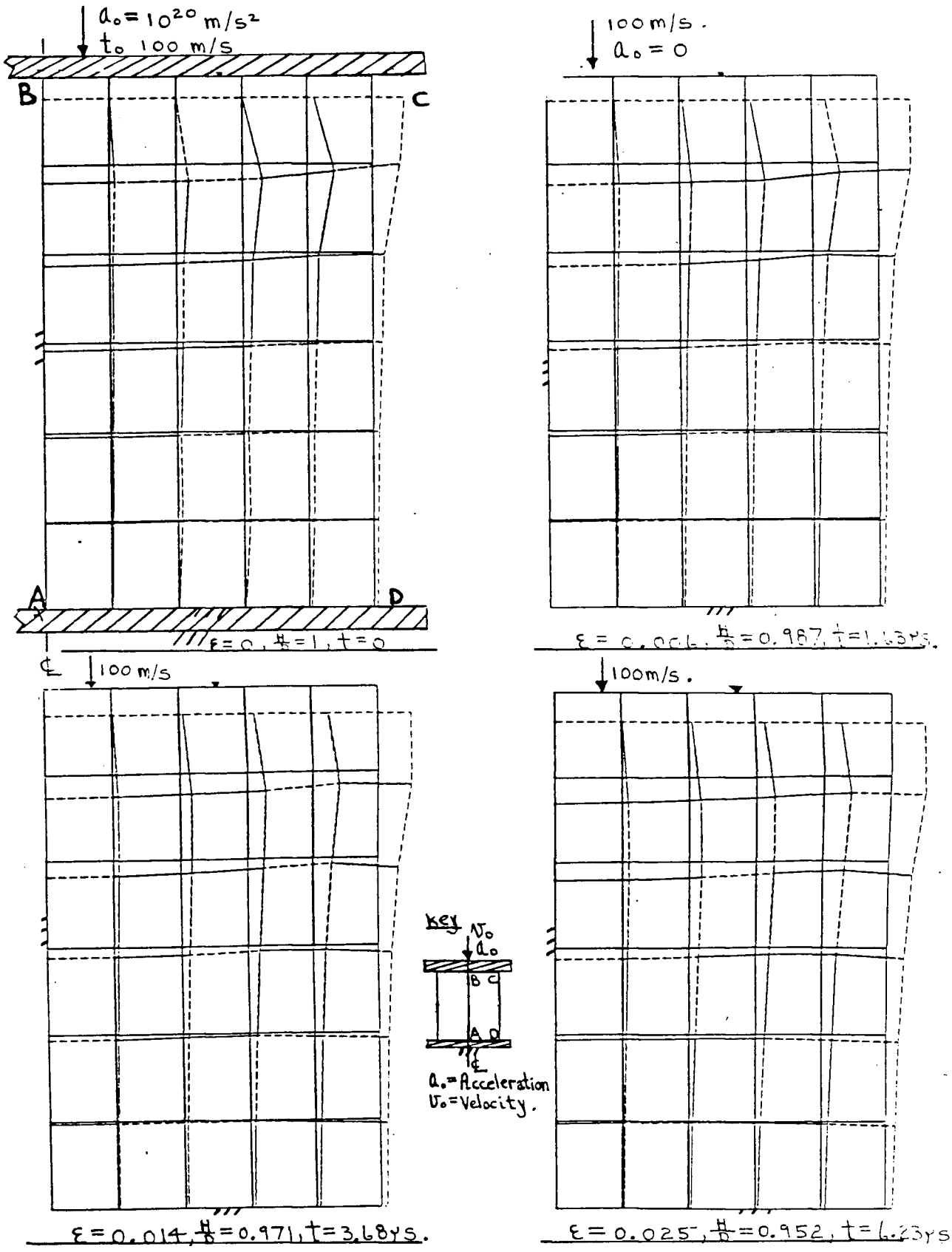

FIG. 5.5.1.

DISPLACED SHAPE PLOTS FOR THE DYNAMIC COMPRESSION OF ALUMINUM AT 100 m/s.

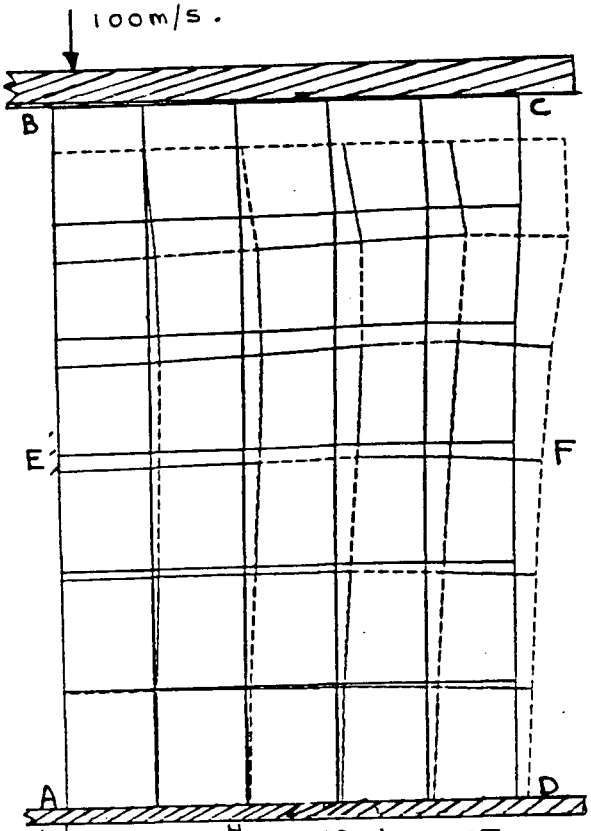

$\varepsilon = 0.038$, $\frac{H}{D} = 0.928$, $t = 9.27$ μs.

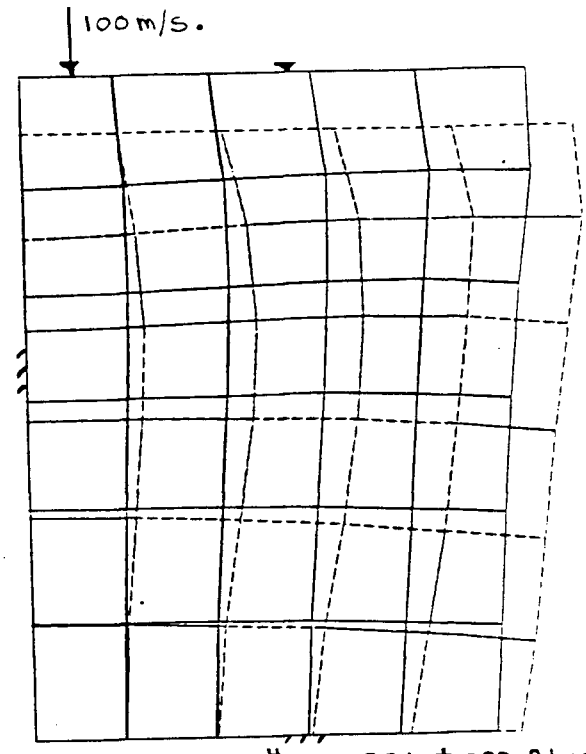

$\varepsilon = 0.099$, $\frac{H}{D} = 0.821$, $t = 23.91$ μs.

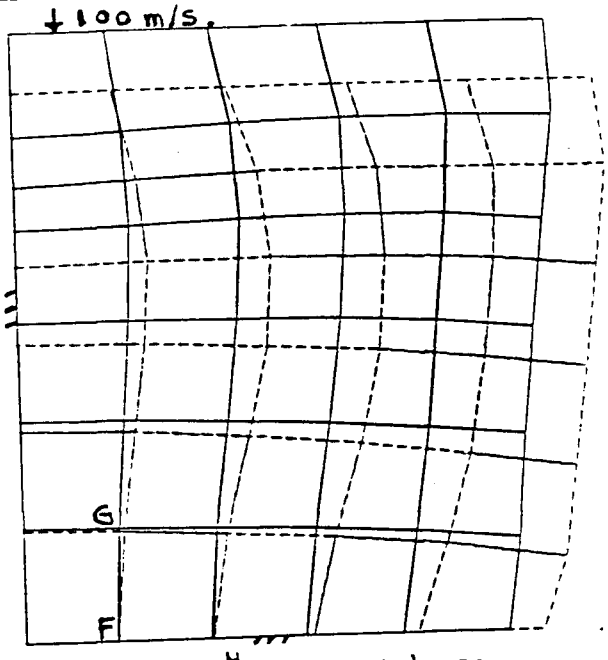

$\varepsilon = 0.160$, $\frac{H}{D} = 0.725$, $t = 37.69$ μs.

FREE (V_o not specified)

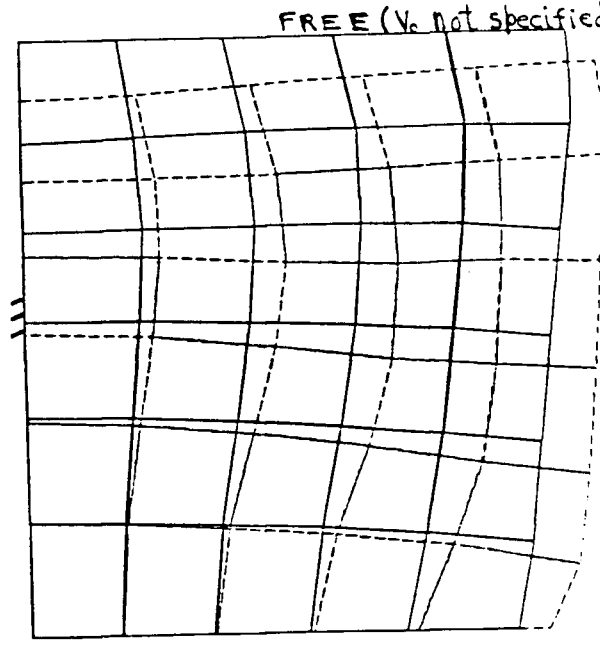

$\varepsilon = 0.189$, $t = 45.11$ μs

FIG. 5.5.2.

DISPLACED SHAPE PLOTS CONTINUED FOR THE DYNAMIC COMPRESSION OF ALUMINUM AT 100 m/s.

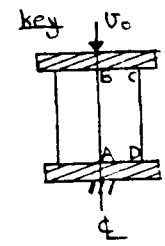

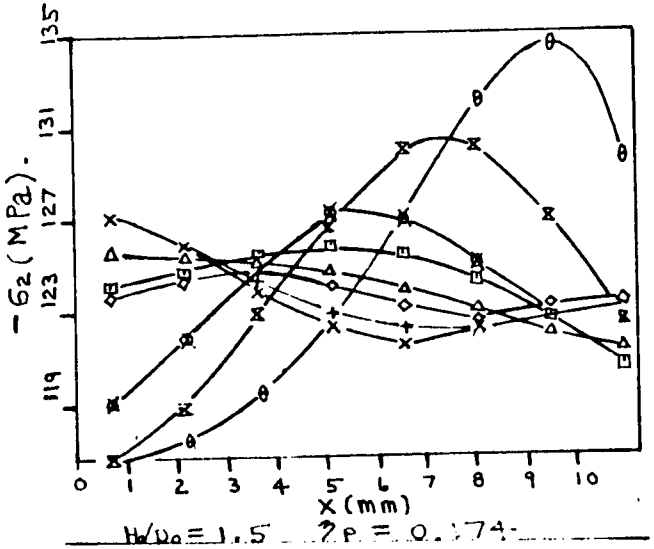

$H_o/D_o = 1.5$ $\eta_p = 0.174$

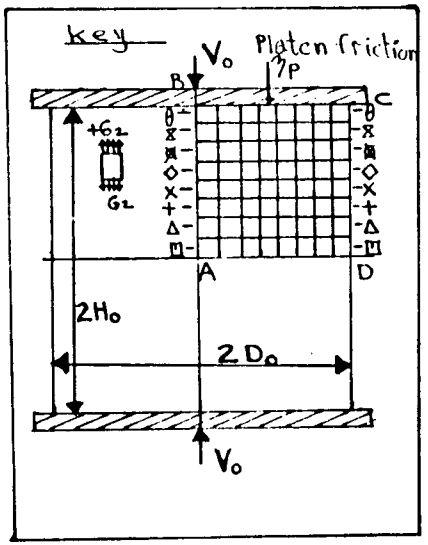

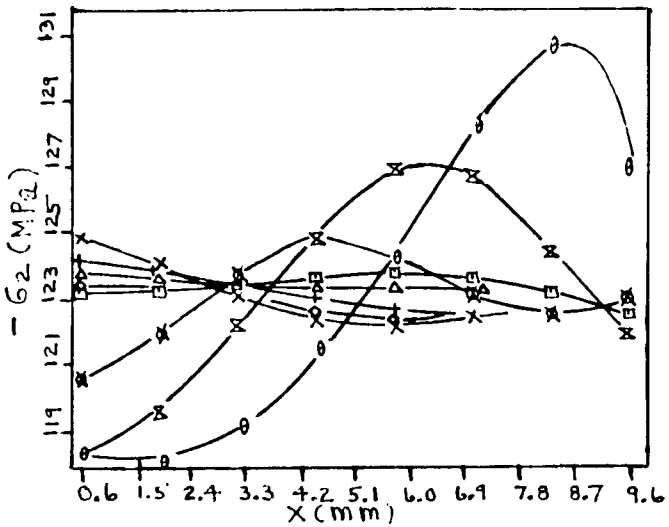

$H_o/D_o = 2.$ $\eta_p = 0.174$

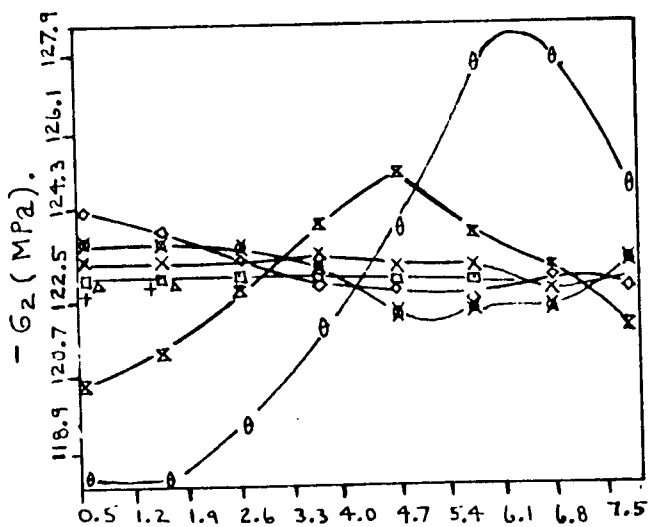

$H_o/D_o = 3$ $\eta_p = 0.174$

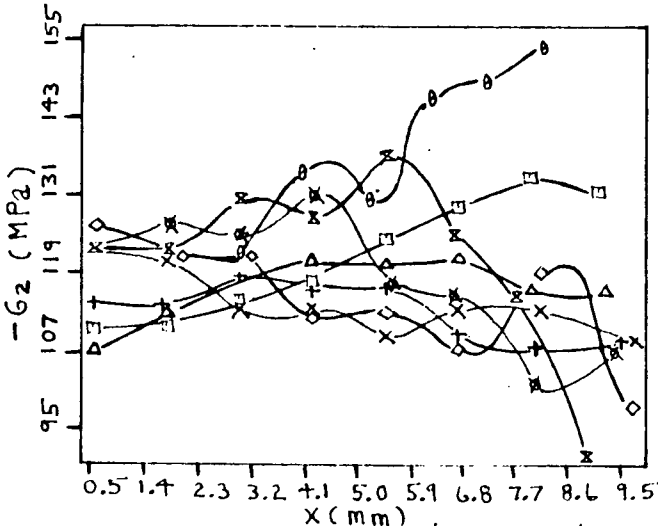

$H_o/D_o = 2.023$ (Boundary CD distorted.)
$\eta_p = 0.174$

147

FIG. 5.6.1.1.

GRAPHS OF G_2 (ELEMENT AVERAGES) AGAINST X FOR HORIZONTAL ROWS OF ELEMENTS ON UNSTRAINED BLOCKS OF ALUMINUM. A PLATEN FRICTION COEFFICIENT OF 0.174 WAS USED IN EACH CASE.

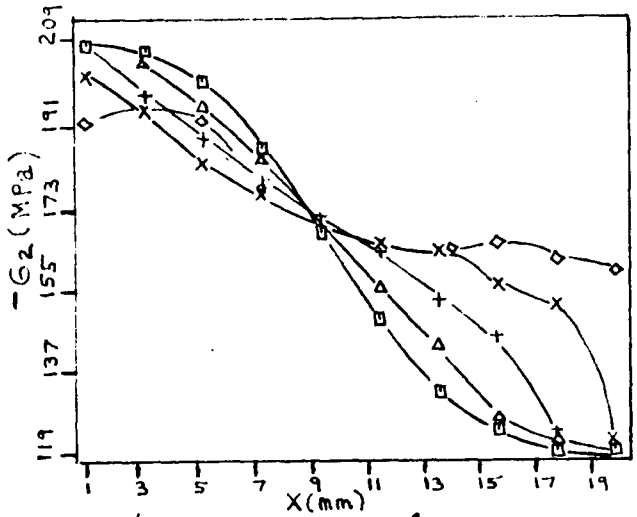

$H_o/D_o = 0.463$ $\eta_P = 0.358$.

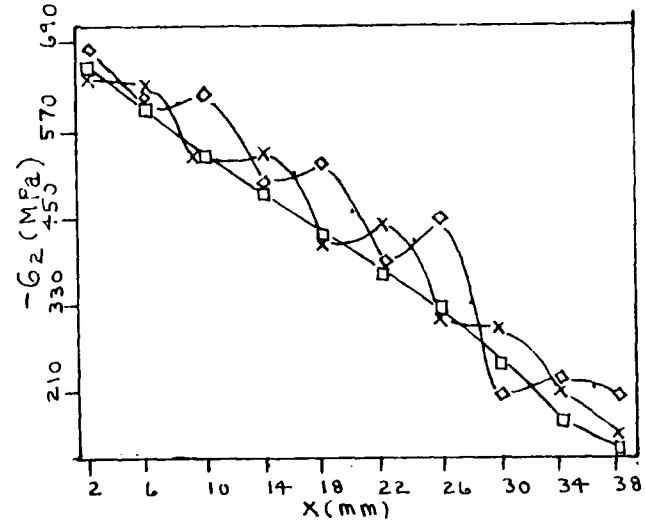

$H_o/D_o = 0.125$ $\eta_P = 0.469$.

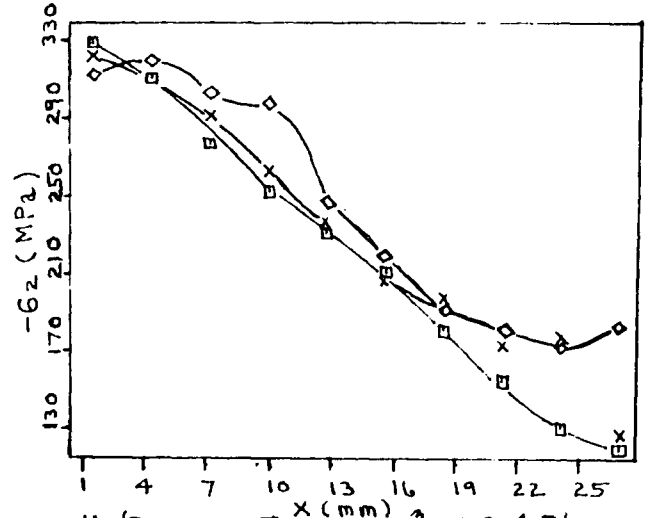

$H_o/D_o = 0.25$ $\eta_P = 0.426$.

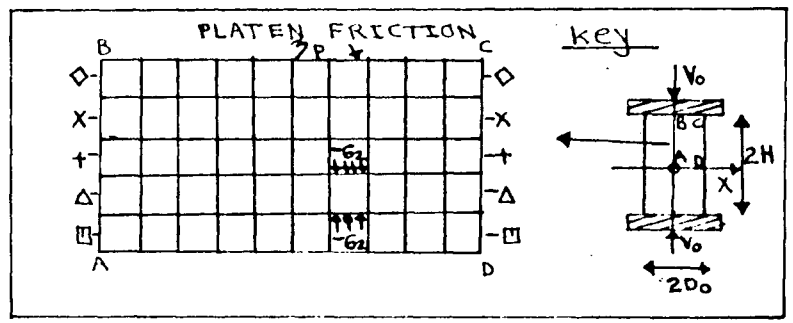

FIG. 5.6.1.2.

G_{2c} (ELEMENT AVERAGE) AGAINST X FOR THREE VALUES OF H_o/D_o FOR UNSTRAINED BLOCKS OF ALUMINUM. THE MASTER-SLAVE NODE METHOD WAS USED IN EACH CASE WITH $\beta = 0.675$

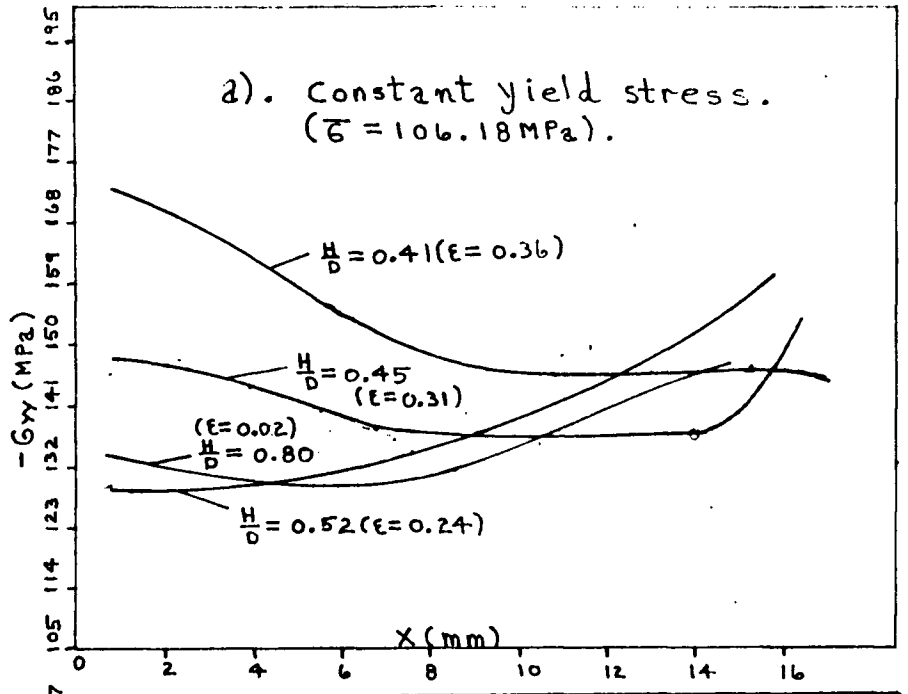

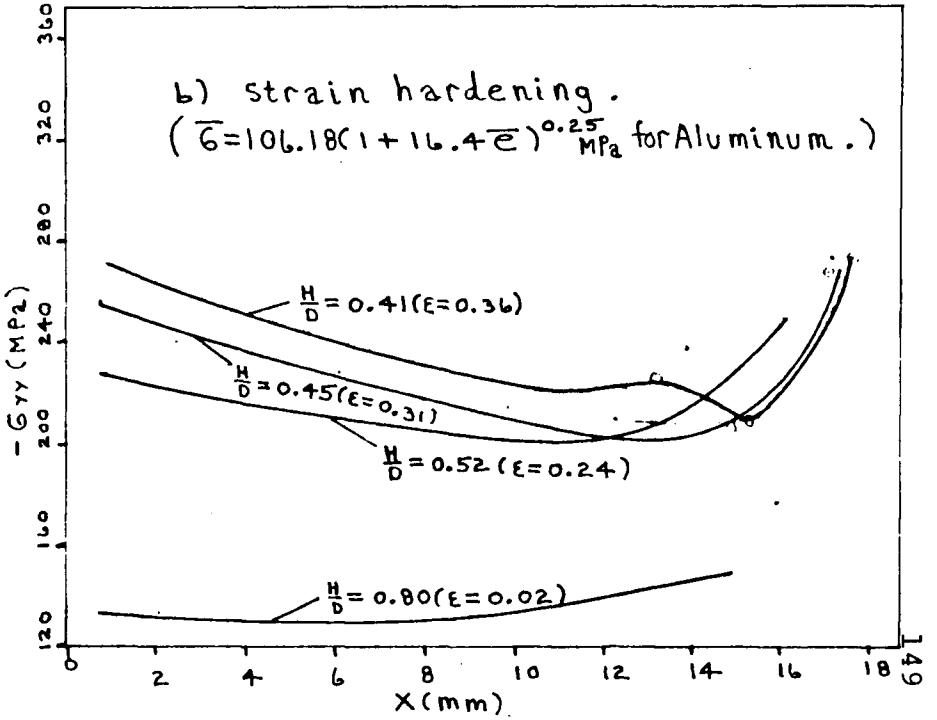

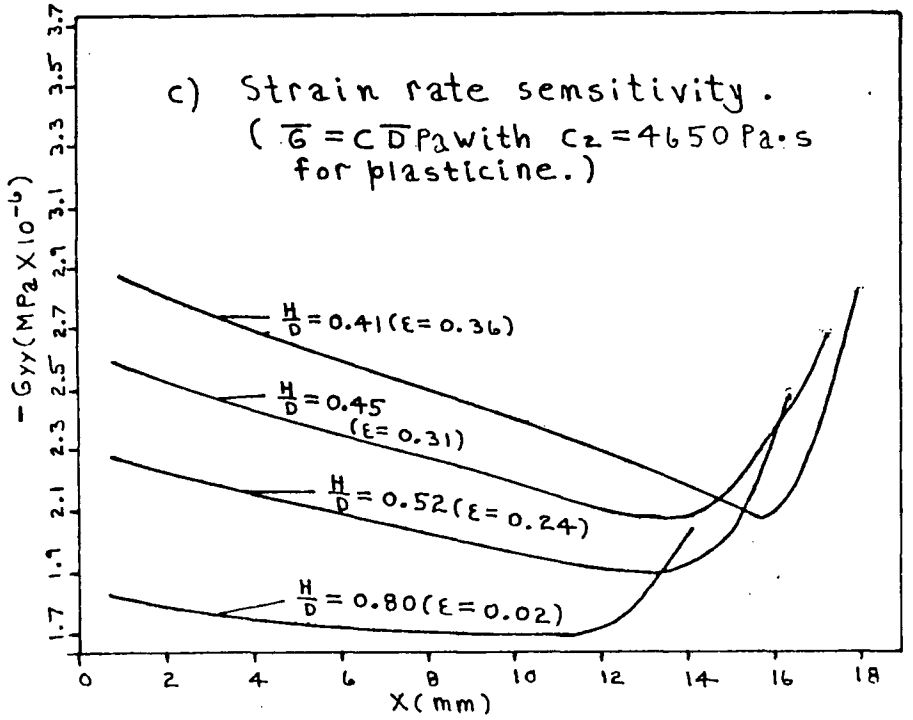

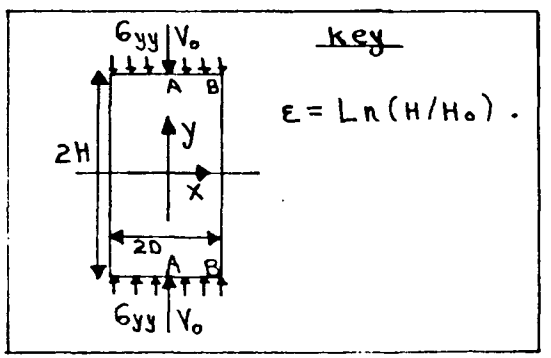

FIG. 5.6.1.3.

NORMAL STRESS (σ_{yy}) AGAINST X ALONG THE TOP AND BOTTOM BOUNDARIES AB FOR SEVERAL H/D RATIOS ACHIEVED BY STRAINING FROM H_o/D_o = 0.84.
a). CONSTANT YIELD STRESS. b). STRAIN HARDENING.
c). STRAIN RATE SENSITIVITY.

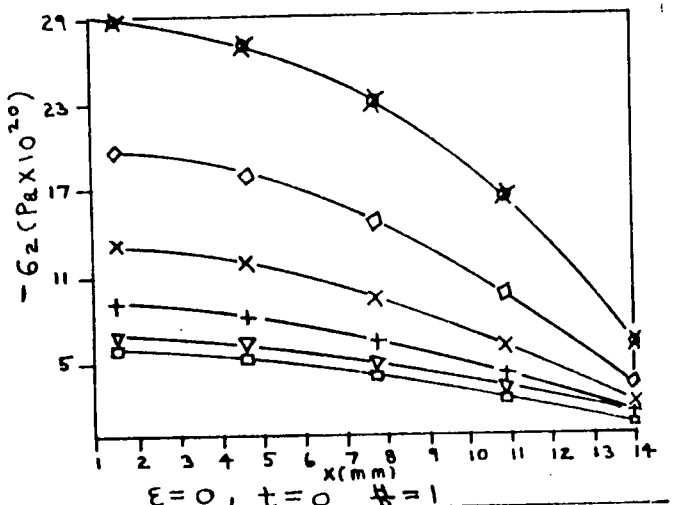

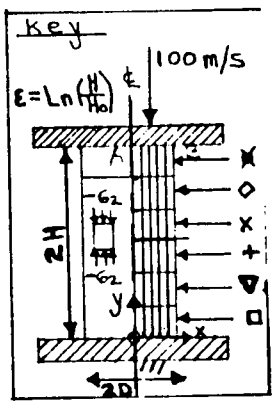

Initial Dimensions:
$2H_0 = 2D_0$ =

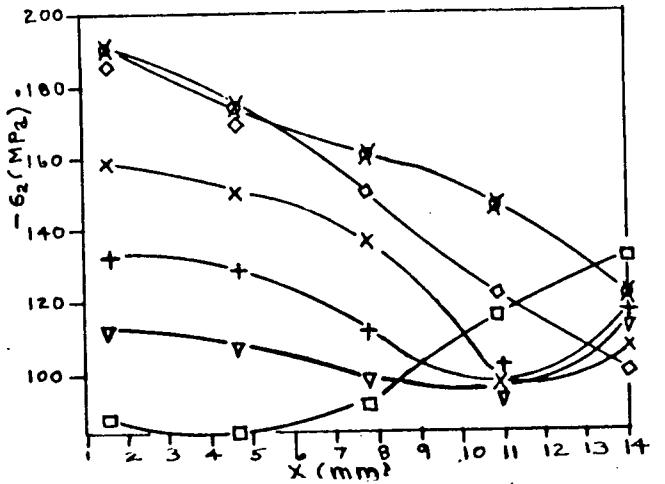

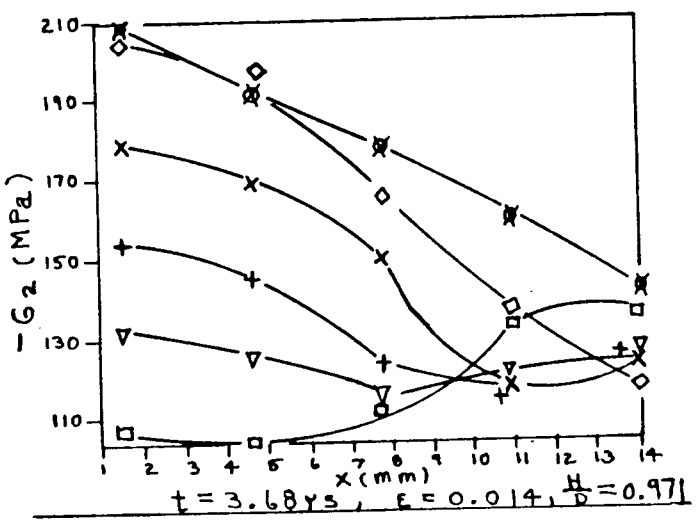

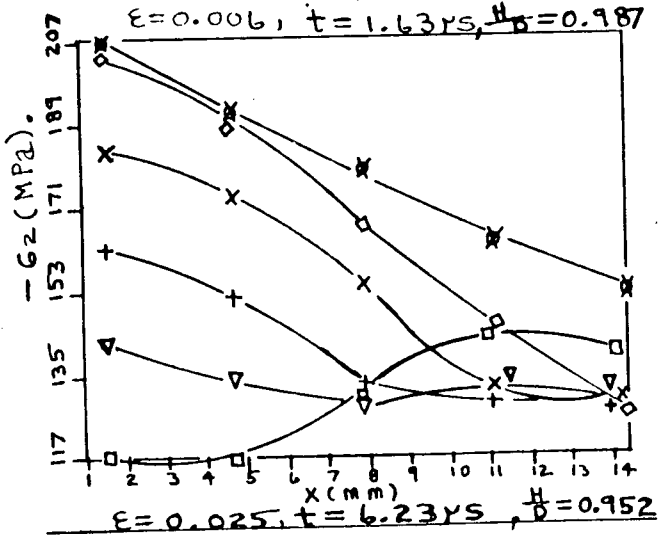

FIG. 5.6.2.1.

$-G_2$ (ELEMENT AVERAGE) AGAINST X FOR THE DYNAMIC COMPRESSION IN PLANE STRAIN OF ALUMINUM AT 100 m/s.

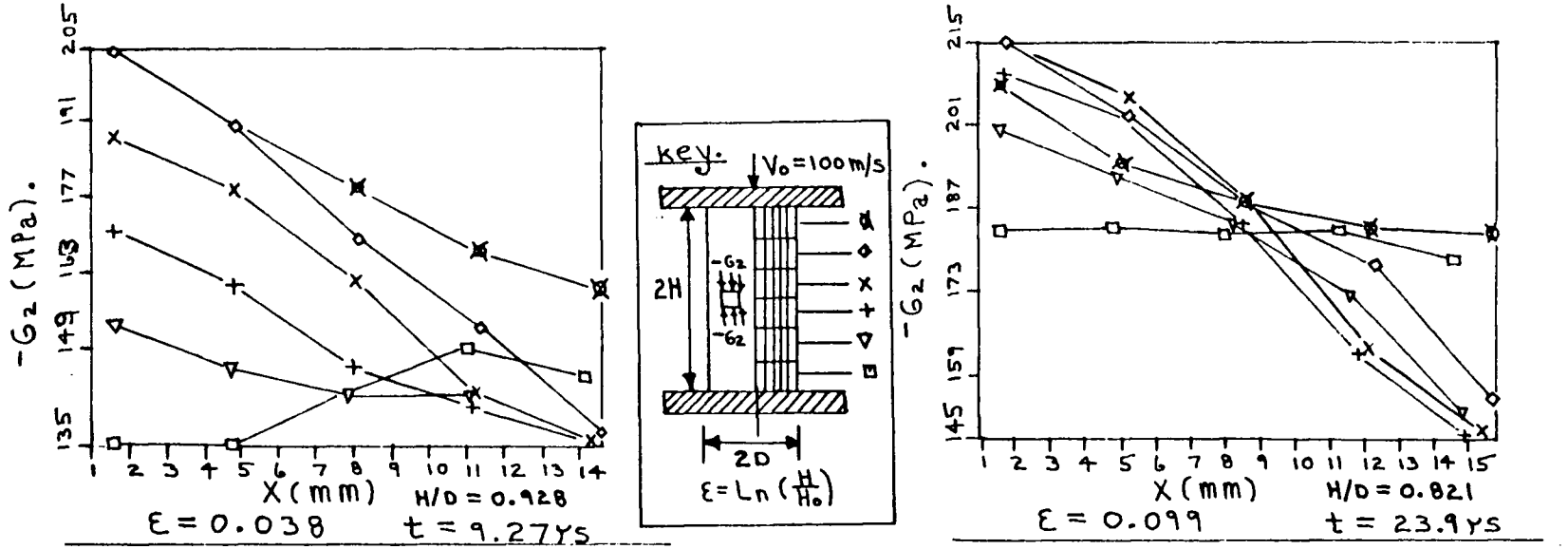

FIG. 5.6.2.2.

GRAPHS OF $-G_2$ AGAINST X FOR DYNAMIC COMPRESSION OF ALUMINUM AT 100 m/s (CONT.). A GRAPH FOR UNLOADING IS ALSO SHOWN.

CHAPTER 6

CONCLUSIONS

The finite element model which was developed for large plastic plane strain deformation proved to be an invaluable tool for investigating the fundamental characteristics of die-forging operations. It dealt successfully with strain hardening, strain rate sensitivity. inertia, interface and end plate friction over a wide range of specimen sizes. It is a flexible and compact code which handles the very large plastic deformation in an efficient way.

The finite element code reproduced exactly the results for frictionless and hence homogeneous deformation in which plane sections remain plane. Comparisons of the billet shape were also made between the finite element model predictions and experimental results for quasi-static compression of aluminum and the dynamic compression of plasticine. There proved to be good comparisons over a large range of deformation, as shown for some select cases in Figs. 6.1, 6.2 and 6.3.

Further studies conducted with the finite element model identified many of the fundamental characteristics of the plane strain forging operations. The conclusions of the effect of specimen height (H) to width (D) ratio, material properties, friction, and inertia are given below.

1. With rigid perfectly-plastic material and H/D>1 deformation tends to concentrate along lines of intense shear. The mode of deformation is approximated by the upper

bound solution given in section 2.3.1. Material tends to stick on the platen (even with low coefficients of friction) and to generate normal interface shear stress distributions clearly different from classical friction hill. Indeed the normal stress distributions were inverse friction hills with the maximum shear stress occurring not at the centre of the specimen, but at the outer edges.

A symmetric buckling or boundary concavity occurred with $H/D>3$. Boundary shape at the onset of deformation significantly affects the mode of deformation.

2. With rigid perfectly-plastic material and $H/D<1$ deformation tends to concentrate along lines of intense shear. The mode of deformation is approximated by the upper bound solution given in section 2.3.3. Material tends to slip on the work platen and generate friction hill type of normal interface stress distributions.

3. With strain hardening material the lines of concentrated deformation become wider and give more homogeneous deformation. With moderate friction the homogeneous solution given in section 2.2 is more appropriate. A friction hill type of normal interface stress distribution is obtained.

There is also a tendency for a concave profile to develop for tall specimens, but the development is somewhat less pronounced than it is for rigid perfectly-plastic material.

4. With strain rate sensitive materials the lines of concentrated deformation become wider and give more homogeneous deformation. The mode of deformation is similar to the strain hardening case except that the effect occurs immediately the material is moving and does not require the material to be significantly strained as it does in the strain hardening case.

5. With dynamic loading the inertia effects are initially dominant and cause local inhomogeneous deformation. However, as the energy of impact is diffused through the specimen, the deformation becomes homogeneous. An inverse friction hill can develop on the stationary platen while at the same time a true friction hill develops on the moving platen.

6. Platen and glass plate friction are both important in determining deformation characteristics. Glass plate friction tends to generate a restraining force so that material tends to rotate around the lower platen. This results in the deformation becoming less homogeneous.

The influence of platen friction depends upon the H/D ratio considered. For $H/D>1$ sticking occurred for quite low values of the coefficient of friction. For $H/D<1$ slipping occured for moderate values of the coefficient of friction.

7. Inverse friction hills can develop at large H/D ratios and low values of strain hardening and strain rate sensitivity.

8. The energy of deformation is used primarily in plastic work within the specimen and in overcoming glass plate friction. Platen friction and surface traction due to atmospheric pressure require very little energy.

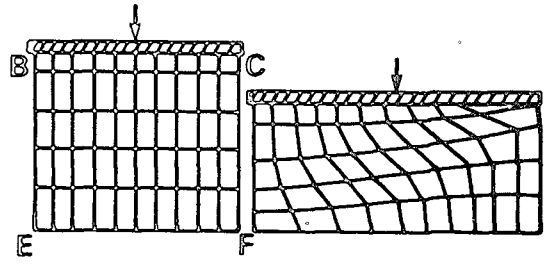

INITIAL MESH DEFORMED MESH

NO STRAIN HARDENING

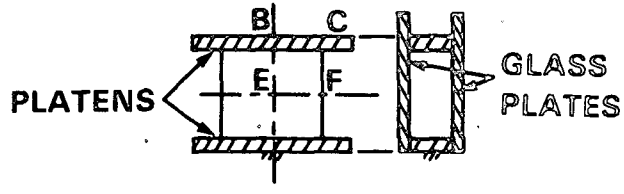

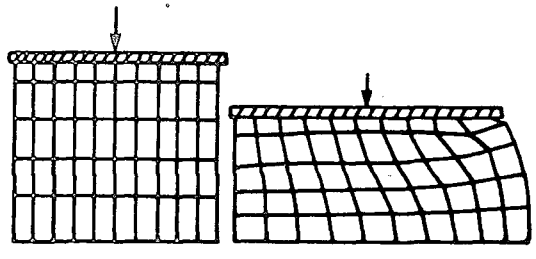

STRAIN HARDENING

FINITE ELEMENT MODEL

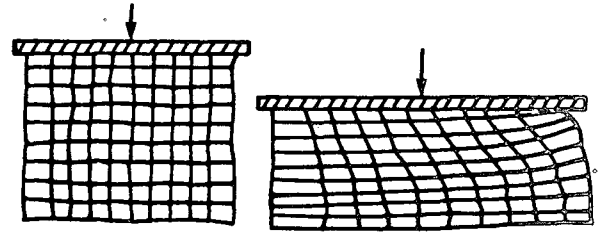

EXPERIMENT

QUASI-STATIC COMPRESSION OF ALUMINUM

FIG. 6.1

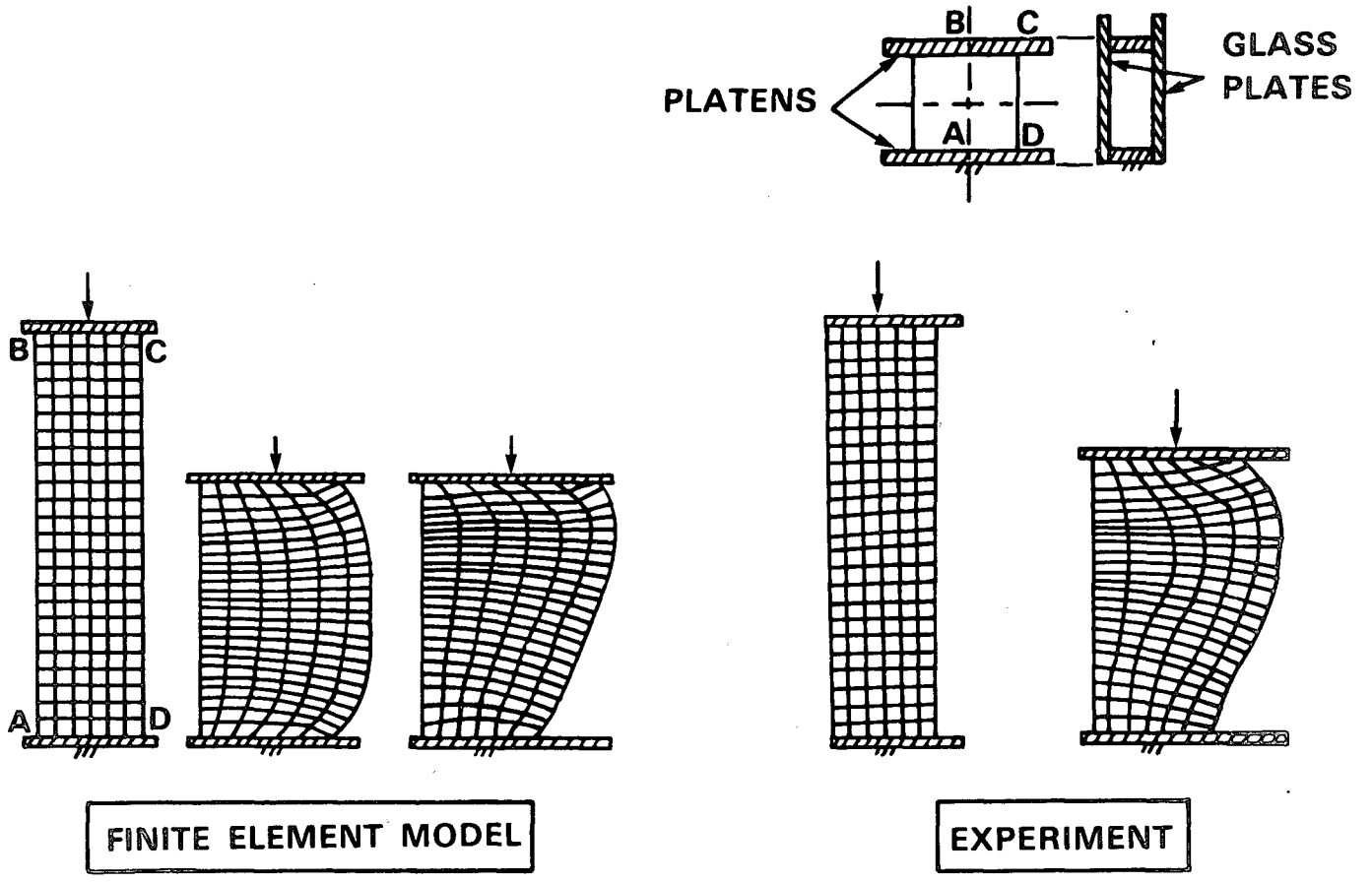

DYNAMIC COMPRESSION OF PLASTICINE

FIG. 6.2

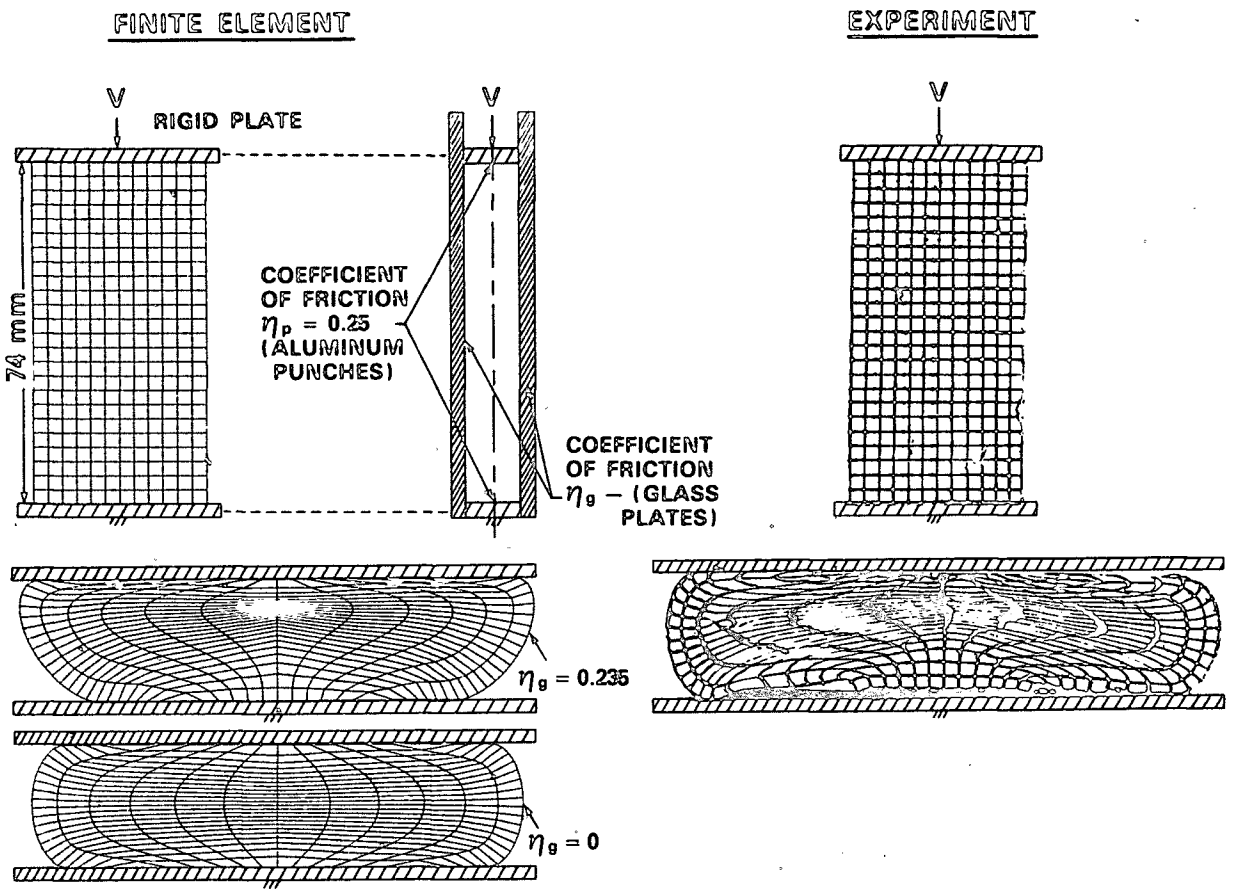

EXPERIMENTAL AND THEORETICAL RESULTS FOR
THE PLANE STRAIN COMPRESSION OF PLASTICINE

FIG. 6.3

REFERENCES

1. B.Avitzur. Metal Forming Processes and Analysis. Mcgraw Hill, 1968.

2. W.Johnson and P.B.Mellor. Engineering Plasticity. Van Nostrand Reinhold Company. 1973.

3. R.Hill The Mathematical Theory of Plasticity. Clarendon Press. Oxford. 1950.

4. H.Hencky. Uber die einige statisch bestimmte Falle des Gleichgewichts in Plastischen Korpern. Z.angew. Math. Mech. 3, 241. 1923.

5. W.Johnson, R.Sowerby, R.D.Venter. Plane-Strain Slip-Line Fields For Metal-Deformation Processes. A Source Book and Bibliography. Pergamon Press, 1982.

6. E.G.Thomsen. Visioplasticity. CIRP Conference. September, 1963.

7. A.H.Shabaik, E.G.Thomsen. Computer Aided Visioplasticity Solution of Some Deformation Problems. Int. Symp. On Foundation of Plasticity. Edited by A.Sawczyk, Noordhoff, Leyden. 1972. PP. 177-199.

8. C.Moore, G.W.Vickers, S.N.Dwivedi. Visioplasticity Solution of Deformation Problems: Data Handling Procedures. International Journal for Numerical Methods in Engineering. Vol. 19, 257-269 (1983).

9. A.H.Shabaik. Finite Difference Method for the Complete Analysis of Plane Strain Extrusion. Proceedings of the Third North American Metalworking Conference. Vol. 3. 1975. PP. 127-142.

10. O.C.Zienkiewicz. The Finite Element Method. 3'rd Edition. Mcgraw-Hill. 1977.

11. H.D.Hibbitt, P.V.Marcal, and J.R.Rice. A Finite Element Formulation for Problems of Large Strain and Large Displacement. Int. J. Solids and Structures. Vol.6. PP. 1069-1086. 1970. Pergamon Press.

12. H.Kitagawa, Y.Seguchi, and Y.Tomita. An Incremental Theory of Large Strain and Large Displacement Problems and its Finite Element Formulation. Ingenieur-Archiv 41. 1972. PP. 213-224. Springer-Verlag.

13. M.Gotoh and F.Ishise. A Finite Element Analysis of Rigid-Plastic Deformation of the Flange in a Deep-Drawing Process Based on a Fourth-Degree Yield Function. Int. J. Mech. Sci. Vol. 20. PP. 423-435. Pergamon Press Ltd., 1978.

REFERENCES

14. O.C.Zienkiewicz, P.C.Jain, and E. Onate. Flow of Solids During Forming and Extrusion: Some Aspects of Numerical Solutions. Int. J. Solids and Structures. Vol. 14. PP. 15-38. 1978. Pergamon Press.

15. O.C.Zienkiewicz and P.N.Godbole. Flow of Plastic and Visco-Plastic Solids with Special Reference to Extrusion and Forming Processes. Int. J. Numerical Methods in Engineering. Vol. 8. PP. 3-16. 1974.

16. O.C.Zienkiewicz and P.N.Godbole. A Penalty Function Approach to Problems of Plastic Flow of Metals with Large Surface Deformations. Journal of Strain Analysis. Vol. 10. No. 3. 1975.

17. C.H.Lee and S.Kobayashi. New Solutions to Rigid-Plastic Deformation Problems Using a Matrix Method. Journal of Engineering for Industry. Aug. 1973. PP. 865.

18. J.W.H.Price and J.M.Alexander. Specimen Geometries Predicted by Computer Model of High Deformation Forging. Int. J. Mech. Sci. Vol 21. PP. 417-430. Pergamon Press Ltd. 1979.

19. P.Hartley. C.E.N.Sturgess, and G.W.Rowe. Friction in Finite-Element Analysis of Metalforming Processes. Int. J. Mech. Sci. Vol 21. PP. 301-311. Pergamon Press Ltd., 1979.

20. J.B.Hawkyard and W.Johnson. An Analysis of the Changes in Geometry of a Short Hollow Cylinder During Axial Compression. Int. J. Mech. Sci. Vol. 9. PP. 163-182. 1967.

21. P.Hartley, C.E.N.Sturgess, and G.W.Rowe. Influence of Friction on the Prediction of Forces, Pressure Distributions and Properties in Upset Forging. Int. J. Mech. Sci. Vol. 22. PP. 743-753. Pergamon Press Ltd., 1980.

22. G.T.Van Rooyen and W.A.Backofen. A Study of Interface Fricton in Plastic Compression. Int. J. Mech. Sci. 1960. Vol. 1. PP. 1-27.

23. W.Johnson. Impact Strength of Materials. Edward Arnold. 1972.

24. I.M.Hutchings and T.J.O'Brien. Normal Impact of Metal Projectiles Against a Rigid Target at Low Velocities. Int. J. Mech. Sci. Vol. 23. PP. 255-261, 1981.

25. G.R.Johnson. Analysis of Elastic-Plastic Impact Involving Severe Distortions. Trans. ASME. Vol. 43. Journal of Applied Mechanics. Sept. 1976.

REFERENCES

26. G.R.Johnson. High Velocity Impact Calculations in Three Dimensions. Trans ASME. Vol. 44. March 1977. Journal of Applied Mechanics.

27. J.A.Zukas. Impact Dynamics. Theory and Experiment. Emerging Technologies in Aerospace Structures, Structural Dynamics, and Materials. ASME. 1980.

28. J.F.W.Bishop, On The Effect Of Friction On Compression And Indentation Between Flat Dies. Journal of the Mechanics and Physics of Solids, 1958, Vol. 6 pp. 132-144. Pergamon Press Ltd., London.

29. Y.Tomita and R.Sowerby. The Deformation Mechanics Of Rate Sensitive Materials. Int. J. Mech. Sci. Vol. 20. pp. 361-371. 1978.

30. G.E.Mase, Continuum Mechanics. Schaum's Outline Series. Mcgraw-Hill Book Company. 1970.

31. S.Y.Aku. R.A.C.Slater, and W.Johnson. The Use of Plasticine to Simulate the Dynamic Compression of Prismatic Blocks of Hot Metal. Int. J. Mech. Sci. Pergamon Press Ltd. 1967. Vol. 9. PP. 495-525.

32. G.W.Vickers, A.Plumtree, R.Sowerby, and J.L.Duncan. Simulation of the Heading Process. Trans. ASME. Journal of Engineering Materials and Technology. 1974.

33. T. Alton, S.Oh and H. Gegel, Metal Forming, American Soc. of Metals, 1983.

34. Open Die Forging Manual, Forging Ind. Assoc., 1982.

REFERENCES